THE UNIVERSITY OF ASTON IN BIRMINGHAM.

RADIAL-FIELD MAGNETIC ELECTRON LENSES.

Thesis submitted for the degree of
DOCTOR OF PHILOSOPHY
by
C. D. Newman.

DEPARTMENT OF PHYSICS
SEPTEMBER 1976.

SUMMARY

This investigation looks critically at conventional magnetic lenses in the light of present-day technology with the aim of advancing electron microscopy in its broadest sense. By optimising the cooling arrangements and heat transfer characteristics of lens windings it was possible to increase substantially the current density in the winding, and achieve a large reduction in the size of conventional magnetic electron lenses.

Following investigations into the properties of solenoidal lenses, a new type of lens with only one pole-piece was developed. The focal properties of such lenses, which differ considerably from those of conventional lenses, have been derived from a combination of mathematical models and experimentally measured axial flux density distributions. These properties can be profitably discussed with reference to "half-lenses".

Miniature conventional twin pole-piece lenses and the proposed radial field single pole-piece lenses have been designed and constructed and both types of lenses have been evaluated by constructing miniature electron optical columns. A miniature experimental transmission electron microscope (TEM), a miniature scanning electron microscope (SEM) and a scanning transmission microscope (STEM) have been built.

A single pole-piece miniature one million volt projector lens of only 10cm diameter and weighing 2.1kg was

designed, built and tested at 1 million volts in a commercial electron microscope.

Preliminary experiments indicate that in single pole lenses it is possible to extract secondary electrons from the specimen in spite of the presence of the magnetic field of the probe-forming lens. This may well be relevant for the SEM in which it is desirable to examine a large specimen at a moderately good resolution.

ACKNOWLEDGEMENTS

The research described in this thesis was supported by a grant from the IMS Division of the National Physical Laboratory, Teddington, and I would like to thank Drs. A. Franks and P. Stuart of the above division and my supervisor Professor T. Mulvey for many helpful discussions during the course of the work. I would also like to thank Mr. J. Lloyd, Senior Technician on the project, for constructing the new lenses and most of the experimental electron-optical columns described in this thesis. I should also like to thank the Director of the C.E.G.B. Research Laboratories at Berkeley, Gloucestershire, for placing the million volt HU 1000 electron microscope at our disposal for testing the miniature projector lens, and Mr. G. K. Rickards of the above laboratory for his advice and help in mounting the experiment.

I am indebted to Dr. E. Munro of the University of Cambridge Engineering Department and Mr. W. Trowbridge of the Rutherford Laboratory, Harwell, for their kind assistance with the specialized computation of the field distribution of the snorkel lens.

I am grateful to Dr. S. Juma for the use of his rotation-free magnetic lenses in the miniature transmission and scanning transmission electron microscopes, and to Mr. Akhtar for some experimental assistance in the scanning electron-optical system. Finally I wish to thank Mr. R. Keen and Mr. K. Bate for general assistance in the construction of the miniature systems, and Mr. R. Howes and Mr. E. A. Newman for the photographs used in this thesis.

LIST OF SYMBOLS

(SI units used throughout unless otherwise stated)

A	winding area
a	cross-sectional area of conductor
B	flux density
b	half the 'half width' of the flux densiy distribution
C	constant of integration
C_s	spherical aberration coefficient
c	specific heat
D	diameter
d	density
e	electronic charge ($1.6021917 \times 10^{-19}$C)
f	focal length
H	hydraulic diameter
h	heat transfer coefficient
I	current
K	paraxial ray parameter ($K^2 = eB^2/8mV$)
k	thermal conductivity
L	length of conductor forming a coil
l	length
m	electronic mass (9.109558×10^{-31}kg)
N	number of turns
Nu	Nusselt number (hH/k)
Pr	Prandlt number (cu/k)
Q	heat generation rate
q	heat flux
R	resistance
Re	Reynolds number (Hvd/u)

r	radius
S	surface area of coil
T	temperature
U	volume
u	viscosity
V	voltage
v	velocity
W	power
2w	width of coil
x,y,z	cartesian coordinates

Greek symbols

α	temperature coefficient of resistivity
η	exponent parameter
θ	temperature difference
λ	packing factor
ρ	resistivity
σ	current density
ω	constant ($\omega = (1 + eb^2B_M^2)/8mV$)

Subscripts

A	average
C	cold
c	centre
cu	copper
f	fluid
H	hot
i	insulation
in	initial

M	maximum
m	mean
n	normal
o	objective
opt	optimum
p	projector
R	relativistic
s	surface
z	axial
1	inner
2	outer

LIST OF FIGURES

CONTENTS

1. INTRODUCTION

1.1 The Conventional Magnetic Electron Lens

A magnetic electron lens must produce an axially symmetrical magnetic field. It is designed and constructed mainly with this feature in mind. A magnetic lens consists of a current carrying coil shrouded in an iron circuit except for a small gap where the effect of the field is localised. The iron circuit, shaded in Figure 1.1, has a central column with shaped polepieces, an outer cylindrical casing and a top plate, forming a closed circuit except for an air gap between the polepieces. A single coil shown in the figure could in practice be a set of coils all carrying a stabilised current of a few amperes. The focussing field is produced by accurately machining a hole down the axis of symmetry of the magnetic circuit.

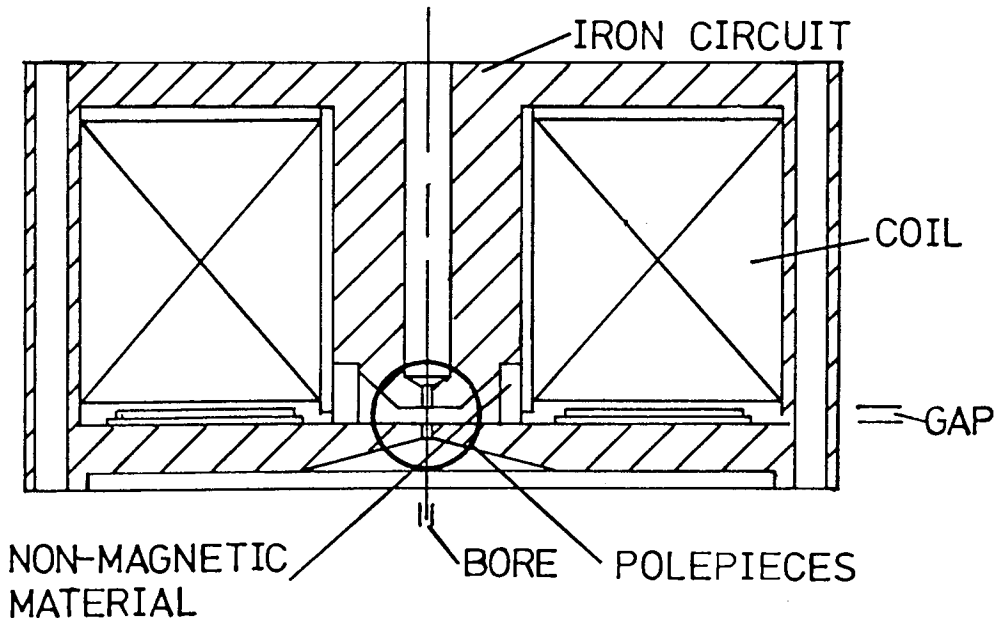

Figure 1.1 Conventional magnetic electron lens

In the region of the gap the original uniform magnetic field is now distorted (see Figure 1.2), giving rise to the lens action. Inaccuracy of the machining or assembly operations can introduce errors or aberrations in the final lens, in addition to those arising from the shape of the magnetic field distribution.

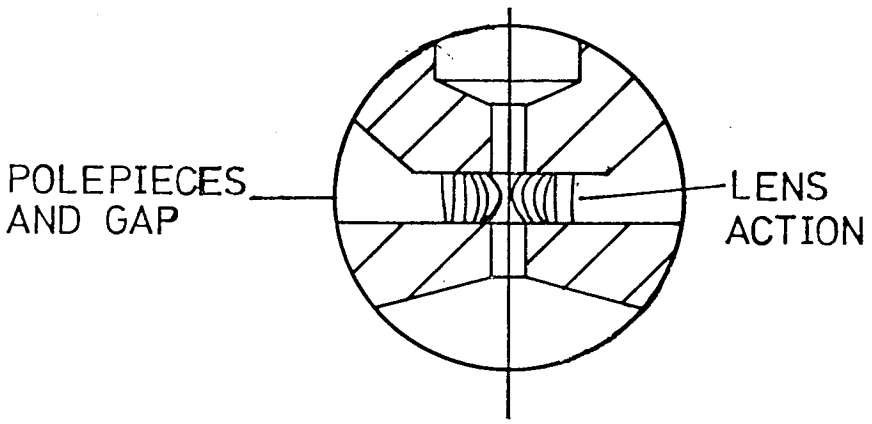

Figure 1.2 Polepieces of the conventional magnetic lens and the magnetic flux lines producing the lens

A magnetic electron lens has two main applications, namely to form an electron probe, i.e. a demagnified image of an electron source, or alternatively to form a highly magnified image of a small object. An electron microscope is constructed by stacking a series of magnifying magnetic lenses in a column, see Figure 1.3. An electron source at one end illuminates a specimen and a fluorescent screen at the other reveals a highly magnified image. The objective lens, which controls the

resolution of the microscope, forms an enlarged intermediate image which is then projected onto the fluorescent screen or photographic plate by the projector lenses, which determine the magnification and distortion of the image. Magnifications of up to several million can be usefully produced in this way.

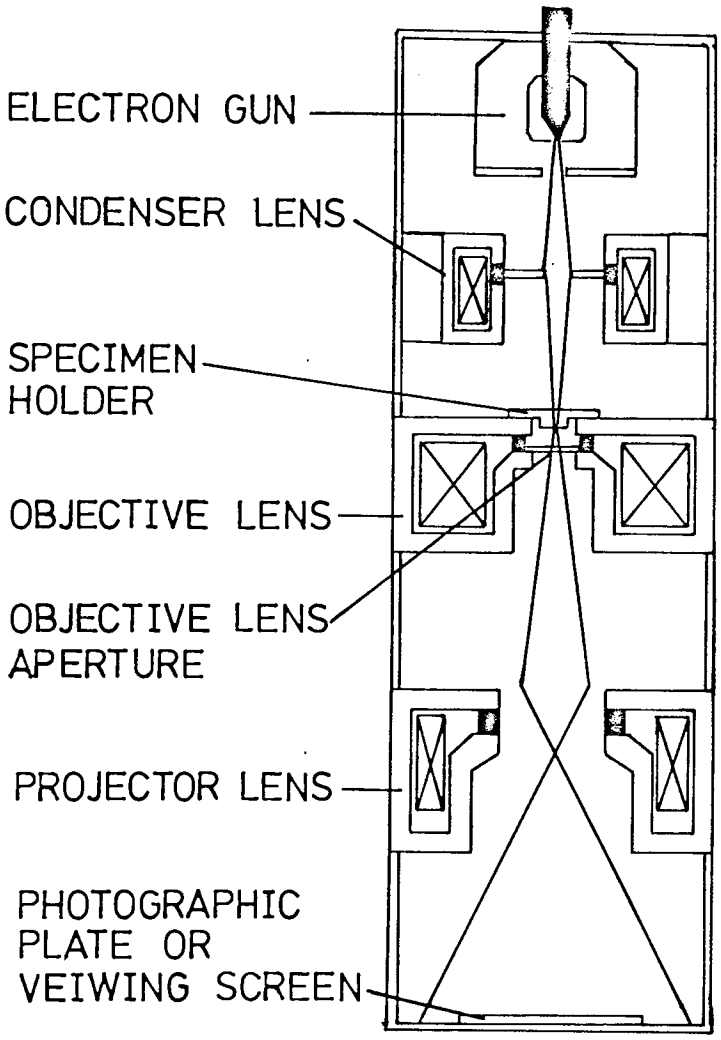

Figure 1.3 Arrangement of magnetic electron lenses in an electron microscope. The illuminating source is an electron gun which emits a high energy beam of electrons. The condenser lens controls the degree of illumination over the specimen. The objective lens focuses the electrons scattered by the specimen into an intermediate image. This image is further magnified by the projector lens,which produces the final image on the viewing screen.

1.2 Innovations in Electron-Optical Instruments

The conventional electron microscope has followed closely the original ideas of Knoll & Ruska (1932). In the scanning electron miscroscope, (SEM) developed by Knoll in 1935, a highly demagnified image of an electron source is produced by a similar group of lenses. This electron "probe" is then allowed to fall on to the specimen. The probe is then scanned in a raster across the specimen and any physical effect, such as the emission of secondary-electrons from the specimen, caused by the impinging probe, can be detected and displayed on a cathode ray oscilloscope running in synchronism with the probe raster. This instrument has been highly developed using secondary-electrons as the contrast-producing mechanism. (Smith and Oatley 1955).

The transmission electron microscope (TEM) with a resolution of 2.4Å (Thon 1969) and the scanning microscope (SEM) with a resolution 100Å (Pease & Nixon 1965) or better are two types of instruments with very different capabilities. The conventional TEM system is very useful if examining thin specimens at high magnification while the scanning electron microscope is useful for the examination of the surface of thick specimens at a lower magnification. The SEM can be operated in the transmission mode (STEM) and although these two instruments appear to be very different at first sight, with their separate techniques and methods of image formation, it has been shown that these two microscope

systems can be considered to be identical, (Crewe 1970). The advantage of the scanning image is that although it contains exactly the same information as that of the transmission image, the information is provided in a more convenient form for image processing.

Many modern 100kV transmission electron microscopes are being developed and sold commercially as multi-purpose instruments for X-ray microanalysis, scanning electron miscroscopy and scanning transmission electron microscopes (STEM). The scanning transmission mode and the X-ray analysis mode are valuable adjuncts to the simple transmission mode. Many commercial transmission microscopes can be operated in the X-ray microanalysis, scanning and scanning transmission modes by adjusting the position of the specimen in the objective and appropriately switching the lens power supplies. (Maclachlan 1973).

1.3 Miniaturisation of Conventional Lenses

Since the first electron microscope was produced the quality and versatility of the instrument has improved greatly. This progress has stemmed from the improvements in the stabilisation of the electronic power supplies and the increase in accuracy of the many machining operations necessary to produce an electron microscope. Further improvement in these respects is likely to be of minor significance compared with the problems, such as radiation damage, to be solved in image formation at high resolutions with practical specimens.

In order to achieve high resolution, a large effort has been spent on achieving a high flux density in as small a gap as possible in the polepieces. This technique leads to designs in which specimen manipulation is difficult and vacuum conditions tend to be very poor. It is also very difficult to extract information from the specimen in the form of X-ray photons and secondary-electron emission. Because of the use of thermionic valve power supplies in the past the power that could be supplied to the lenses was limited and hence very bulky windings surrounded by large magnetic circuits have become an accepted feature of magnetic lenses. The stray fields produced by these large lens housings lead to alignment problems and other difficulties. Some of these problems can be solved by using superconducting windings (Farrant 1970) but these introduce experimental difficulties and at present do not appear economically viable for routine use. Another possibility would be to use iron-free "mini-lenses" in the form of a long solenoid (Le Poole 1964). This technique has been used (Fontijn, Bok & Kornet 1968), (Cooke & Openshaw 1970) and (Cooke & Duncumb 1968) successfully for comparatively weak probe forming lenses but not for objectives.

As it is relatively easy to cool the windings of a long thin solenoid, Le Poole was able to work at current densities of 6000 Amps/cm^2 which compares favourably with

200 Amps/cm² of conventional windings. Unfortunately, solenoidal lens have spherical aberration coefficients of the order of their length and their small diameter creates constructional problems which can limit their performance at high resolution. A relaxation of the mechanical tolerances (Bassett & Mulvey 1968) can be achieved by a conical solenoid. Nevertheless, the constructional difficulties of winding such lenses are still difficult to overcome. A more promising approach is the use of flat helical lenses or pancake lenses (Bassett & Mulvey 1969) in conjunction with an iron screen. Such lenses form a bridge between conventional and superconducting lenses.

1.4 Mini-Lenses in Electron Microscopy

The basic constructional techniques for miniature lenses (Mulvey & Newman 1972) are described in Appendix 1. Such lenses have proved reliable and easy to fabricate, once the basic design parameters are appreciated. These allow a wide selection of lenses to be produced. These lenses are applicable in every branch of microscopy, scanning transmission electron microscopy STEM (Mulvey & Newman 1973, Appendix 2) high voltage electron microscopy HVEM (Mulvey & Newman 1973b, Appendix 3).

This thesis describes, among other things, the early experiments leading to the evolution of the iron-shrouded minilens. Chapter two is devoted to a theoretical appraisal of how such a lens is to be designed and

constructed. This includes the matching of the lens winding to its power source, and the thermal consequences of confining a large heat source in a small volume; perhaps surprisingly, this can be achieved without an undue temperature rise. A comparison between copper tape and enamelled copper wire coils was carried out and is described in Chapter 3 together with a description of the construction of a few simple windings and their subsequent performance.

A theoretical discussion on the lens properties of miniature lenses is given in Chapter 4. Various theoretical lens models have been considered to explain and help the design of the new miniature lenses. These models are briefly mentioned together with the simple computer programmes devised during the course of this investigation in order to achieve an adequate theoretical understanding of the focal properties of these lenses.

The practical construction of the lenses and the experimental results obtained on the Intercol Electron Optical Bench is fully described in Chapter 6, where comparisons of size and performance of miniature and conventional lenses are made.

A series of experiments involving a current-carrying coil and cylinder of soft iron are described in Chapter 7. These led to the introduction of the "radial-field" or "single-pole" lens. These lenses are suitable as objective lenses in a complete electron

optical system. Chapter 7 explores the early attempts to devise a practical form of the lens and the development of a nearly optimised form of a single pole lens. The focal properties of single pole lenses were evaluated using the techniques described in Chapters 4 and 5.

The subsequent chapters of the thesis are concerned with systems of miniature electron optical elements from a simple transmission electron microscope stack to the scanning electron microscope, and finally, the thesis ends with a description of a miniature high voltage lens.

2. DESIGN OF THE LENS WINDING

2.1 Relationship between input power, coil dimensions and excitation

A conventional lens winding consists of many thousands of turns working at a fraction of an amp, derived from a stabilized power supply making use of thermionic valves of limited output. With the advent of solid-state power supplies, stabilised currents of 10 -100 amps are now readily obtainable giving an order of magnitude more power. It thus becomes feasible to operate a compact coil of a few hundred turns at a large current provided the heat produced in the windings can be removed. For a reduction of volume of about two hundred times the power required is about six times that of a conventional winding. However, the reduction in lens size and decrease in aberration may more than compensate for the increase in power. Alternatively, by the use of a larger number of such compact coils, efficiently cooled, the power may be kept the same as in a conventional coil and a more modest reduction of lens size accepted.

It is easily shown, that for any exciting coil used in a magnetic electron lens the power input W is related to the ampere-turns NI in the lens and the current density σ in the wire by

$$W = \rho\sigma\pi D_m \cdot (NI) \qquad \ldots\ldots 2.1.1$$

where D_m is the mean diameter of the coil and ρ is the resistivity of the wire forming the coil.

In designing windings for electron lenses a specific number of ampere-turns have to be obtained for the lens to work over the required range of electron beam voltages. Thus, for a projector lens it is desirable to have sufficient excitation for the lens to work at its minimum focal length for the largest accelerating voltage which is to be applied.

In general, miniature lens windings consume a larger amount of power than those of conventional lenses (Mulvey and Newman, 1972, Appendix 1), but providing the cooling requirements of the winding are met the maximum power W_M available from the power supplies may be a limiting factor. For a given number of ampere-turns, and a maximum power W_M the current density in the wire is given by:

$$\sigma = W_M/(\rho\pi D_m.(NI)) \qquad \ldots\ldots\ldots \text{2.1.2}$$

from equation 2.1.1

The mean diameter D_m, a geometrical term dependent on the size of the winding, may be limited if the lens has to fit in a specific space of an existing instrument, (Mulvey and Newman 1973b, Appendix 3).

The resistivity ρ is temperature dependent, for example (for copper) $\rho = 1.72.10^{-8}$ ohm-m at $20^{o}C$ and $2.54.10^{-8}$ ohm-m at $120^{o}C$. From equation 2.1.2 it can be seen that if either the coil size or the operating temperature is increased, the current density at which the conductor in the winding is running is reduced. These terms are interdependent.

The current density in a coil, Figure 2.1 is given by:

$$\sigma = NI/w\lambda(D_2-D_1) \quad \ldots\ldots\ldots \quad 2.1.3$$

Substituting 2.1.3 in 2.1.1 gives

$$W = (\rho\pi/2w\lambda).(NI)^2.(D_2/D_1+1)/(D_2/D_1-1) \ldots 2.1.4$$

which is valid for wire and tape windings. This equation is useful in determining how much power is necessary for a required excitation. The power W is plotted in Figure 2.2 which shows the calculated values of W against D_2/D_1 for copper-wound coils with a packing factor λ of 75% required to produce 4000 A-t, and coils with λ = 65% producing 2000 A-t. The limits are drawn for temperatures of 120°C and 20°C; in practice the temperature will usually lie between these limits. Thus the power required to produce a given number of ampere-turns for a coil decreases as D_2/D_1 increases. The mean temperature of these coils will also fall as D_2/D_1 is made larger, since the increase in surface area enhances the transfer of heat from the coil.

When designing a lens winding the ratio D_2/D_1 should be kept as large as possible, consistent with other requirements.

2.2 Optimisation of the wire diameter

In order to make the best use of a given power supply it is important to choose the correct wire diameter for the lens. Consider a power supply capable of delivering a maximum current of I_M amps at a maximum

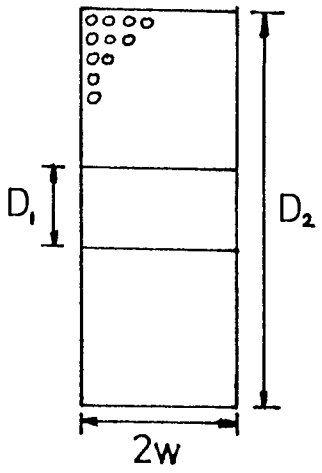

$$\sigma = NI/w\lambda(D_2-D_1)$$

$$D_m=(D_2+D_1)/2$$

Figure 2.1 Parameters of a winding used to define the current density σ and mean diameter D_m, where D_1 is the inner diameter, D_2 the outer diameter, 2w the winding width, N the number of turns, I the current in the winding and λ the packing factor.

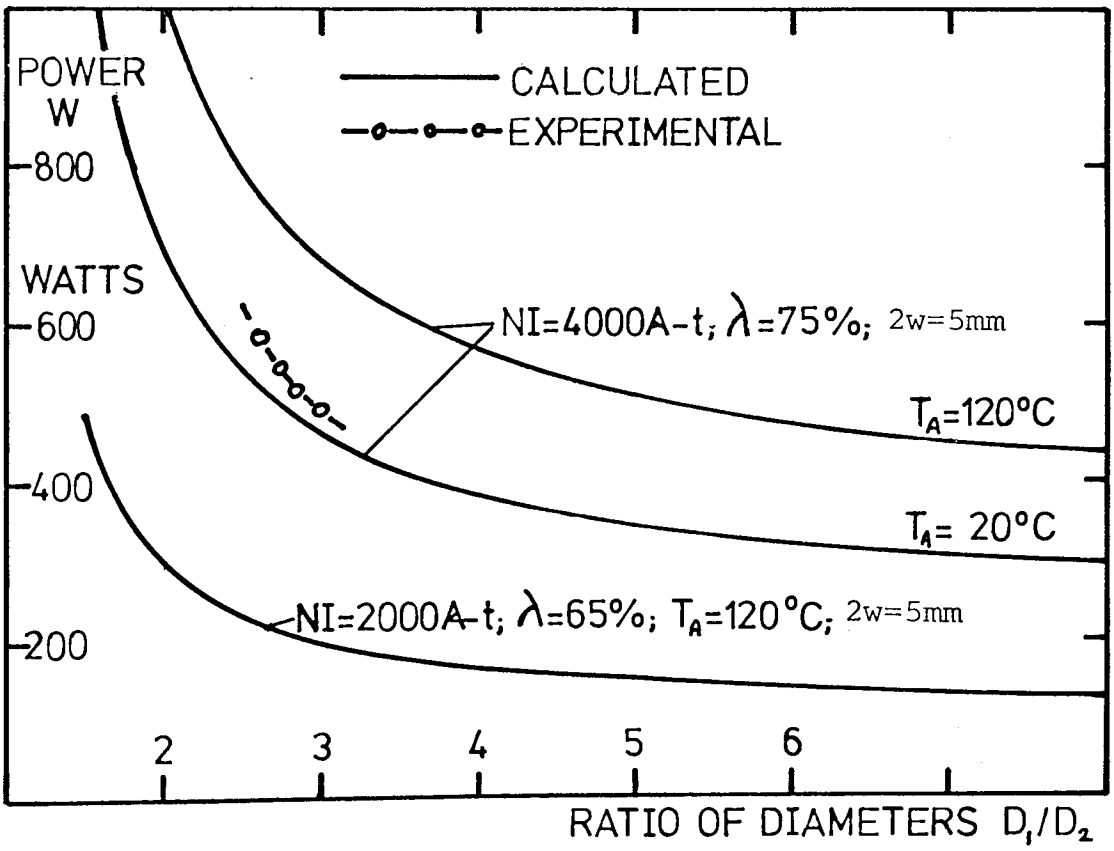

Figure 2.2 Variation of power W with coil diameter ratio (D_2/D_1) for constant excitation NI and average coil temperature T_A. λ is the packing factor.

voltage of V_M volts. The maximum power is then $V_M I_M$ watts. This maximum power can only be delivered into a load of V_M/I_M ohms, namely the resistance of the winding working at its operating temperature.

In this instance the coil resistance R_H will be matched to the power supply and will draw the maximum amount of power W_M available.

$$W_M = V_M I_M \quad \ldots\ldots 2.2.1$$

$$R_H = V_M/I_M \quad \ldots\ldots 2.2.2$$

Table 2.1.1 shows this experimentally for a coil of 275 turns connected to a power supply, (V_M = 40 volts, I_M = 25 amps). The current and voltage readings were noted as the turns were removed from the coil. Notice that maximum ampere-turns occur when the working resistance of the coil is the same as the resistance V_M/I_M of the power supply.

Table 2.1.1 Optimisation of lens winding to a power supply

N (turns)	NI (Ampere turns)	I (Amps)	VI (watts)	I (Amps. m^{-2}
275	4580	16.7	685	$6.680.10^7$
261	4650	17.8	725	$7.120.10^7$
236	4760	20.2	808	$8.080.10^7$
220	4880	22.2	898	$8.890.10^7$
200	5000	25	1000	1.10^8
180	4500	25	900	1.10^8

Consider a coil made from a length L (m) of conductor of cross-sectional area a(m^2). Its resistance will be:

$$R_H = \rho L/a = R_C(1+\alpha\theta) \quad \ldots\ldots \quad 2.2.3$$

at the operating point. The current density will be

$$\sigma_M = I_M/a \quad \ldots\ldots \quad 2.2.4$$

at the same point. An optimum value a_{opt} for the cross-sectional area of the conductor can be obtained from equations 2.1.2 and 2.2.4

$$a_{opt} = I_M \rho\pi D_m(NI)/W_M \quad \ldots\ldots \quad 2.2.5$$

If a value for ρ is assumed and if the term D_m has been fixed there will be an optimum wire size for the coil winding.

Equation 2.2.5 can be rearranged as:

$$a_{opt} = \pi\rho D_m N_{opt} I_M^2/W_M \quad \ldots\ldots \quad 2.2.6$$

where N_{opt} is the optimum number of turns in the winding. For any coil

$$N = \frac{\text{Winding area(A) x Packing factor}(\lambda)}{\text{Cross-sectional area of conductor(a)}} \ldots 2.2.7$$

hence $$N_{opt} = A\lambda/a_{opt} \quad \ldots\ldots \quad 2.2.8$$

Substituting 2.2.8 in 2.2.6 yields an expression for the optimum wire size a_{opt}:

$$a_{opt} = (\pi\rho D_m A\lambda I_M^2/W_M)^{\frac{1}{2}} \quad \ldots\ldots \quad 2.2.9$$

Substituting 2.2.8 in 2.2.5 yields an expression for the optimum number of ampere-turns $(NI)_{opt}$:

$$(NI)_{opt} = (W_M A\lambda/\rho\pi D_m)^{\frac{1}{2}} \quad \ldots\ldots \quad 2.2.10$$

Two cases can now be considered.

Wire sizes less than the optimum ($a<a_{opt}$)

Here the power supply will limit at its maximum output voltage V_M and NI is given by:

$$NI = V_M a/\rho\pi D_m \quad \ldots\ldots \quad 2.2.11$$

Thus the excitation NI is proportional to wire diameter a, if a is less than the optimum diameter a_{opt}.

Wire sizes greater than the optimum ($a>a_{opt}$)

In this case the power supply will limit at its maximum output current I_M.

$$NI = \lambda A.I_M/a \quad \ldots\ldots \quad 2.2.12$$

Thus the excitation (NI) is inversely proportional to a if a is greater than the optimum diameter a_{opt}. This is shown in Figure 2.3.

In both these cases ρ has been assumed to be a constant. In fact the value of ρ depends on the temperature of the coil. To a first approximation ρ can be assumed to take a value corresponding to the mean operating temperature of the coil. The operating temperature of the coil will depend on the number of layers of conductors in the coil, the insulation thickness between conductors and the power dissipated in the winding.

When designing a coil a realistic value of ρ must be chosen. If there is a choice between two wire diameters the larger should be chosen if an optimistic value of ρ has been assumed and the smaller if a pessimistic value of ρ has been chosen. Figure 2.3 shows

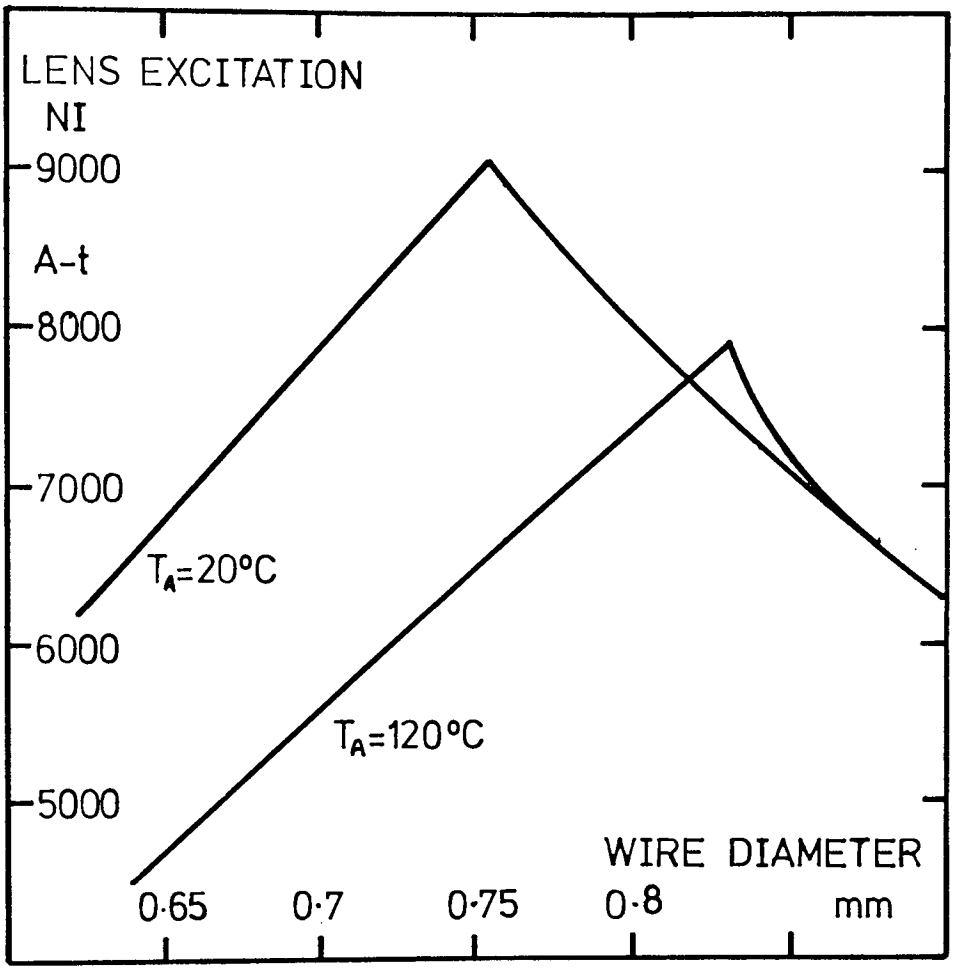

Figure 2.3 Maximum lens excitation as a function of wire diameter for a power supply with characteristics V_M = 60 volts, I_M = 25 Amps supplying a coil with parameters D_m = 51.5 mm, 2w = 4.7 mm, A = 470 mm^2 and λ = 0.65 with the average temperature of the winding kept constant.

the maximum ampere-turns obtainable from a fixed power supply plotted against wire diameter. NI is proportional to the wire diameter (a) for a $<a_{opt}$ assuming ρ remains constant and inversely proportional to (a) for $a>a_{opt}$. Two curves are shown in Figure 2.3 assuming a constant temperature of $20^{o}C$ and $120^{o}C$ respectively. From a consideration of the thermal properties of a particular coil, an estimate of the operating temperature can be obtained. With this information one can decide whether the coil is to be wound with $a<a_{opt}$ or $a>a_{opt}$ and of course the estimated ampere-turns that will be produced.

2.3 Heat Conduction and Thermal Conductivity

The current needed to excite a lens produces ohmic heating in the lens windings. This heat must be removed or serious damage to the coil may result. When dissipating low powers it is sufficient to let natural conduction to the coil yoke and cheeks provide the cooling process, and in some cases blowing air onto the windings will suffice. With a miniature lens the use of high current-densities necessitates the use of high powers typically 300-500 watts per lens. Dissipating this power in a small uncooled volume would result in immediate damage. The simplest design (Mulvey and Newman 1972, Appendix 1) for a miniature lens has the actual coil winding immersed in the coolant (water) flow which allows the large amounts of heat generated to be removed. The maximum amount of heat that can be removed is

determined by the maximum temperature allowable in the coil. This temperature is determined by the properties of the insulating material. The maximum temperature is also determined by the shape of the coil, the thermal conductivity of the materials making up the coil and the efficiency of the heat transfer process to the cooling water.

If, in a steady state, heat is generated at a rate of $Q(\text{Watts.m}^{-3})$ in a substance of conductivity $k(\text{Watt m}^{-1}{}^{o}\text{C}^{-1})$ then from the diffusion equation the temperature distribution will be given by:

$$\frac{d^2T}{dx^2} + \frac{d^2T}{dy^2} + \frac{d^2T}{dz^2} = Q/k \quad \ldots\ldots \quad 2.3.1$$

Solution of this equation will give the complete temperature distribution throughout the coil; in practice only two temperatures are of interest, the average temperature T_A of the coil and its maximum temperature T_C. These are determined theoretically in Section 2.5.

The temperature T_A determines the resistance of the coil, the importance of which has been described in the preceding sections. The temperature T_C determines the maximum amount of power that can be dissipated in the windings without damaging the insulation. Both these temperatures can be determined approximately without resorting to the solution of equation 2.3.1 which is sometimes difficult and always tedious.

The thermal conductivity of a substance is defined as:

$$k = (W/S).(dT/dx) \quad \ldots\ldots \quad 2.3.2$$

where W is the power flowing in the x direction through the surface S and $\frac{dT}{dx}$ is the temperature gradient in the x direction.

The thermal conductivity for copper is approximately 400 Watts.m^{-1}.$^{o}C^{-1}$ and for a typical insulating material is approximately 2.10^{-1} Watts.$m^{-1}{}^{o}C^{-1}$. This demonstrates the fact that a coil wound with insulated copper wire will have a thermal conductivity determined largely by the insulating material. The thermal conductivity of the lens winding will in fact depend on the packing factor λ and the thermal conductivity of the insulating material.

The packing factor λ depends on the method of winding, the wire diameter and the thickness of the insulation. The insulation thickness of wires is proportioned to the square root of the wire diameter so λ will increase with wire diameter. With wide coils it is possible to wind successive layers in the interstices of the previous layer resulting in an increase in λ. In the present investigation, the coils were thin, 2-4 wires occupying the half-width of the coil, giving a value of $\lambda \simeq$ 60-70%.

A coil wound with insulated copper wire will have a thermal conductivity determined largely by the insulation

alone. The shape of the wire, the packing factor (λ) and the thermal conductivity of the insulation (k_i) all determine the gross thermal conductivity of the coil.

A relationship between these parameters may be derived (see, for example, Kroon, 1968).

2.4 Removal of heat from the winding

An excellent general account of heat transfer can be found in many books such as (Knudsen and Katz 1954), (McAdams 1933) and (Kays and London 1964). Here the general principles are applied to the problems involved in the removal of the heat produced in miniature magnetic lenses.

The miniature coil is in direct contact with the water which greatly increases the heat transfer coefficient (h). For heat to be transferred from the coil to the coolant there has to be a temperature difference between the cooled surface and the coolant. This temperature difference will be dependent on the velocity v and the thermal and mechanical properties of the coolant, i.e. viscosity u, density d, thermal conductivity k and specific heat c, and the power transferred to the coolant from the cooled wall.

The power W transferred through a surface of area S at temperature T_s is given by

$$W = hS\ (T_s - T_f) \qquad \ldots\ldots\ldots 2.4.1$$

where T_f is the temperature of the fluid.

Generally the heat transfer coefficient h is expressed in terms of dimensionless parameters in empirical

equations. There are three important numbers to mention in connection with h, the Reynolds number Re = vdH/u, the Prandtl number Pr = c.u/k and the Nusselt number Nu = h.H/k. Here H is the "hydraulic diameter" of a tube. For a circular tube, H is equal to the diameter of the tube, but for tubes of other cross sections, the hydraulic diameter is defined as follows:

$$H = \frac{4 \times \text{Cross-sectional Area}}{\text{"wetted" perimeter}} \qquad \ldots\ldots 2.4.2$$

For a cooling fluid flowing turbulently ($10^4 < Re < 1.2 \times 10^5$) the heat transfer coefficient is determined from the relationship

$$Nu = 0.023\ Pr^{0.4}\ Re^{0.8} \text{ (McAdams 1933)} \ldots\ldots 2.4.3$$

$$\text{hence } h = 0.023\ (c.d^2k^{3/2}/u)^{0.4} V^8/H^{0.2} \ldots\ldots 2.4.4$$

The expression in brackets is a fundamental property of the coolant. Because of the temperature dependence of viscosity it too is temperature dependent. The larger this factor is the larger h becomes and hence the more efficient becomes the transfer process. Of all readily available cooling fluids water is the best, (Montgomery 1969).

Certain specially developed fluorides have higher values of $\frac{cd^2k^{3/2}}{u}$ than water and are also electrical insulators but they require a closed system and recycling plant. Water on the other hand is readily available. If the velocity and the hydraulic diameter are known, the heat transfer coefficient can be calculated.

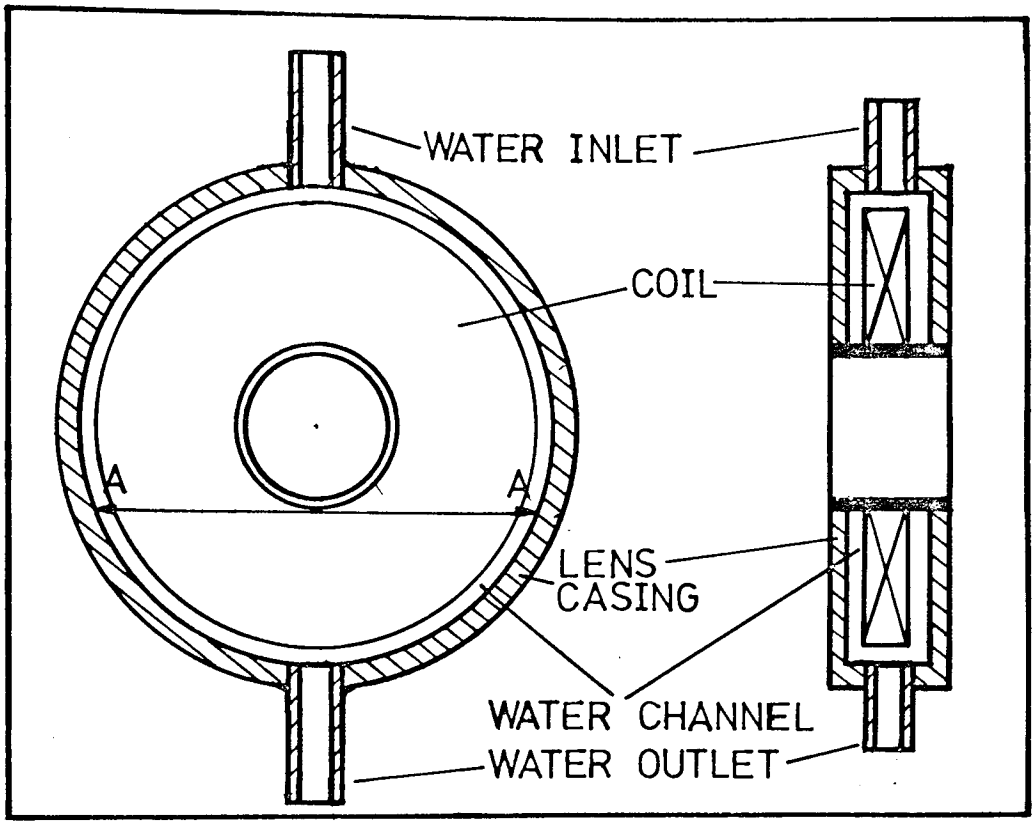

Figure 2.4 Cooling arrangements for a miniature lens.

Figure 2.4 shows the cooling passages in the lens shell; using equation 2.4.2 a value for the hydraulic diameter can be found. In this example H = 4mm. With a water flow of 1 litre/min the velocity v in the inlet pipe to the lens housing will be 1.33 m/sec. The passage cross-sectional area in this lens varies from 12.6mm^2 at the inlet to 62mm^2 at the section AA to 42mm^2 at the lens centre, (Figure 2.4). Assuming an approximate passage cross-section of 40mm^2 the average velocity will be 0.39m/sec, Re $\simeq$ 3000.

Fluid flow is considered laminar if the Reynolds number Re is below 2100 - 2500. At higher rates of flow the fluid is said to flow turbulently. There is a range of flow, however, called intermediate flow and the Reynolds

number corresponding to this range depends on the system geometry and the properties of the fluid. In fact, laminar flow has been achieved at Re = 97000 and turbulent flow at Re $\simeq$ 2000 and the flow therefore is considered turbulent. On the other hand, there was no evidence of mechanical vibration caused by this flow.

To evaluate h, the temperature at which the viscosity u is to be evaluated must be determined. This involves some approximations.

A widely adopted procedure is to define a "film-temperature" T_{film} equal to the mean of the surface temperature T_s and the bulk fluid temperature T_f.

i.e. $T_{film} = (T_f + T_s)/2$

T_{film} is then the temperature at which the fluid properties are to be evaluated.

Table 2.4.1 shows the variation in fluid properties and heat transfer coefficient h for different wall temperatures. The bulk fluid temperature was assumed to be $10^{o}C$.

As the effective thermal conductivity of a wire winding is lower than a tape winding and as there is a layer of insulation between the fluid and the conductors in a wire coil the effective surface temperature of the wire coil will be lower than in the case of a tape winding hence h for a wire coil will be correspondingly lower. This is in fact what is observed in practice.

TABLE 2.4.1

VARIATION IN FLUID PROPERTIES AND HEAT TRANSFER COEFFICIENT FOR DIFFERENT WALL TEMPERATURES

(to 3 significant figures)

T_s ^oC	T_f ^oC	T_{film} ^oC	k $Wm^{-1}{}^oC^{-1}$	u Pas	c $J\,kg^{-1}\,{}^oC^{-1}$	d $kg\,m^{-3}$	h $Wm^{-2}{}^oC^{-1}$
10	10	10	.603	$1.27.10^{-3}$	4190	1000	2450
30		20	.613	$1.06.10^{-3}$	4180	998	2660
50		30	.622	$0.85.10^{-3}$	4180	996	2920
70		40	.631	$0.72.10^{-3}$	4180	992	3140
90		50	.640	$0.60.10^{-3}$	4180	988	3390
110		60	.650	$0.50.10^{-3}$	4190	983	3680
130		70	.659	$0.42.10^{-3}$	4190	978	3960
150		80	.668	$0.36.10^{-3}$	4200	972	4220

2.5 Experimentally determined heat transfer coefficients

In tape coils the temperature drop across the conductor is small hence the film temperature is $\frac{1}{2}(T_f + T_A)\,^oC$ and h should lie between 3000 and 3500 watts $m^{-2}\,{}^oC^{-1}$. It should be possible to obtain a much higher value than this if the tape edges are bare and protrude into the cooling fluid. When constructing these coils it is necessary to have the insulating material overlapping the copper to avoid short-circuited turns, which would degrade the heat transfer at the surface, and reduce the number of turns in the coil. For wire coils the presence of insulating layers between the conductors and the water provide thermal barriers which would give a much

lower value for the film temperature as a large temperature drop is possible across the insulation layers. Moreover, some heat transfer will occur from the outer diameter of coil, effectively increasing S. This effect is important only for coils of small mean diameter values.

In practice a heat transfer coefficient can be defined for the coil winding from equation 2.4.1.

$$h = W/S(T_A - T_f) \qquad \ldots\ldots\ldots 2.5.1$$

The average coil temperature T_A is used in equation 2.5.1 instead of the surface temperature T_s as T_A can be more easily determined in practice; for safety of operation it is preferable to underestimate rather than overestimate h. Putting in typical experimentally measured values of W,S,T_A and T_f in equation 2.5.1, one obtains

Tape Coil
$W/S = 24.10^4$ watts/m^2
$T_A = 80^oC$
$T_f = 10^oC$
$T_{film} = 45^oC$
$h = 3580$ watts/$m^{2o}C$

Wire Coil (D_m = 20mm)
$W/S = 24.10^4$ watts/m^2
$T_A = 120^oC$
$T_f = 10^oC$
$h = 2200$ watts/$m^{2o}C$

Both values of h agree very well with the theory, see Table 2.4.1, especially for the tape, where because of the

small temperature gradient across the tape $T_s \simeq T_A$. The agreement is not as good in the case of the wire coil and if account is taken of the heat transfer from the outer diameter $h \simeq 1500$ watts $m^{-2}\ ^oC^{-1}$. For design purposes it is recommended that this value be used.

2.6 Temperature distribution in the windings

The windings which were constructed during this investigation were in the form of discs; for design purposes heat flow in the radial direction was neglected. The temperature distribution in the coil, assuming axial heat flow only, can be found by developing the heat flow equation for a plane-walled slab containing uniformly distributed heat sources as shown in Figure 2.5, (Eckert and Gross, 1963). In this model the heterogeneous winding is replaced by a homogeneous one having an equivalent composite thermal conductivity; the heat production is assumed to take place uniformly throughout the winding and not simply in the wires of the winding.

There are two further approximations in this treatment; the power dissipated in the coil is calculated assuming a constant average temperature in the coil T_A, and once this power has been determined the value is resubstituted into the model and the temperature distribution calculated as shown in Figure 2.6.

The method of determining the temperature is as follows:-

Let Q (watts m^{-3}) be the heat generated assumed to be independent of x; i.e. resistivity ρ is assumed

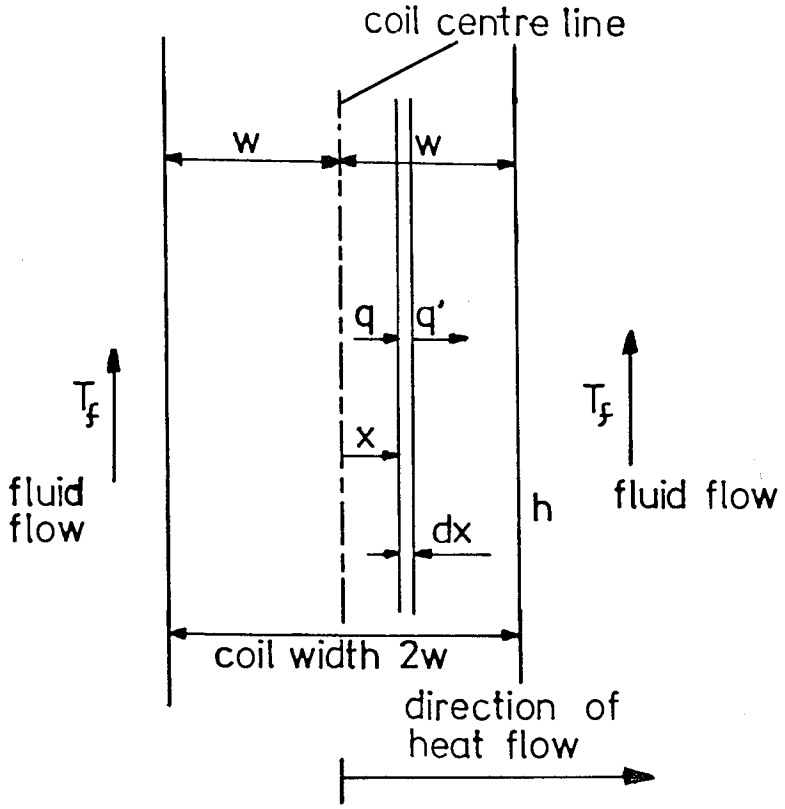

Figure 2.5 Model of heat flow in a water cooled plane walled slab of infinite length and breadth and thickness 2w,with heat sources.

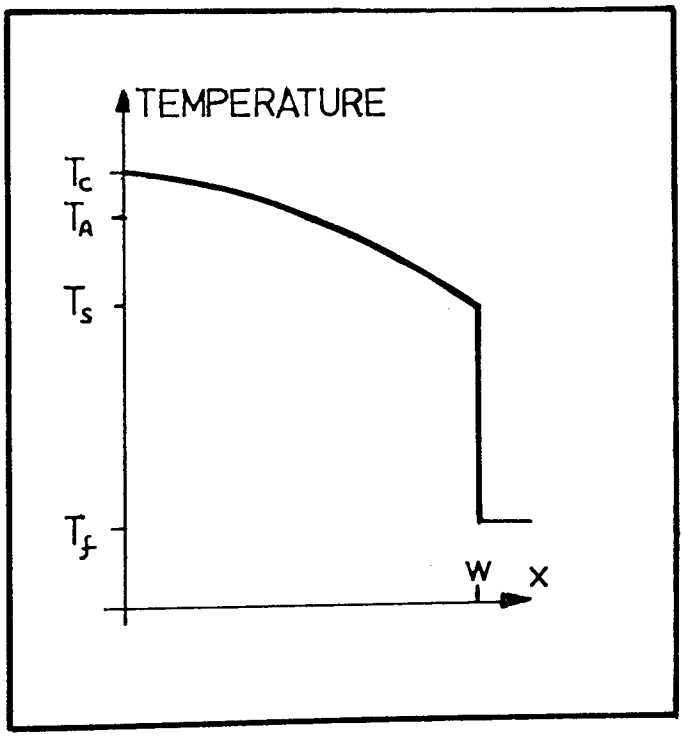

Figure 2.6 Temperature distribution in the plane walled slab. T_f-fluid temperature, T_c-centre temperature, T_s-surface temperature and T_A-average temperature.

not temperature dependant. The power generated will not therefore vary with x.

The heat flow q through a plane a distance x from the coil centre x = o is

$$q = -k\, dT/dx$$

$$= -k\, d\theta/dx \qquad \ldots\ldots\ldots 2.6.1$$

where $\theta = T - T_f$ the temperature above the fluid temperature, and k is the thermal conductivity of the slab.

The heat flowing through the plane at x + dx, q', is:

$$q' = q + \frac{dq}{dx}\, dx$$

$$= -k \frac{d\theta}{dx} - \frac{k d^2\theta}{dx^2} dx \qquad \ldots\ldots\ldots 2.6.2$$

In the steady state the difference (q' - q) must be equal to the heat generation in the slab dx.

$$\text{i.e. } q' - q = Q dx$$

$$\therefore \quad Q = -k \frac{d^2\theta}{dx^2} \qquad \ldots\ldots\ldots 2.6.3$$

which can be integrated to give the temperature distribution.

$$\theta = -Qx^2/2k + C_1 . x + C_2 \qquad \ldots\ldots\ldots 2.6.4$$

C_1 and C_2 are constants of integration.

The boundary conditions are such that the maximum temperature occurs at the centre of the coil

$$T = T_c \quad \text{at } x = 0$$

and the distribution is symmetrical about x = 0, the tangent to the temperature profile at this point must be horizontal.

$$d\theta/dx = 0 \quad \text{at } x = 0$$

And also at the surface of the coil the heat conducted

through the coil must be transmitted to the cooling fluid. Hence at the surface

$$q_s = -h.\theta_s \qquad \ldots\ldots\ldots 2.6.5$$

where the subscript s refers to values at the slab surface i.e. at x = w.

From 2.6.1

$$q_s = -k.(d\theta/dx)_s \qquad \ldots\ldots\ldots 2.6.6$$

$$\theta = Q(w^2 - x^2)/2k + Qw/h \qquad \ldots\ldots\ldots 2.6.7$$

i.e. the temperature profile is a parabola.

From 2.6.7

$$T_c = Qw^2/2k + Qw/h + T_f \qquad \ldots\ldots\ldots 2.6.8$$

The most important temperature in the design of these coils is the temperature at the coil centre, this being the hottest part of the coil, and where the insulation is most likely to fail. The average coil temperature is the easiest to measure experimentally. the average coil temperature above the fluid temperature θ_A is given by

$$\theta_A = (\int \theta \cdot dx)/w$$

between the limits x = 0 and w

i.e. $$\theta_A = Qw^2/3k + Qw/h \qquad \ldots\ldots\ldots 2.6.9$$

and for a tape coil $\theta_A \simeq Qw/h$ as $3k/w >> h$ and it can be seen that this equation is identical to equation 2.5.1.

In practice the average coil temperature can easily be determined by measuring the increase in resistance with temperature. Feeding the coil from a constant current supply has the advantage of making it easy to observe the rise in temperature with time. Current

through the coil heats the wire which increases the resistance and a corresponding increase of voltage is necessary to maintain the constant current.

The resistance of a wire coil R was measured and current passed through it in stages; the voltage V needed to drive this current I through the coil was recorded. When the supply is first switched on the voltage needed to drive current I through the coil is $V_C = I.R_C$. After the coil has reached a steady thermal state the voltage needed will have to rise to V, due to increased temperature of the coil and hence increased resistance. The percentage increase in voltage is a measure of the temperature rise and is given by

$$100(V - V_C)/V_C \qquad \text{.....2.6.10}$$

An increase of 40% for copper wire indicates a temperature rise of about $100^{\circ}C$; this was considered the maximum permitted temperature rise for safe operation of the coils, as can be seen in the following treatment.

2.7 The thermal conductivity of the winding

The thermal conductivity of a tape winding is simply the thermal conductivity of the conductor as heat is assumed to flow entirely axially, and there is no insulation to impede the heat flow to the cooling fluid.

In the case of the wire winding the problem becomes more difficult. Kroon (1968) has published a method for calculating k for coils wound non-orthocyclicly. He also suggests that winding coils orthocyclicly would give values of k of about 3-4 Watts.m^{-1}.$^{\circ}C^{-1}$, see Figure

2.7. A simple model can be described in which the winding is replaced by slabs (see Figure 2.8).

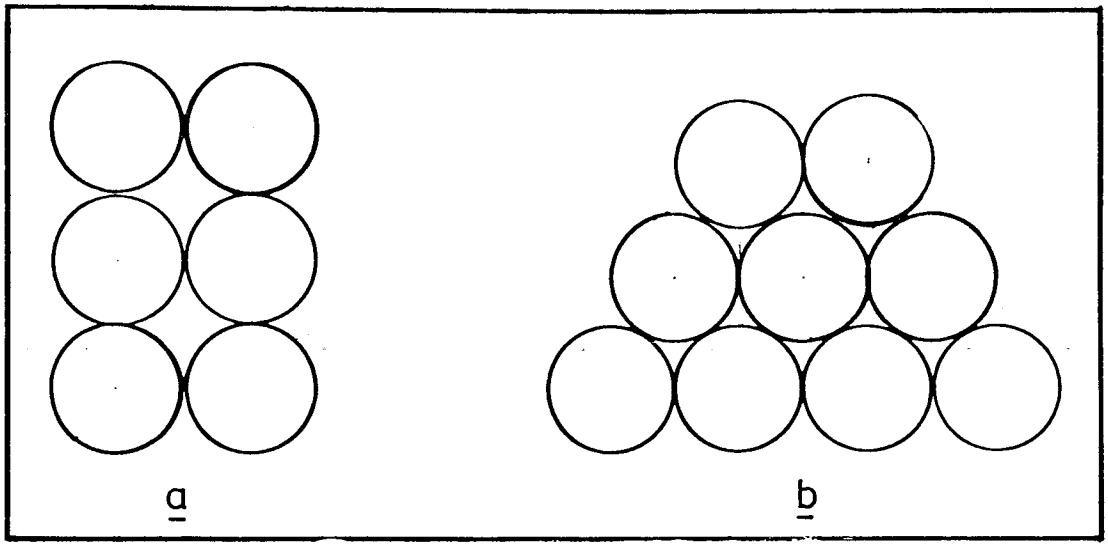

Figure 2.7 (a) Non-orthocyclic and (b) orthocyclic windings of wire with circular cross-section.

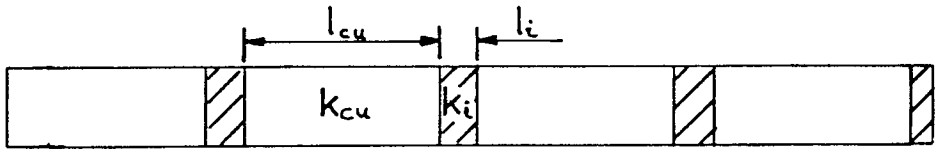

Figure 2.8 Thermal conductivity model used to calculate k.

The thermal conductivity of this model is given by:

$$(l_{cu} + l_i)/k = l_{cu}/k_{cu} + l_i/k_i \quad \ldots\ldots 2.7.1$$

the thickness of the insulation being the dominant term. In the non-orthocyclic case l_{cu} will be less than the wire diameter and l_i will be greater than the insulation thickness. It is not so easy to say what values to attach to l_{cu} and l_i in the orthocyclic case. As an approximation

l_{cu} will be assumed to be the wire diameter; since this distance is not as critical as l_i the errors introduced will be small. As a first approximation l_i will be assumed as the insulation thickness between the wires at the closest point, this will not be a gross over-estimation as in the orthocyclic coil and the semi-orthocyclic coil the interstices are partly filled with copper and provide a further path for heat flow.

Typical values for l_i are 0.0381 - 0.0508 mm which give values for thermal conductivity of k = 4 - 7 Watts.m^{-1}.$^oC^{-1}$. The maximum temperature that the wire insulation can withstand is approximately 180^{o}C. Assuming a cooling fluid temperature T_f at 20^{o}C and and typical values for w, h and k, equation 2.5.4 can be solved for Q.

Typically Q = 0.1 - 0.5 .10^8 Watts/m^3 depending on the values of w, h and k used.

Substituting this value of Q in equation 2.6.9 the maximum average temperature rise can be found,

θ_A = 100^{o}C, or T_A = 120^{o}C

to ensure that the coils are in no danger of being burnt out. Now that a maximum value for Q has been determined and once the coil dimensions are fixed, i.e. its volume is known, the maximum power input to the coil is fixed, i.e.

$$W_M = Q.\lambda.U \text{ Watts} \qquad \text{.....2.7.2}$$

In every calculation the emphasis has been on safety as the time needed to burn out a miniature lens winding working at these high powers is measured in minutes. If the water supply is suddenly reduced or rises

in temperature the heat transfer will be reduced; it is thus advisable to have a margin of safety in these lens windings. Once the integrity of the coolant supply is assured, it will be possible to increase the performance of these lenses. Until such time, however these windings should be operated conservatively.

3. CONSTRUCTION OF THE MINIATURE LENS WINDINGS

3.1 Copper tape windings

Previously a pancake lens using a tape-wound coil had been built for the micro-Kossel camera in the Department of Metallurgy, Liverpool University. This lens had a coil wound from 0.1 mm thick copper tape with dimensions D_2 = 110 mm and D_1 = 40 mm and having 275 turns. Under operating conditions it was apparent that this coil was capable of running at a much higher current density than had been previously estimated. A series of experiments was designed using coils produced from copper tape having half the thickness of that used in the Kossel camera lens. As the inner diameter D_1 was also reduced, this lead to a considerable reduction in the size of the finished coil. The dimensions of the new coil were; inside diameter 16.6 mm, outside diameter 50 mm, compared with 40 mm and 110 mm respectively for the original design. For this coil D_2/D_1 = 3.01; from Figure 2.2 a power input of some 450 - 550 Watts would be required to produce 4000 A-t, assuming it is possible to obtain this performance in the temperature range 15 - 115 ^{o}C. An iterative method can be employed to determine the operating characteristics of the winding. For example, assuming that 550 Watts are dissipated in the winding, Figure 2.2 predicts an average coil temperature T_A of $(T_f + 60)^{o}$C. The resistance of the coil at this temperature would be 2.44 ohms and the current required to produce 4000 A-t would be 14.5 Amps, giving a power

requirement of 513 Watts, some 40 Watts lower than the initial assumption. If the above procedure is repeated with an initial estimate for power input = 500 Watts, the characteristics obtained are; $T_A = (T_f + 55)^{o}C$

$R_H = 2.4$ ohms

$W = 504$ Watts.

As 504 Watts is quite close to the assumed value 500 Watts the process is discontinued.

Table 3.1.1 shows the experimental values of power, current, voltage and resistance. The values for I = 15 Amps compare very favourably with those calculated.

TABLE 3.1.1

EXPERIMENTALLY MEASURED VALUES OF POWER, CURRENT, VOLTAGE AND RESISTANCE OF THE COPPER TAPE COIL

Current I Amps	Voltage V volts	Power W Watts	Resistance R ohms
7.0	13.5	94.5	1.93
10.0	21.1	211.0	2.10
15.0	36.0	540.0	2.40
16.7	41.0	685.0	2.46

From the table it can be seen that although this coil functions as was intended, it is not an optimum design. As the power supply can deliver 25 Amps at 40 volts, an optimised coil would have 200 turns and produce 5000 A-t. Further examples of optimisation of coils are given later in the chapter;the object of this exercise was to show that the miniaturisation techniques developed work in practice, and that the original large winding of the Kossel camera

lens could be replaced by a much smaller unit. The construction remained the same, namely each winding was insulated from the next by Melinex tape 9.0 μm thick. Figure 3.1 shows the three ways of constructing a tape coil.

The main difficulty with the tape coils was in insulating one turn from the next. The coils were produced by interlacing 'Melinex' tape with copper. It was intended to undercut the Melinex insulation to increase the turbulence in the water flow and so enhance the heat transfer, see Figure 3.1a.

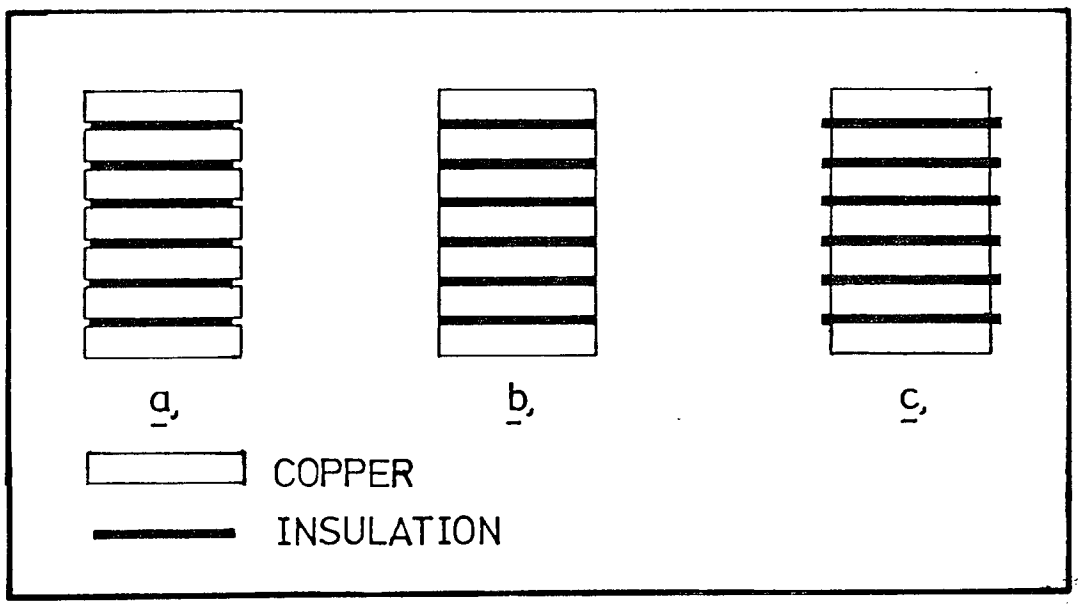

Figure 3.1 The three methods of winding copper tape coils

The first coil was wound with Melinex tape of the same width as that of the copper tape (Figure 3.1b). Unfortunately, several turns were found to be short circuited. This was due to the edges of the copper tape being burred. After mechanical grinding and subsequent etching in ferric chloride, some edge burrs still remained.

The coils that were finally produced had the Melinex tape slightly overlapping the copper, (Figure 3.1c). Three types of tape coil were produced from copper tape of width w = 5 mm, thickness 0.0635 mm ($2.5 \cdot 10^{-3}$ inch) and Melinex insulation thickness = 9 μm.

(1) Singly-wound coils of typical dimensions D_i = 16.6 mm and D_o = 50.0 mm.

(2) A double coil; two coils are wound on a common copper former; the coils are wound in opposite directions. The inner end of each coil is connected to the copper former. The two outer connections then serve as input and output wires resectively. This design removes the need for a central connection in the critical region near the lens axis. This ensures that the flux from each coil is in the same direction, i.e. the fluxes add.

(3) A double-wound coil with coils wound in the same direction with connections again made to the outer turns. The two coils must be separated by a ferro-magnetic sheet, since the magnetic fluxes of the coils now oppose each other. This design produces a rotation-free lens winding which is desirable in projector lenses in electron microscopy.

The construction of tape coils is straightforward given the availability of good quality copper tape of the desired width and thickness. At the time of carrying out these experiments tape of adequate quality was not available. Further improvements in the performance of tape coils will depend on devising reliable methods of

construction. Methods suggested include:-

(1) Rolling of enamelled wire into a tape.

(2) Coating the tape with a polyurethane or other suitable varnish and then if necessary removing the varnish from the edges, before or after the coil has been wound, in order to increase heat transfer.

3.2 Comparison of copper tape and enamelled copper wire windings

Windings of standard enamelled copper wire are easy to manufacture. A series of experiments was therefore conducted on copper wire coils with enamel insulation. The object was to determine what performance could reasonably be expected from wire coils of optimum shape, compared with that from tape windings, of comparable dimensions and geometry. The results could then easily be extrapolated for lenses with tape windings.

A wire coil was constructed having similar geometry to that of the miniature tape coil discussed in section 3.1. For the wire coil N = 220 turns, $\lambda = 0.64$, R = 1.63 ohms and a = 0.245 mm^2. A new tape coil with the same number of turns was constructed for comparison purposes. It was seen in Chapter 2, that the heat transfer coefficient for a particular wire-wound coil was some 50% less than that of a tape coil. Clearly the excitation produced by the tape coil will be appreciably greater than that produced by this wire coil having the same geometry. Using the methods set out in Chapter 2, it was found that the maximum ampere turns expected from the wire coil would be 3330 A-t for the maximum safe power dissipation of about

567 Watts, as given by equation 2.7,2. The coil was constructed and tested experimentally. It produced 3300 A-t for 520 Watts input, agreeing well with the expected values. The results can be compared with those from the tape coil; for ease of comparison Figure 3.2 shows the curves of power against $(NI)^2$ for both coils. Straight lines on this graph represent hypothetical coils operating at constant temperatures; consequently power is proportional to $(NI)^2$ since the resistance of the coil remains constant. Where the experimentally observed curve of power versus $(NI)^2$ intersects such a line, the mean temperature of the coil at that point is given by the temperature corresponding to that of the straight line.

It can be seen from the graph that the mean temperature of the tape coil increases only gradually with increasing power input, whereas the wire coil rapidly rises to the temperature at which the insulation is in danger of breaking down (T_A = 120 ^{o}C). The curves f and g on Figure 3.2 also show the corresponding temperature rise of the winding (right hand scale) against $(NI)^2$. From Figure 3.2 the temperature of the wire winding is shown as 140^{o}C, some 20^{o}C higher than expected. The calculation of the heat transfer coefficient at this point yields h =1250 Watts.m^{-2}.$^{o}C^{-1}$, somewhat lower than the value assumed. As the coil has been conservatively designed it was possible to supply an extra 140 Watts to the coil without damage. At this power the coil gave 3480 A-t for $T_A \simeq 160^{o}$C, the maximum permissible temperature. It is apparent that to

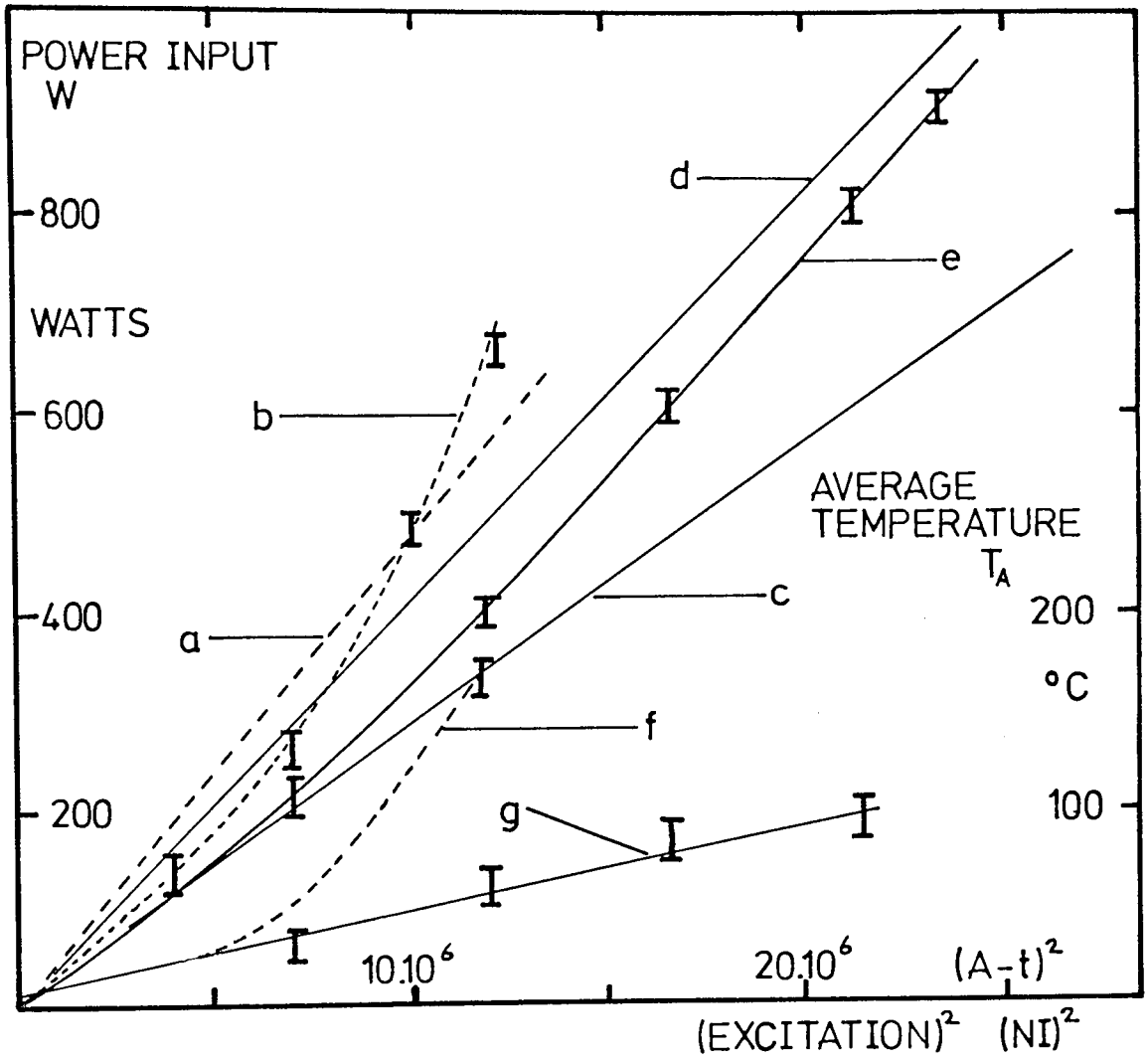

Figure 3.2 Power input W and coil average temperature T_A as a function of lens excitation squared $(NI)^2$ for tape and wire coils.
a - calculated power input W for a wire winding with constant average coil temperature $T_A = 120^oC$
b - measured power input W for a wire winding.
c - calculated power input W for a tape winding with constant average coil temperature $T_A = 15^oC$
d - calculated power input W for a tape winding with constant average coil temperature $T_A = 120^oC$
e - measured power input W for a tape winding.
f - average temperature T_A of a wire winding
g - average temperature T_A of a tape winding.

obtain worthwhile performance from a wire wound coil the coil centre temperature T_c must be kept below the failure temperature of the insulation. This can be achieved by making one of the coil dimensions smaller than the other i.e. a wire wound coil must be in the form of a thin disc or a thin solenoid. This construction limits the number of insulating layers between the coil centre and the cooling fluid thus allowing an easier passage of heat out of the coil. A further type of construction is possible; in which the dimensions $(D_2 - D_1)$ and w are both small. This method was used for the coils of the experimental snorkel lens described in section 3.4. It is therefore not always possible to produce a satisfactory wire wound coil to replace a tape coil without a change of geometry, some further reductions in dimensions may be necessary in practice. This point can be further emphasised by considering Figure 3.3, a plot of input power against θ_A for tape and wire coils; this shows the superior heat transfer characteristics of the tape winding over that of the enamelled wire winding. The poor heat transfer characteristics of the wire coil are largely due to the large temperature drops across the internal insulation layers, which produce a correspondingly lower surface temperature at the coil surface. The heat transfer at the surface is a function of the surface temperature and will therefore be lower than that of a tape wound coil. A secondary factor is the different types of surface that the coils present to the water for heat dissipation. The

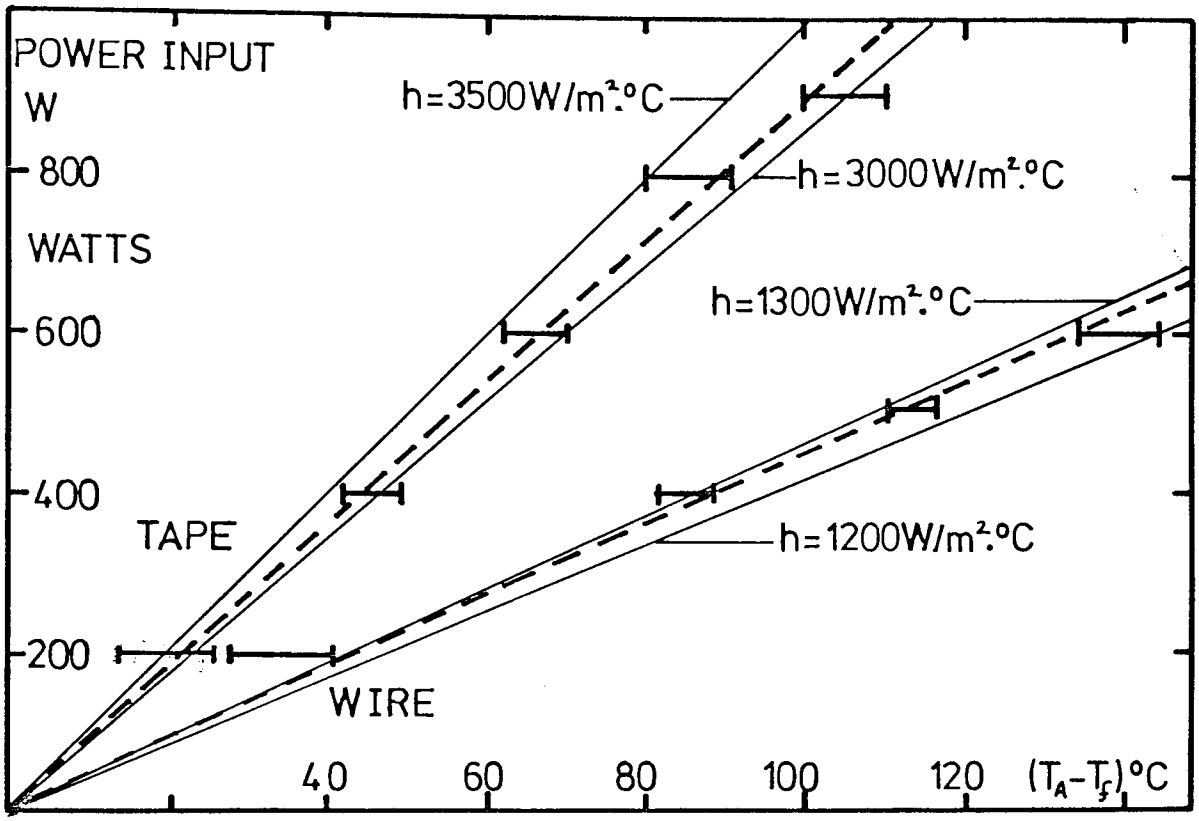

Figure 3.3 Power input W as a function of average temperature rise in a coil, $\theta_A = (T_A - T_f)$. Fluid temperature $T_f = 15^{\circ}C$.

tape has bare conductors, slightly overlapped by Melinex tape insulation, but nevertheless directly immersed in the cooling fluid, while the wire winding has a layer of insulation between its conductors and the cooling fluid. This will also affect the surface temperature and heat transfer coefficient as already mentioned.

Because there is only a small temperature difference across the tape it should be possible to operate the tape coil $10^{\circ}C$ or so below the failure temperature of the insulation provided the water supply is

maintained. A further step would be to determine what happens to the heat transfer coefficient h when the water starts to boil, as heat transfer by boiling is very efficient. This heat transfer regime may of course cause vibrations in the lens, which cannot be tolerated. This may be overcome by reducing the pressure in the neighbourhood of the coil. In the wire winding shown the temperature at the centre of the coil would reach the insulation failure temperature before the surface temperature could reach the boiling point of the cooling fluid.

The straight lines on Figure 3.3 refer to constant heat transfer coefficients. The uncertainty in the experimental points prohibit any precise quantitative statements being made about the variation of heat transfer coefficient with temperature.

3.3 Comparison of the performance of the tape and wire coils

At low power, e.g. 200 Watts, the tape coil gives 2600 A-t to the wire coils 2300 A-t, 13% more. At the higher power of 600 Watts, the tape gives 4100 A-t to the wire coil's 3400 A-t, 21% more. A similar trend is seen if the power required to produce a given number of ampere turns is examined, the higher the number of ampere turns required a proportionately higher amount of power is required in the wire coil than in the tape coil. For the same ampere turns a wire coil will always need more power than a tape coil. For example, at low excitation (2000 A-t) the power input is similar, 140 Watts for the wire coil and 120 Watts for the tape coil. For 3100 A-t 50% more power

is required in the wire coil, i.e. the wire coil draws 480 Watts to the tape coil's 320 Watts. Power input/degree temperature rise for a tape coil is twice that of the wire coil 8.5 Watts/^{o}C to 4.0 Watts/^{o}C respectively, i.e. the wire coil will always have a higher internal temperature than a tape coil for the same power input, because the thermal conductivity of wire winding is lower. To improve the heat transfer in practice it is possible to gain some heat transfer from the cylindrical surface of the coil by choosing a suitable value of the outer diameter D_2. Wire coils of 120 turns were made with dimensions as follows D_1 = 10 mm, D_2 =30 mm, and width w = 5 mm. The maximum safe temperature of the winding was set at 120^{o}C; the resulting safe number of ampere turns can be estimated from Figure 2.2. These coils are shown in Figure 3.4 placed on top of the conventional winding they replace. As a result of these experiments it was clear that a considerable improvement in the design of magnetic lenses should be possible with such small coils. For example if the excitation NI = 2000 A-t, Figure 2.2 gives a power requirement of 200 Watts for this particular geometry. This was verified experimentally. In order to make progress as quickly as possible these small coils were chosen as the standard windings for the series of miniature lenses described in this thesis.

However, further worthwhile technical improvement in performance seems possible. Preliminary experiments suggest that the heat transfer coefficient can be improved

Figure 3.4 Two miniature lens windings supported by the conventional winding they replace.

considerably by using wire of square cross-section or by reducing the coil thickness to 2.5 mm or by reducing the number of layers in the coil. In the long term, tape windings have overwhelming advantages. The windings of a tape coil are more compact, have greater axial symmetry, use less copper for a given number of turns than the wire coil, and the temperature rise in a tape is typically less than that of a wire coil by a factor of two or three. In the present investigation the ease of manufacture of a wire coil was of prime importance; it was therefore decided to to use wire coils of optimum design. Care must be taken with enamelled covered wire to avoid pin-holes and other defects in the covering or electrical leakage may be troublesome. Improvements in the techniques of winding wire coils are being constantly made (Taylor 1972).

3.4 Special lens windings (single-pole or snorkel lens winding)

The final version of the snorkel lens, mark IV, had restrictions on the inner and outer diameter. The outer diameter of the lens was kept the same as that of the previous designs to make it compatible with existing adaptors and electron optical components already produced for the 'Intercol' electron optical bench. The inner diameter was fixed by magnetic saturation considerations described fully in Chapter 7. The resulting dimensions of the coil to fit the lens shell are given in Figure 3.5.

An excitation of approximately 4000 A-t was required, i.e. 2000 A-t from each coil. Referring to Figure 2.2 the power inputs, assuming the coils were to

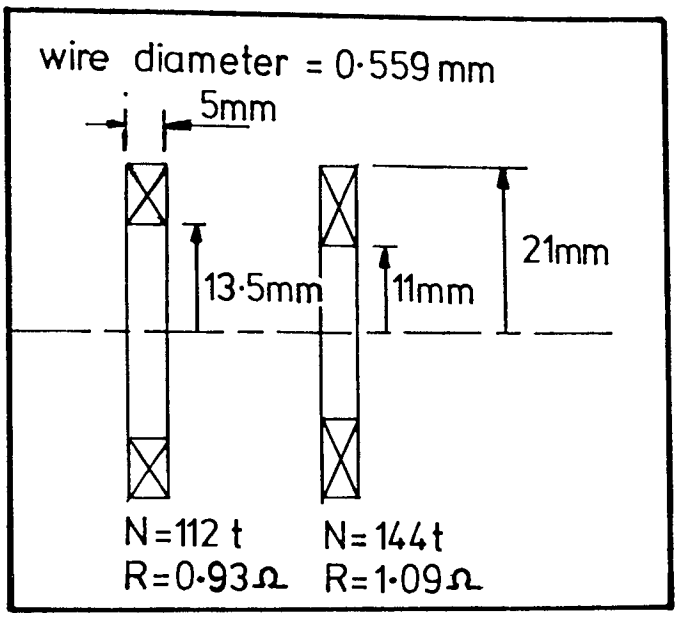

Figure 3.5 Design parameters of the wire windings for snorkel lens IV

run at 120°C, would be 300 Watts per coil taking an average value for D_2/D_1.

The power supply available was rated at 1 kW, (25 Amps at 40 volts). It is possible to supply the 600 Watts of power necessary in two extreme ways:

(1) Maximum voltage limit. V_M = 40 volts, consequently I_M = 15 Amps.

From equation 2.2.2 R_H = 2.67 ohms

equation 2.2.3 R_C = 1.89 ohms

equation 2.2.6 conductor diameter = 0.559 mm (0.022 inch)

(2) Maximum current limit. I_M = 25 Amps, therefore V_M = 24 volts.

From equation 2.2.2 R_H = 1.0 ohms

equation 2.2.3 R_C = 0.7 ohms

equation 2.2.6 conductor diameter = 0.914 mm (0.036 inch)

It is therefore feasible to produce coils for

this lens with wire diameters between 0.559 mm and 0.914 mm. It is preferable to use the larger diameter wire as it would run at a lower current density (30% lower), be thermally more efficient (fewer insulation barriers), and at a lower potential with respect to the lens case (lower leakage currents). However, supplies of 0.559 mm (24 swg) wire were readily available and the coils were wound with this. The finished coils had number of turns and resistances as given in Table 3.4.1 showing good agreement with the predicted values.

TABLE 3.4.1

NUMBER OF TURNS AND RESISTANCE OF THE SNORKEL IV LENS COILS

	N turns	R ohms
Coil 1.	112	0.93
Coil 2.	144	1.09
Total	256	2.02

Assuming a heat transfer coefficient as previously described, the average coil temperature would be 75 - 105 ^{o}C for a coil dissipating 300 Watts. The temperatures of the coils were determined experimentally and are shown in Figure 3.6. The low operating temperature indicates a better value of heat transfer coefficient than the one assumed. This was probably due to the radial extent of the coil being of the same order as the axial extent, thereby increasing the heat transfer.

The conservative nature of the assumptions made in

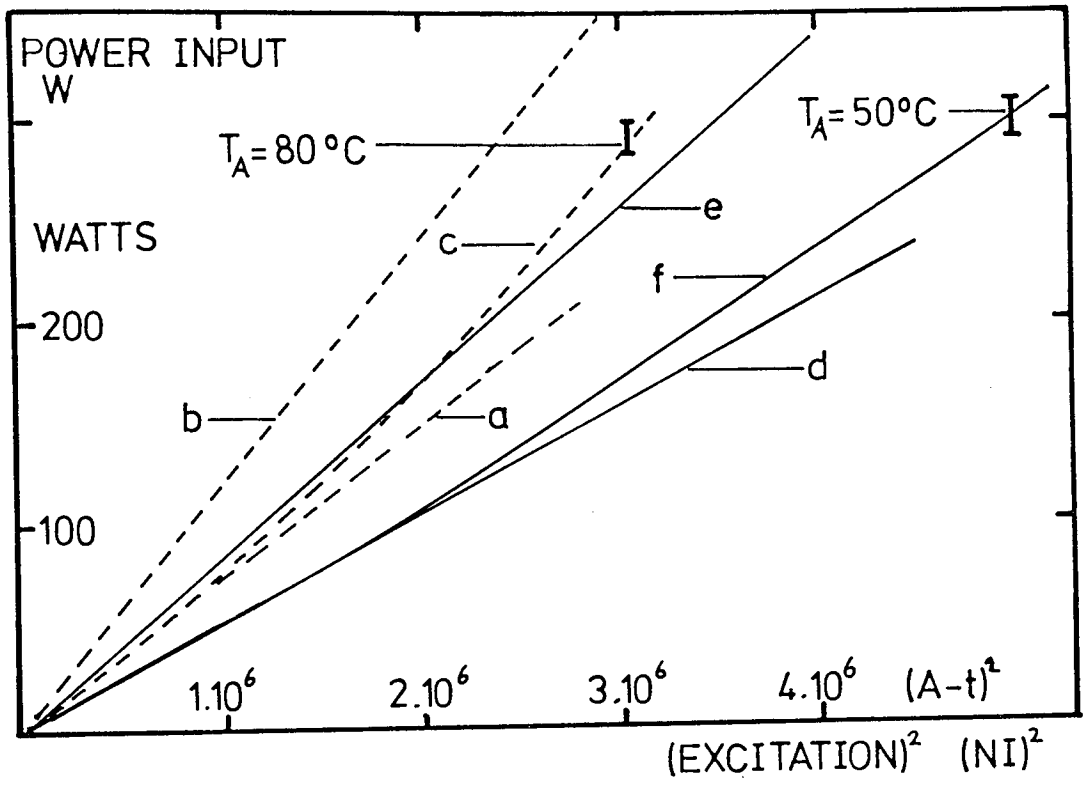

Figure 3.6 Power input W as a function of lens excitation squared $(NI)^2$ for the wire coils made for snorkel lens IV.
a - calculated power input W for the 112 turn coil with constant average temperature T_A = 15°C
b - calculated power input W for the 112 turn coil with constant average temperature T_A = 160°C.
c - measured power input W for the 112 turn coil.
d - calculated power input W for the 144 turn coil with constant average temperature T_A = 15°C.
e - calculated power input W for the 144 turn coil with constant average temperature T_A = 160°C.
f - measured power input W for the 144 turn coil.
I - the operating point of each coil and the calculated average temperature T_A at that point.
Total excitation NI = 4000 A-t.

the foregoing theory is borne out by the low operating temperatures observed in practice. This lens proved very satisfactory in operation. Its reliability enabled rapid progress in the design of special electron optical columns to be made as this lens played a major role in every system produced.

3.5 Coils for the high voltage lens

For the miniature snorkel lens, minimum projector focal length occurred at an excitation parameter $NI/V_R^{\frac{1}{2}} = 14$ (see Chapter 7). A high voltage lens would therefore need 19 800 A-t if it is to operate at its minimum projector focal length at an accelerating voltage of 1 million volts. In the experiments carried out on the million volt electron microscope, the maximum permissible size of the lens was severely limited, as explained in Chapter 10. Consequently the coil dimensions were severely restricted, as shown in Figure 3.7; Table 3.5.1 shows the maximum dimensions that were considered possible in a practical design using ordinary insulated wire.

Table 3.5.1 also shows the ampere turns available from each coil estimated from the geometry and assuming the same current in each coil. Substituting these values in equation 2.1.4, an estimate of the power required for each coil can be made. Table 3.5.2 shows the power required for the desired performance between the temperature limits of 20°C and 120°C, i.e. a total power of between 3.6 and 5.4 kW would be required depending on the working temperature; this corresponds to a Q of

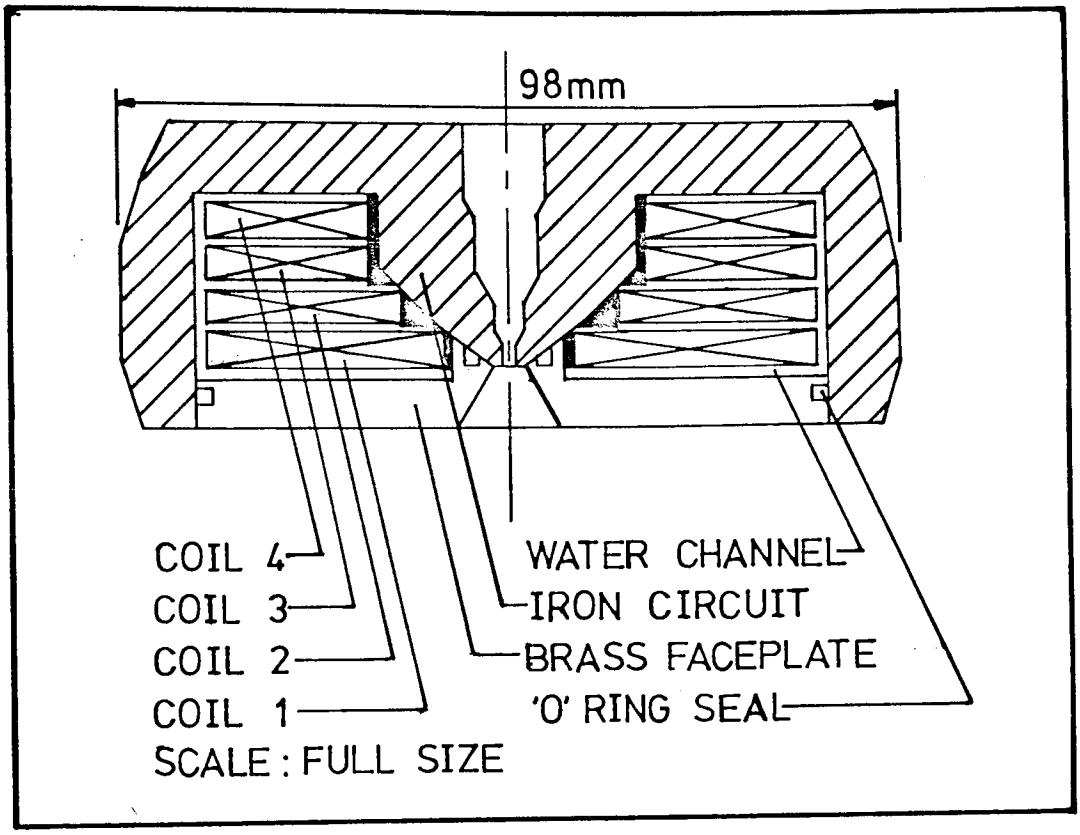

Figure 3.7 The miniature high voltage lens, showing the position of the four coils around the single polepiece. The iron circuit (shown sectioned) is machined from a single billet. Two 'O' ring seals form the water-tight joint between the brass face-plate and the iron circuit. The dimensions of the coils are given in table 3.4 and the iron circuit and brass face plate in figure 10.3

0.5×10^8 Watts/m , which is just on the upper limit of the maximum dissipation given in Chapter 2. If 5 kW were available, this lens could be made to operate at minimum projector focal length assuming that optimum values of h and k could be achieved. At the time, only two power supplies were available. These were capable of delivering 1.5 kW each; it was therefore decided to design a set of coils so that the full 3 kW could be used to drive the lens under optimum conditions. Clearly, this entailed

TABLE 3.5.1

DIMENSIONS OF THE MINIATURE HIGH VOLTAGE LENS COILS

Coil No.	1	2	3	4
D_1 (mm)	15.0	27.0	35.0	35.0
D_2 (mm)	78.0	78.0	78.0	78.0
D_m (mm)	46.5	52.5	56.5	56.5
D_2/D_1	5.2	2.9	2.2	2.2
D_2-D_1 (mm)	63.0	51.0	43.0	43.0
NI (A-t)	6237.0	5049.0	4257.0	4257.0

TABLE 3.5.2

POWER REQUIREMENTS OF THE MINIATURE HIGH VOLTAGE LENS COILS

Coil No.	1	2	3	4	Total
Power at 20°C Watts	1000	930	860	860	3650
Power at 120°C Watts	1500	1370	1270	1270	5410

accepting a reduction in lens excitation. Substituting the coil dimensions and the power available into equations 2.2.9 and 2.2.10, the maximum number of ampere turns NI_M were found to be 15 700 A-t for the optimum wire diameter = 0.814 mm (0.032 inch). This was certainly adequate for a preliminary experiment. Table 3.5.3 summarises the details of the coils actually constructed.

The coils were built and tested experimentally; the electrical performance is summarised in Table 3.5.4. The front coils, coils 1 and 2, produced 8575 A-t for

TABLE 3.5.3

THE CONSTRUCTED COILS FOR THE HIGH VOLTAGE LENS

Coil No.	1	2	3	4	Total
R ohms at 20 ^{o}C	0.95	0.87	0.76	0.76	3.34
N turns	189	153	127	127	596
NI A-t I=25 Amps	4725	3825	3175	3175	14 900

TABLE 3.5.4

ELECTRICAL PERFORMANCE OF THE HIGH VOLTAGE LENS COILS

Front coils N = 343 t					Back coils N = 252 t					Total	
V	W	I	NI	T_A	V	W	I	NI	T_A	W	NI
10	50	5	1715	20						50	1715
20	200	10	3430							200	3430
30	450	15	5145							450	5145
42	840	20	6860							840	6860
56	1400	25	8575	70						1400	8575
					8	40	5	1260	20	1440	9835
					17	170	10	2520		1570	11095
					27	405	15	3780		1805	12355
					44	880	20	5040	130	2280	13615

V- volts, W- Watts, I- Amps, NI- A-t, T_A- ^{o}C.

1.4 kW and had an operating temperature of 70°C. The back coils, coils 3 and 4, gave 5040 A-t for 880 Watts, and had an operating temperature of 130°C, some 50°C above the expected value calculated from heat transfer considerations. The conclusion was drawn that the cooling water supply to the rear coils of the lens was inadequate. A lens construction of this type, with an improved water supply, would therefore be expected to produce 15 000 A-t. This is sufficient for operating at minimum focal length at an accelerating voltage of 700 kV. For a lens of this size to work at its minimum projector focal length for V_R = 1 MV, it would be desirable to use a tape winding.

Tape windings

It is of interest to evaluate the power that would be required to operate this million volt projector lens using tape windings having the same dimensions as the wire coils. This result is shown in Table 3.5.5.

TABLE 3.5.5

POWER REQUIREMENTS OF THE TAPE COILS FOR THE HIGH VOLTAGE LENS

Coil No.	1	2	3	4	Total
Power at 20°C Watts	860	800	740	740	3140
Power at 120°C Watts	1290	1180	1090	1090	4600
Excitation A-t	6237	5049	4257	4257	19 800

The optimum tape thickness would be approximately 0.1 mm. Increasing the tape thickness while keeping the insulation

thickness constant increases the packing factor λ which also leads to reduction in the input power.

Estimating the average temperatures T_A of the windings using equation 2.6.9 will give a realistic estimate of the power input for a given lens excitation. The average temperature of the wire windings at 20 000 A-t is in the region of 120°C; the coils would therefore consume about 5 kW. The corresponding tape winding would operate at about 65°C for 20 000 A-t, reducing the power input to about 3.7 kW. With the available 3.0 kW supply, it would have been possible to produce an excitation of 18 800 A-t in a tape winding corresponding to $NI/V_R^{\frac{1}{2}} = 13.3$ and $f_p = 1.01 f_{pmin}$. This compares favourably with the 15 700 A-t to be expected from a wire winding at $NI/V_R^{\frac{1}{2}} = 11.1$ and $f_p = 1.13 f_{pmin}$. These examples illustrate the considerable advantage of tape windings over wire windings when size and power requirements are important. In commercial equipment it would therefore be desirable to make use of tape windings wherever possible. This is illustrated by the preliminary design for a high voltage microscope lens shown in Figure 10.2 of Chapter 10. It is not in fact possible to use wire wound coils to produce the required 20 000 A-t excitation in this design, as the power density would be too high in the limited winding space. It would however, be just possible to use tape windings for this excitation. From equation 2.6.9 the average temperature T_A for the tape winding would be 115°C, a perfectly acceptable value. The power required for an

excitation of 20 000 A-t is 3.8 kW as shown in Table 3.5.6 which also gives the individual coil dimensions and performance.

TABLE 3.5.6

CALCULATED DIMENSIONS, EXCITATION AND POWER REQUIREMENTS OF TAPE COILS FOR THE HIGH VOLTAGE LENS SHOWN IN FIGURE 10.2

	Coil 1	Coil 2	Total
D_1 mm	15	27	
D_2 mm	78	78	
NI A-t	11052	8947	20000
Power at 120°C Watts	2286	1524	3810

With the limit of 3 kW set at the time by the available power supply the lens design of Figure 10.2 could have been expected to produce 15 700 A-t. This is the same as that expected from the wire wound lens design with with improved water supply as previously described. The decision to use wire wound coils was therefore based entirely on the speed and convenience of manufacturing these coils.

4. FLUX DENSITY DISTRIBUTIONS AND THEIR FOCAL PROPERTIES.

4.1 Calculation of the axial flux density distribution

One of the fundamental problems of electron optics is the determination of the axial flux density distribution produced by a given lens. Once the distribution is found, the focal properties of the lens can be determined. The methods employed to determine the flux density distribution are similar whether the field is electrostatic, electric or magnetic (Mulvey & Wallington 1969). The classical method is the solution of Laplace's equation for a set of assumed boundary conditions. Unfortunately, only the most simple structures can be analysed by this method. When the shapes of the structure producing the field become more complicated, numerical methods are used in determining the field distribution. The relaxation method (Liebmann & Grad 1951) is one of the best known; it is accurate but needs long computation times, and it can only be applied to plane or axially symmetrical systems. With the increased store size of the large computer, it is now possible to have a very small interval size and so increase the accuracy of the numerical method. Munro (1971) has used this to great advantage in his "finite-element" calculations.

4.2 Lens models

An experimental determination of the field

distribution is often convenient. As Laplace's equation is linear, a given lens structure can be replaced by a scale model and a measurement of the axial field distribution can be made. Instead of determining the flux density distribution analytically or experimentally, several authors have substituted mathematical expressions for the actual field distribution along the lens axis. The two main mathematical models are those of Glaser(1935) and Grivet-Lenz(Grivet:1972). The Glaser model, also called the bell-shaped field , was obtained by considering the flux density distribution along the axis produced by a circular single current loop. Ampere's Law gives the flux density B_z as follows:

$$B_z = B_M/(1 + (z/r)^2)^{\eta} \qquad \ldots\ldots.4.2.1$$

where B_M = maximum flux density at z = 0

r = radius of the loop

η = constant (η = 3/2 for Ampere's Law)

r is given the empirical value

$$r = b/((2)^{1/\eta} - 1)^{\frac{1}{2}} \qquad \ldots\ldots.4.2.2$$

where 2b is the width of the distribution between the "half-value" points.

substituting η = 1 in equation 4.2.2 gives r = b and substituting this value in equation 4.2.1 gives the bell-shaped field.

$$B_z = B_M/(1 + (z/b)^2) \qquad \ldots\ldots.4.2.3$$

Substituting 4.2.3 in the paraxial ray equation

$$d^2r/dz^2 + (e.B_z^2/8mV).r = 0 \qquad \ldots\ldots.4.2.4$$

where r = radial co-ordinate of the electron trajectory

e = the charge on the electron

B_z = the axial flux density

m = the mass of the electron

V = the accelerating voltage applied to the electron

gives;

$$d^2r/dz^2 + (e/8mV).(B_M^2/(1 + (z/b)^2)).r = 0 \quad \ldots\ldots.4.2.5$$

Solution of equation 4.2.5 gives the focal properties of the Glaser distribution.

$$f_p = -b\omega\,\mathrm{cosec}\,\omega\pi \quad \ldots\ldots.4.2.6a$$

$$z_p = b\omega\cot\omega\pi \quad \ldots\ldots.4.2.6b$$

$$f_o = b\,\mathrm{cosec}(\pi/\omega) \quad \ldots\ldots.4.2.6c$$

$$z_o = a\cot(\pi/\omega) \quad \ldots\ldots.4.2.6d$$

where $\omega = (1 + eb^2B_M^2)/8mV$ 4.2.6e

Equation 4.2.1 can be applied approximately to air coils as well as to iron-shrouded coils. Even asymmetrical fields can be approximately represented by combining two half curves of differing half width but having the same peak height. The case above where $\eta = 1$ approximately fits magnetic lenses that are worked near the saturation point of the iron shroud. In the limiting case as $\eta \to \infty$ equation 4.2.1 reduces to

$$B_z = B_M.\exp(-(z.\ln(z/b))^2) \quad \ldots\ldots.4.2.7$$

Equation 4.2.7 gives a good approximate representation to an actual flux density distribution of a shielded lens when the iron shroud is carrying a relatively low flux density. Another mathematical model for the flux density distribution which predicts the properties of real lenses

well is the Grivet-Lenz model (Grivet 1972),

$$B_z = B_M \operatorname{sech}(z/b) \qquad \ldots\ldots\ldots 4.2.8$$

Both these models have had their focal properties tabulated and are both well understood. The bell-shaped field is perhaps simpler in the fact that its properties are expressed in circular functions while the Grivet-Lenz model has its properties expressed in Legendre polynomials.

The square-top field distribution.

The simplest of all the mathematical models is the square-top distribution or the single step lens field. In this model the axial flux density B_z is constant over the axial extent of the lens. The paraxial ray equation then reduces to

$$d^2r/dz^2 + K^2r = 0 \qquad \ldots\ldots\ldots 4.2.9$$

where $$K^2 = eB^2/8mV \qquad \ldots\ldots\ldots 4.2.10$$

Solution of this equation yields

$$r = C_1.\cos Kz + C_2.\cos Kz$$

where C_1 and C_2 are constants of integration and dependent on the boundary conditions. The focal properties are given as

$$f_o/2b = 1/K2b \qquad \ldots\ldots\ldots 4.2.11a$$

$$z_{\hat{o}}/2b = \pi/4bK - 1/2 \qquad \ldots\ldots\ldots 4.2.11b$$

$$f_p/2b = 1/(2bK.\sin 2bK) \qquad \ldots\ldots\ldots 4.2.11c$$

For a weak lens the objective focal length and projector focal length are identical, but as the lens becomes stronger the objective focal point is immersed in the field and in general becomes progressively shorter.

The positions and magnitudes of the second and third projector focal lengths are given by solutions of

the general equation tan 2bK = 2bK. This expression is obtained by differentiating equation 4.2.11c with respect to K and equating to zero. This procedure gives the K values for the minima of projector focal length, and substituting in equation 4.2.11c gives the magnitude of f_p at these points.

The asymptopes are determined from the equation sin 2bK = 0, i.e. where f_p goes to infinity. These results are summarised in Figure 4.1, where NI' = NI for $f_p = f_{pmin}$. Figure 4.1 also shows the normalised focal properties of two unshrouded coils D_2/D_1 = 3 and 19, the double snorkel lens field and a polepiece lens of bore to gap ratio 1 for comparison. It can be seen that the second and third projector focal lengths are very different and depend on the severity of the tailing off of the flux density distribution.

The exponential field model

Another analytical flux density distribution discussed by Glaser (1952) is the exponential field distribution

$$B_z = B_M \exp-(z/b') \qquad \ldots\ldots\ldots 4.2.12$$

where b' = the half width divided by ln 2. This field, when substituted in the paraxial ray equation yields solutions in terms of Bessel functions. The exponential field appears to fit very closely with the field produced by the snorkel type lenses (Mulvey & Newman 1973, Appendix 2). The objective focal properties of such a distribution are independent of excitation for an excitation parameter

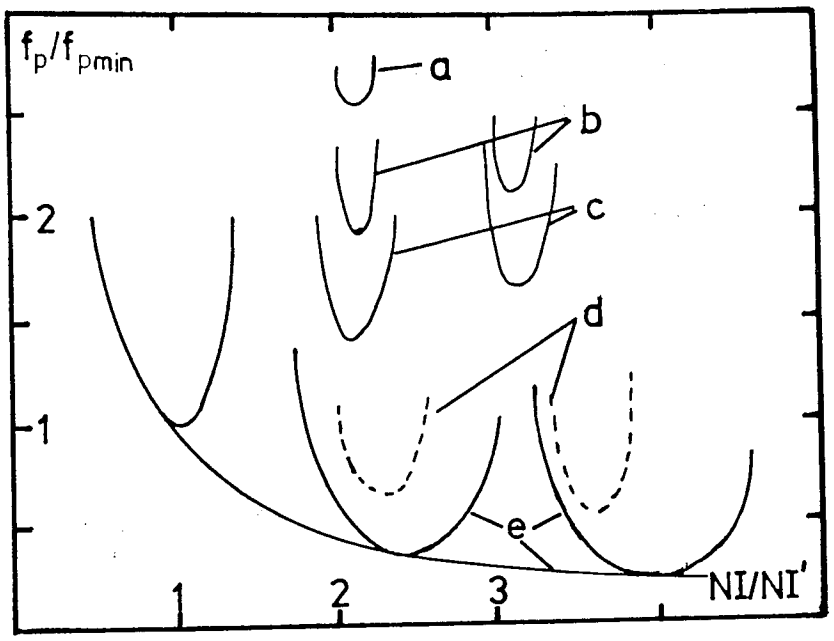

Figure 4.1 Normalised projector focal properties, in terms of f_{pmin} and NI^1, of conventional iron shrouded lenses, iron-free pancake lenses and snorkel lenses. The projector and objective focal properties of the square topped distribution are added for reference.
a - second projector focal length for a double snorkel lens i.e. two snorkel lens distributions placed back to back.
b - second and third projector focal lengths for an iron free pancake lens with outer to inner diameter ratio $D_2/D_1 = 19$.
c - second and third projector focal lengths for an iron free pancake lens with outer to inner diameter ratio $D_2/D_1 = 3$.
d - second and third projector focal lengths for a conventional iron shrouded lens with gap to bore ratio $S/D = 1$.
e - focal properties of a square topped distribution.

NI/NI' = 1. This is also approximately true of the snorkel lens.

4.3 "Full-Field" distributions

The axial field distribution from an iron-free coil can be calculated exactly (Appendix 4), and if such a lens is to be placed in an electron optical system its focal properties are merely read from tables. Hence, if a field distribution from an iron shrouded lens can be fitted approximately to one from an iron-free coil, its focal properties and aberrations can easily be determined from the same tables. Figure 4.2 shows normalised field distributions of three systems. Two iron-free coils of D_2/D_1 ratios 3 and 19 respectively, the Glaser bell-shaped field and the the experimentally measured points for the miniature 100 kV snorkel lens IV (I). Inspection of the data shows that the focal properties of the snorkel lens should be similar to those of an iron-free coil of ratio $D_2/D_1 = 19$. The flux density along the axis of the snorkel lens was measured in the laboratory using a Hall probe. The sensitive part of the probe could be brought up to an axial distance of 1 mm from the pole face. The flux density at the pole face itself could be determined approximately by using a small search coil attached to the face. From these measurements a complete distribution formed by the lens could be produced. Figure 4.2 was then used to determine which iron-free coil has the nearest field distribution to the measured one. In this way the performance of such a lens can be closely estimated.

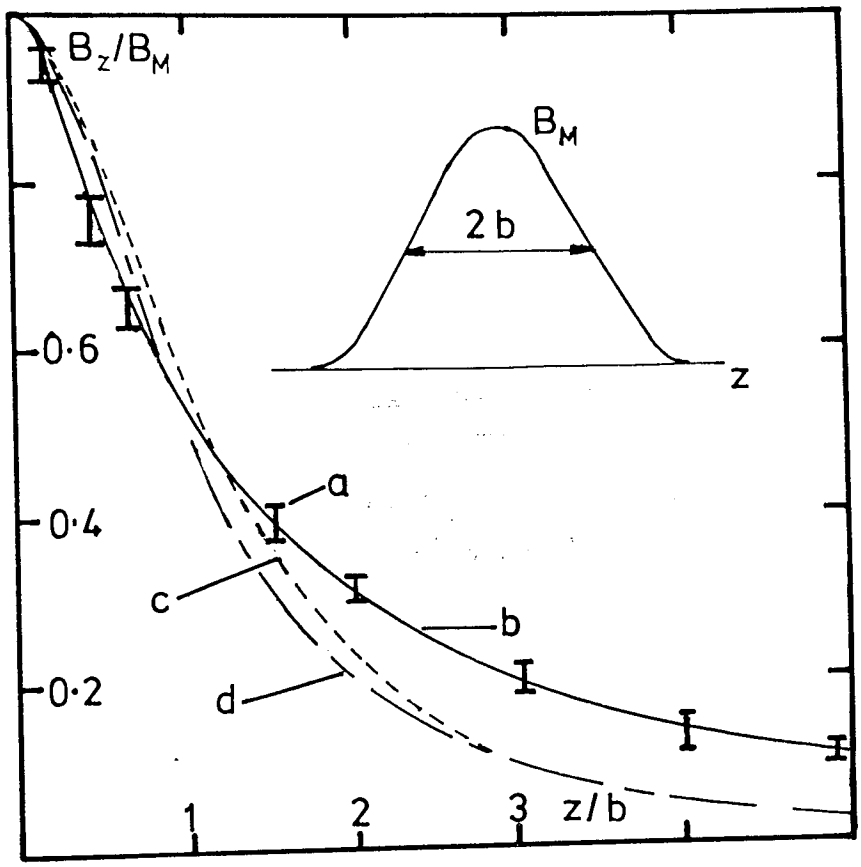

Figure 4.2 Normalised flux density distributions in terms of B_M and b, iron-free lenses and the analytical bell-shaped field lens.
a - Points I on curve b normalised flux density distribution for snorkel lens IV.
b - Normalised flux density distribution for an iron free pancake lens with outer to inner diameter ratio $D_2/D_1 = 19$.
c - normalised flux density distribution for an iron free pancake lens with outer to inner diameter ratio $D_2/D_1 = 3$.
d - normalised flux density distribution for the analytical bell-shaped field lens model.

Two analytical flux density distributions have been found useful in the present experiments; the square top lens and the Glaser bell-shaped field.

The first quadrant of the normalised focal properties is identical for the different lens fields (see Figure 4.1). In the second quadrant the second minimum projector focal length appears to be a very sensitive parameter. With certain lens distributions it is possible to produce a shorter second projector focal length than the first. This property can be seen by considering the two analytical models mentioned above. The sharp cut-off of the square top lens contrasts sharply with the gentle "tailing-off" of the iron-free "pancake" lenses.

The focal properties of the "full-field" system are shown in Figure 4.3. The snorkel lens shown is a double distribution type, i.e. two snorkel distributions placed back to back.

4.4 "Half-Field" distributions

When discussing the snorkel type lens, it is convenient to discuss the properties of the "half-lens". If one half of a symmetrical distribution is removed, the shape remaining is of a similar form to the axial flux distribution of a snorkel lens, i.e. a sharp cut-off occurs near the snout face followed by a gentle slope away from the peak.

The "half-field" focal properties of iron-free coils have been examined mathematically; the results

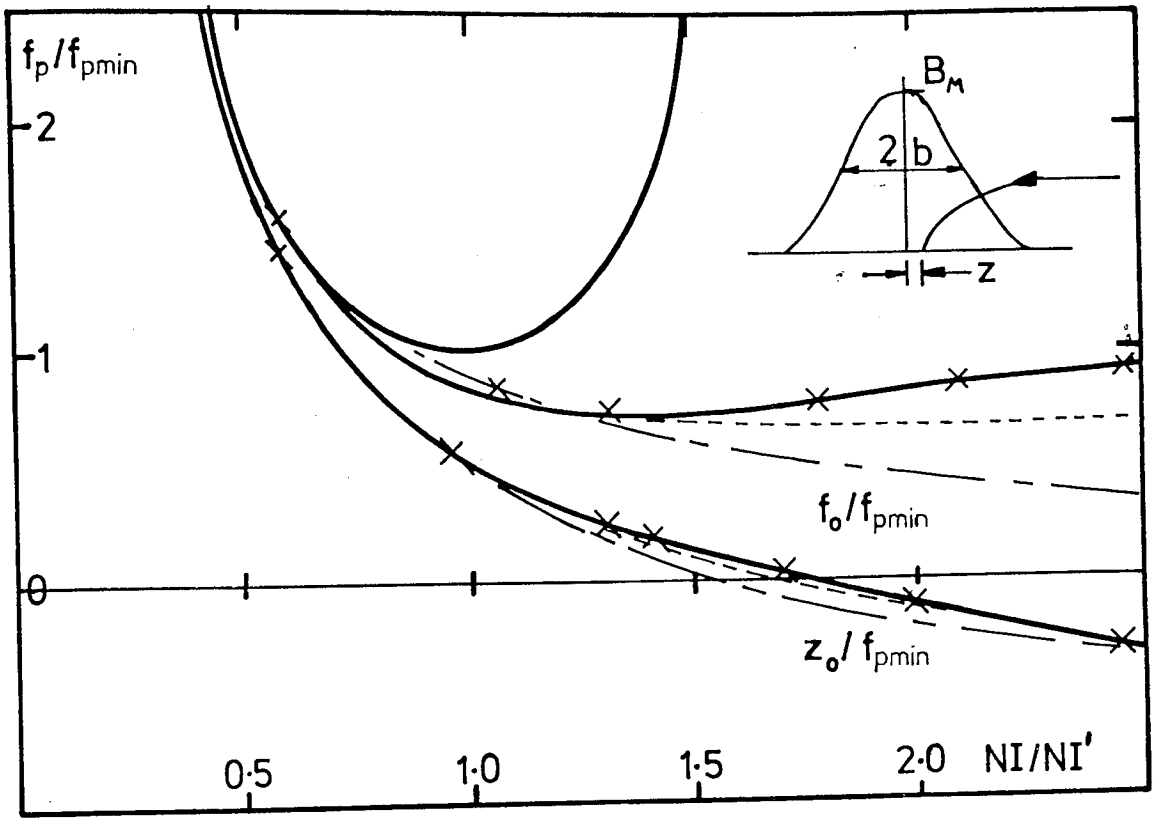

Figure 4.3 Normalised "full-field" focal properties in terms of f_{pmin}, and NI' of:

——— – ——solenoid lens

- - - - - - - - - -iron-free pancake lens with outer to inner diameter ratio $D_2/D_1 = 3$

———————iron free pancake lens with outer to inner diameter ratio $D_2/D_1 = 19$.

× × × × × × focal properties of a double snorkel lens IV distributions placed back to back.

together with the snorkel lens are shown in Figure 4.4 Note that Figure 4.4 shows that the half-field lenses have two objective focal lengths, one arising from the trajectory coming up to the lens in one direction and one for the trajectory passing through the lens in the opposite direction. This type of lens can be used in either mode but the direction in which a parallel beam of electrons enters the gentle slope corresponds to very low

aberrations. The smooth "tail-off" of the field distribution resembles that of the iron-free coil; the curves for snorkel lens IV and the iron-free coil $D_2/D_1 = 19$ are almost identical. The main difference between the two systems becomes apparent when considering the variation of the second projector focal length. By a suitable choice of D_2/D_1, and possibly the position of the snout in the snorkel lens, it should be possible to produce a second projector focal length lower than the first. Figure 4.4 also shows the field distribution kindly calculated by Dr. E. Munro for the snorkel lens again showing good agreement with the "half-lens" distribution.

It therefore seems that the majority of the properties of the snorkel lens could be described using "half-field" distributions. Further examination of the snorkel field distribution shows a resemblance to a type of exponential field distribution (Glaser 1952). Results using this approximation appear to be in good agreement with calculated values (Marai & Mulvey 1974).

The focal properties of the lens systems described were calculated using two computer programs "FLUXBZ" and "FLUTRAG" both of which are discussed in Chapter 5.

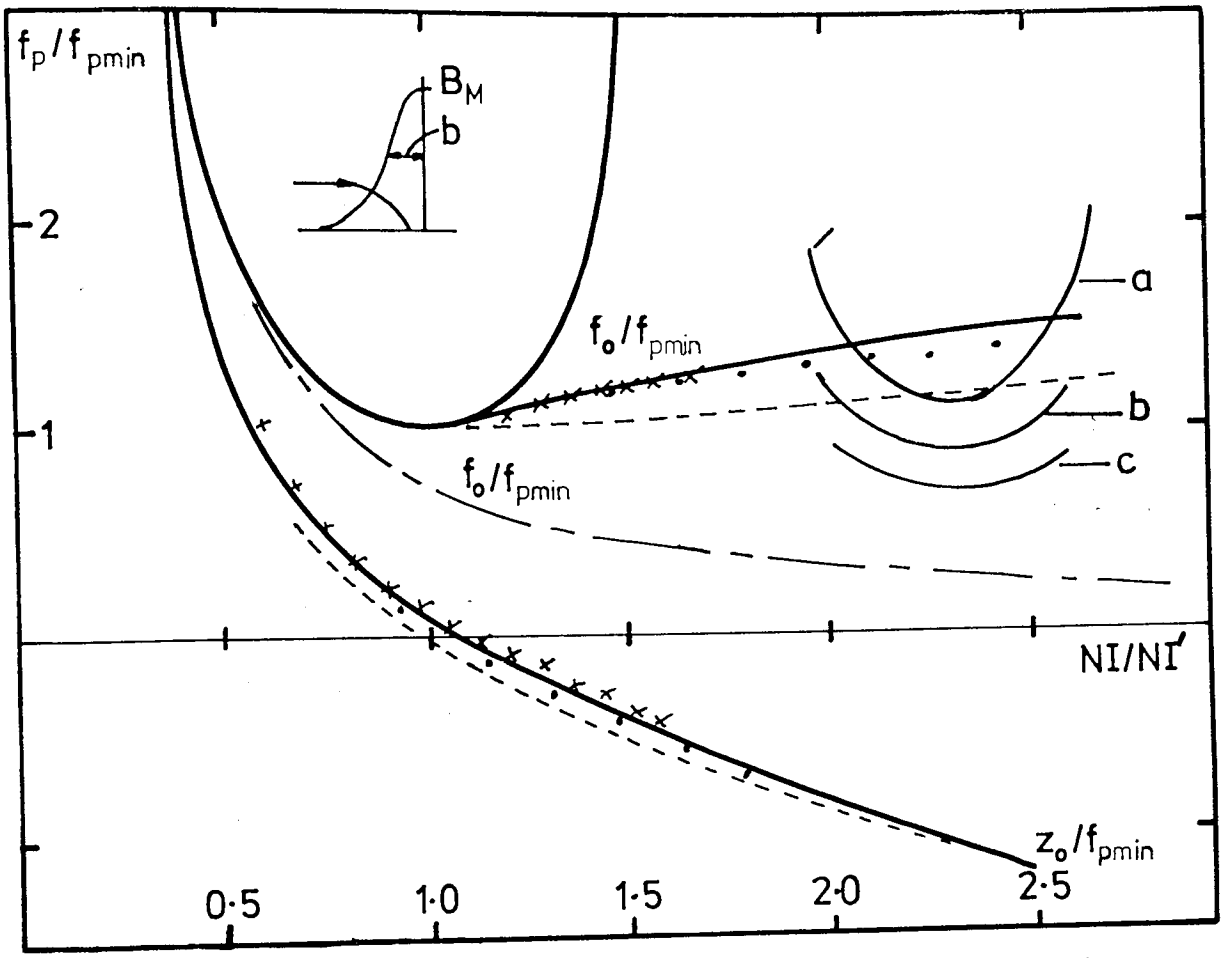

Figure 4.4 Normalised "half field" focal properties in terms of f_{pmin} and NI'

a - second projector focal length of snorkel lens IV

b - second projector focal length of half the flux density distribution produced by an iron-free pancake lens with outer to inner diameter ratio $D_2/D_1 = 3$.

c - second projector focal length of half the flux density distribution produced by an iron-free pancake lens with outer to inner diameter ratio $D_2/D_1 = 199$.

——— focal properties of half the flux density distribution produced by an iron free lens with outer to inner diameter ratio $D_2/D_1 = 19$.

- - - - - - - - focal properties of half the flux density distribution produced by an iron free lens with outer to inner diameter ratio $D_2/D_1 = 3$.

× × × × × focal properties of snorkel lens IV calculated by FLUTRAG.

• • • • • focal properties of snorkel lens IV calculated by Munro using the finite-element method.

——— - ——— Objective focal properties of snorkel lens IV for a trajectory entering the rear of the lens, i.e. in the opposite direction to the × × × × curve, calculated by FLUTRAG.

5. COMPUTER PROGRAMS

5.1 Computational techniques used in electron optics

With the aid of the computer it is possible to speed up many of the time-consuming and monotonous calculations in electron optics. The computer also makes it possible to explore new ideas and systems without the need for expensive laboratory investigation. The relaxation method used to determine an electric or magnetic field distribution lends itself directly to computerisation (Liebmann 1949). Present computers with stores of many thousands of words are now capable of handling large numerical problems with ease. Among these may be mentioned the "finite-element" methods (Munro 1971) of solving electric and magnetic potential field problems.

The present study was mainly concerned with producing new types of lenses and workable electron optical systems, hence there was little need for high accuracy in the initial calculations of lens and system properties. The time taken to "debug" a computer program and to put it into a suitable form for presenting the results logically increases considerably with program sophistication. The computational methods employed in this project were therefore the simplest consistent with an accuracy of the same order as that of the experimental results.

Two programs were developed "FLUXBZ" and "FLUTRAG"

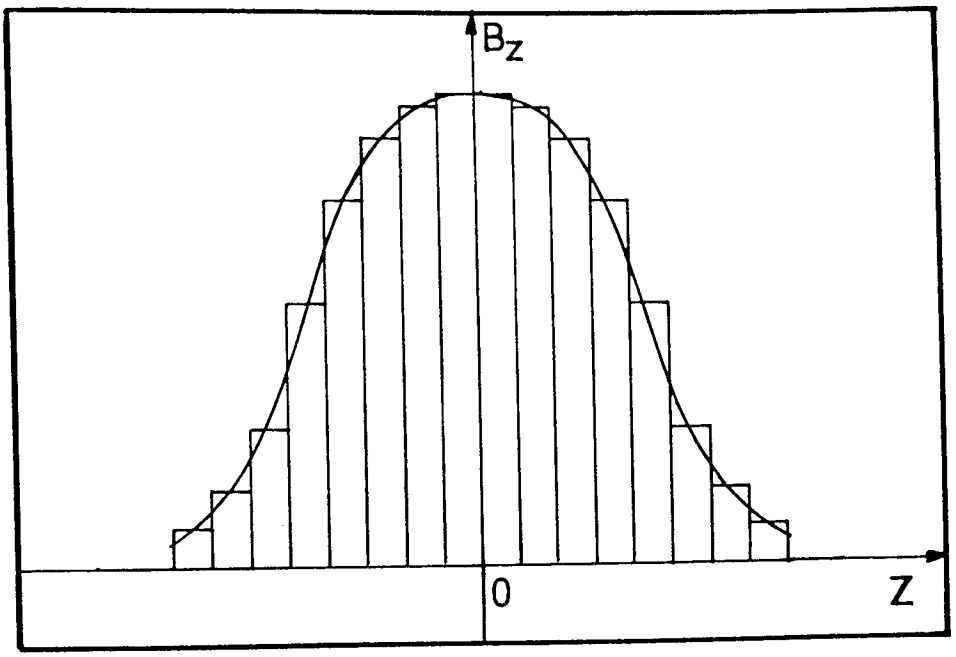

Figure 5.1 Staircase conversion of a flux density distribution as an input to "FLUTRAG".

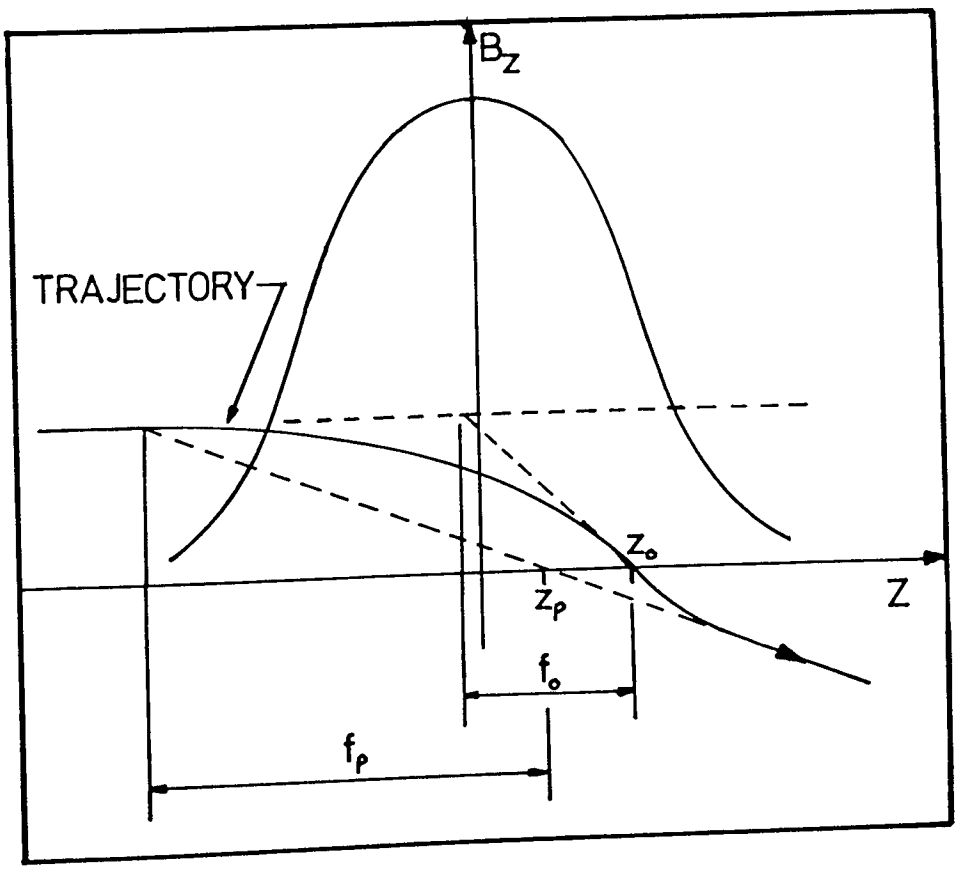

Figure 5.2 Cardinal points of a lens as calculated by "FLUTRAG".

these were used to calculate the axial flux density distributions and focal properties of the lens systems described in Chapter 4. Listings of both programs are included in Appendix 5, together with a sample of the graphical output they produce.

"FLUXBZ" calculates the axial flux density distribution produced by an iron-free coil from the exact expression given in Appendix 4. Since the field distribution of this system is very similar in shape to that produced by "pancake" and "single pole" lenses, this greatly simplifies the calculation of the focal properties of these lenses, as previously described in Chapter 4.

The program "FLUTRAG" calculates the trajectory of an electron passing through the lens. The input to this program can be either an experimentally measured field distribution or a distribution calculated by "FLUXBZ", together with the initial conditions of an electron on entering the lens field. "FLUTRAG" replaces the input field distribution by a "staircase field", as shown in Figure 5.1. The program proceeds to calculate the trajectory of the electron through the lens by solving the trajectory equations in each step of the staircase. The flux density B_z is thus assumed to be constant over each step. The corresponding ray height r and slope r' are given by:- (see equation 4.2.9 page 61),

$$r = r_{in}.\cos K(z + z_{in}) + (r'_{in}/K).\sin K(z + z_{in}) \quad \ldots\ldots\ldots 5.2.1$$

$$r' = r'_{in}.\cos K(z + z_{in}) - K.r_{in}.\sin K(z + z_{in})$$

.....5.2.2

Equations 5.2.1 and 5.2.2 are solved for each of the steps in the staircase field r_{in}, r'_{in} and z_{in} being the initial values and r, r' and z being the values on exit of one step and the initial conditions on entry into the next step. This progam produces all the primary focal properties and lens parameters (Figure 5.2) but not the aberrations. The operation of "FLUXBZ" and "FLUTRAG" is shown in the form of a flow chart, Figure 5.3.

Extensive use was made of the graph plotting facility on the computer and it is possible to display several trajectories through the same lens, or several flux density distributions on one graph. To give an indication of the accuracy of this method of calculation the Glaser bell-shaped lens was used as input to "FLUTRAG". The focal properties calculated by "FLUTRAG" were compared with the focal properties calculated from the analytical expressions and found to agree to better than 10%. This was considered adequate for calculating focal properties to be compared with the experimental results as described in Chapter 4.

Note In practice, accuracy will be better than this since it is difficult to get good agreement with a bell-shaped field as this field extends to infinity. In a practical comparison it is therefore necessary to terminate the bell-shaped field arbitarily, and this results in loss of accuracy in the comparison.

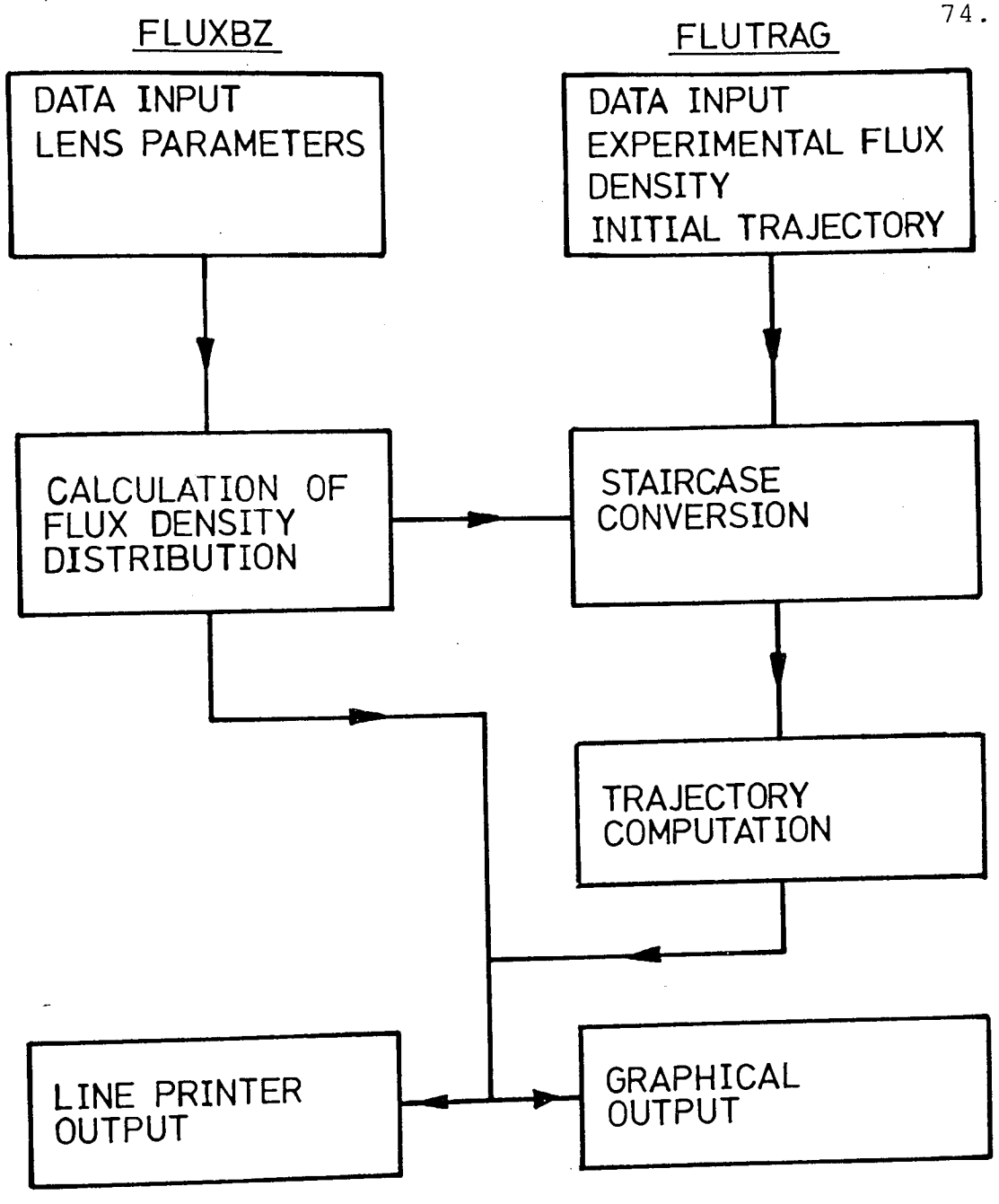

Figure 5.3. Flow chart of "FLUXBZ" and "FLUTRAG".

5.2 Programs from external sources

As the project progressed, the electron optics became more complicated and although the simple computer programs described in 5.1 were adequate for calculating the focal properties, methods were required for determining the field distribution of the new magnetic circuits. By good fortune two new methods appeared during this phase. One was the finite-element method devised by E. Munro (1971) at the Engineering Laboratories, Cambridge University. The other was the direct or integral method of Newman et al (1972) developed at the Rutherford Laboratory at Harwell.

The finite-element method introduced by Munro for calculating the magnetic flux density in all parts of a magnetic lens and in particular, along the lens axis, has enabled the detailed design of magnetic electron lenses to be carried out in a way that was not previously possible. In this method a system of triangular meshes is superimposed on the cross-section of the lens and the space around it. The mesh must extend to a boundary of known potential or in some cases to infinity; the average magnetic vector potential in each "finite-element" of the mesh is determined by solving the associated "finite-element" equations, based on the partial difference equation for the magnetic potential, with the aid of a digital computer. In this method it is straightforward to calculate saturation effects in the iron. Once the magnetic potential along the axis is known, the lens properties can

be readily calculated. A minor disadvantage of the finite-element method is that it is necessary to determine the magnetic field everywhere within the given boundary, even if this includes regions of no direct interest to the designer. Moreover, in non-conventional lenses such as single-polepiece lenses (Mulvey 1974), it is sometimes difficult to decide where the boundary should be set to obtain maximum accuracy for a given computing time. These difficulties can be avoided by first calculating the magnetic field due to the current carrying conductors alone and then the subsequent magnetisation of the iron circuit (Newman et al 1972). The magnetic field at any point is then simply the sum of these two fields. The computational time is comparable with that of the finite-element method but it is only necessary to know the boundaries of the current carrying elements and those of the iron circuit. By the use of these powerful complementary methods it is possible to investigate the properties of new types of lenses.

Figure 5.4 shows the graphical output from the finite-element method kindly supplied by Dr. E. Munro. The flux density along the axis is printed out separately and shown superimposed on the figure. The experimentally measured distribution (see Chapter 7,section 4) was scaled up to 8000 A-t and found to be in good agreement with the calculated distribution at this excitation.

The program of Newman et al was used in the evaluation of the million volt lens and a sample of the

output from that program can be found in Chapter 10.

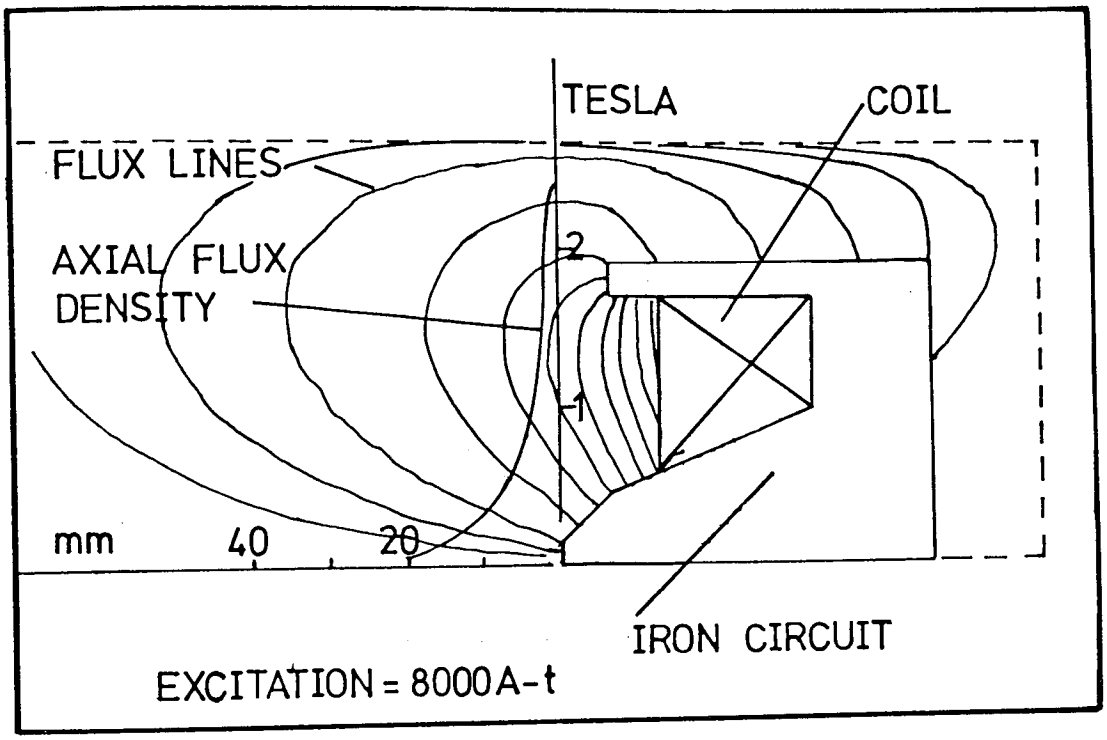

Figure 5.4 The magnetic circuit of snorkel lens IV showing the magnetic flux lines and the axial flux density distribution for an excitation of 8000 A-t. The dashed boundary is the boundary condition of the program where the magnetic vector potential is defined as zero. The left hand boundary is further displaced than the top and right hand boundary to achieve maximum accuracy in the vicinity of the lens snout and is not shown on the figure.

6. PRODUCTION OF THE MINIATURE MAGNETIC ELECTRON LENSES

These lenses were constructed from 'O' quality iron (Edgar Allen, low carbon content) to normal workshop tolerances in the Physics departmental worksop.

6.1 Miniature projector/pancake lens

In order to test out the miniaturisation techniques a 30 kV projector lens was designed with an outside diameter of 50 mm and an axial depth of 16 mm as shown in Figure 6.1. Its practical realisation is shown in Figures 6.3, 6.4 and 6.5.

The winding consisted of a single coil with 120 turns of 24 swg enamelled wire. An excitation of 2000 Ampere-turns was obtained with a current of 16.7 amps. The lens was tested on the "Intercol" electron optical bench. With a 10 kV electron beam a minimum projector focal length of 1.8 mm was achieved with an excitation of 1300 Ampere-turns. Figure 6.2 shows the experimentally measured relationship between projector focal length f_p and $NI/V_R^{\frac{1}{2}}$, see page 134. This lens is capable of focussing 30kV electrons, since 2000 A-t excitation is just sufficient to allow the lens to work at its minimum projector focal length (Mulvey and Newman 1972).

An advantage of the construction shown in Figure 6.1 is that it lends itself to easy conversion to a practical pancake lens. By removing the iron face plate and substituting a similar face plate made of brass, the

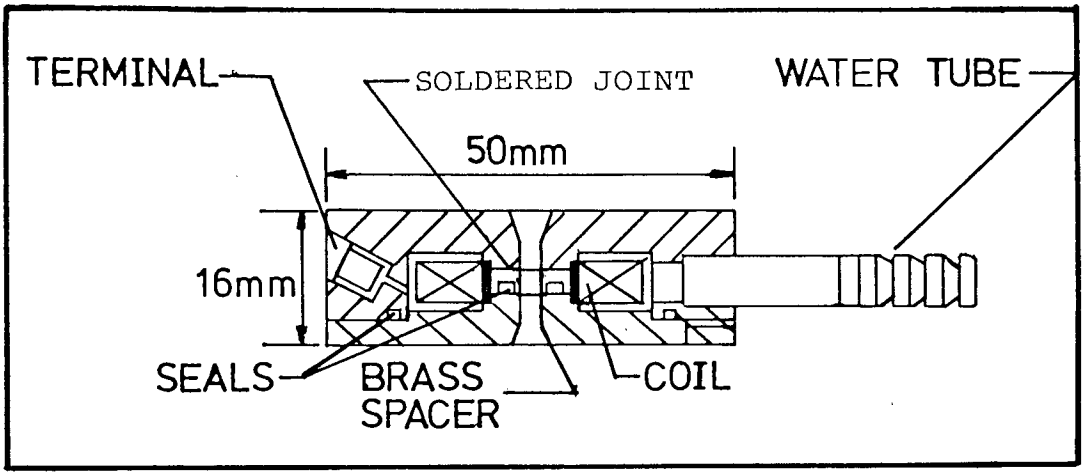

Figure.6.1. Early miniature 30 kV projector lens (Full size). Excitation 2000 A-t, No of turns = 120. The inner seal is both a vacum and water seal.

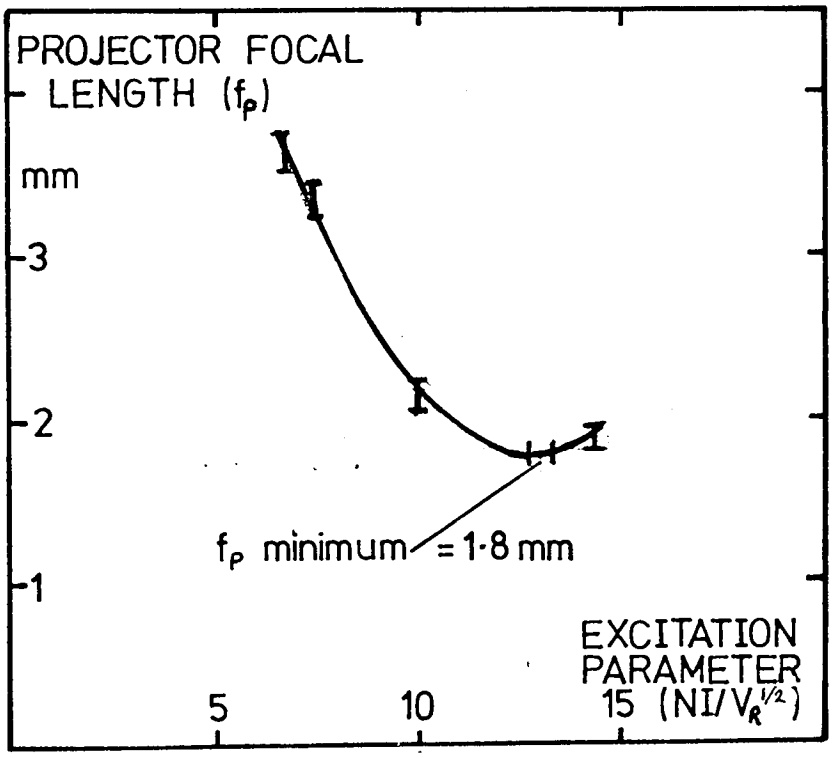

Figure 6.2. Experimentally measured projector focal properties of the 2000 A-t miniature projector lens.

Figure 6.3 Assembled 2000 A-t projector lens. The nylon terminals provide water tight seals for the coil leads. Length of matchbox is 50 mm.

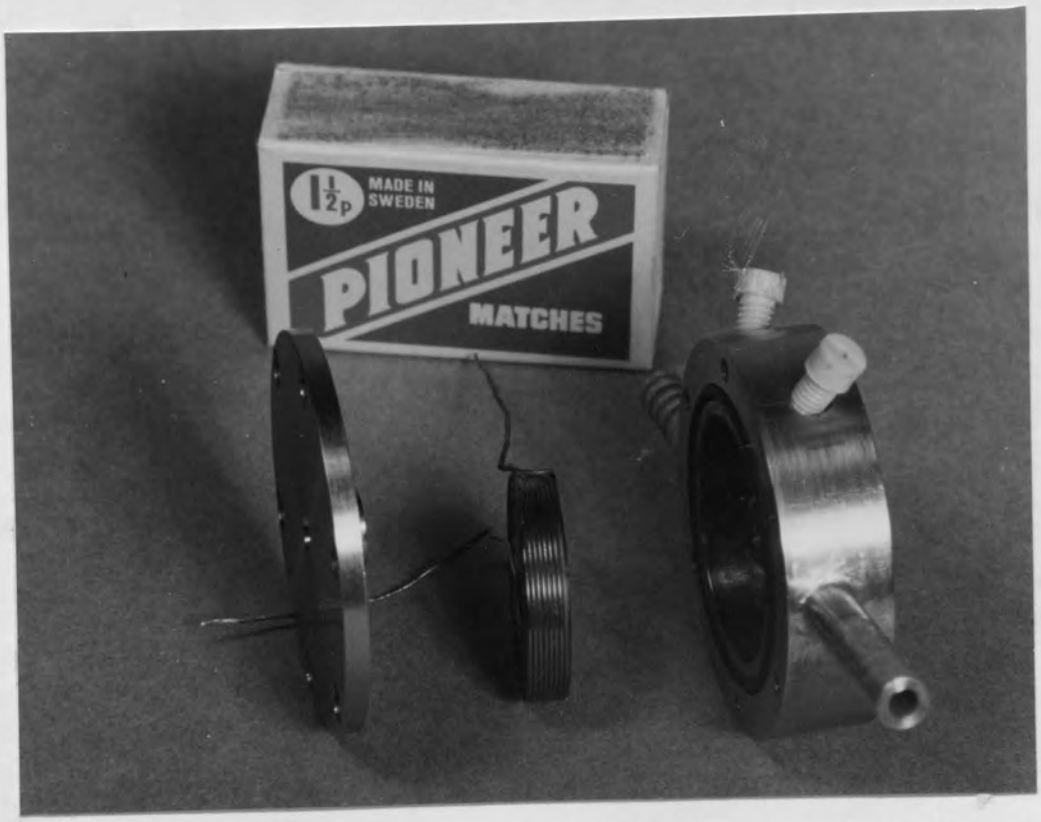

Figure 6.4 Exploded view of the 2000 A-t projector lens showing the enamelled copper wire coil in the lens.

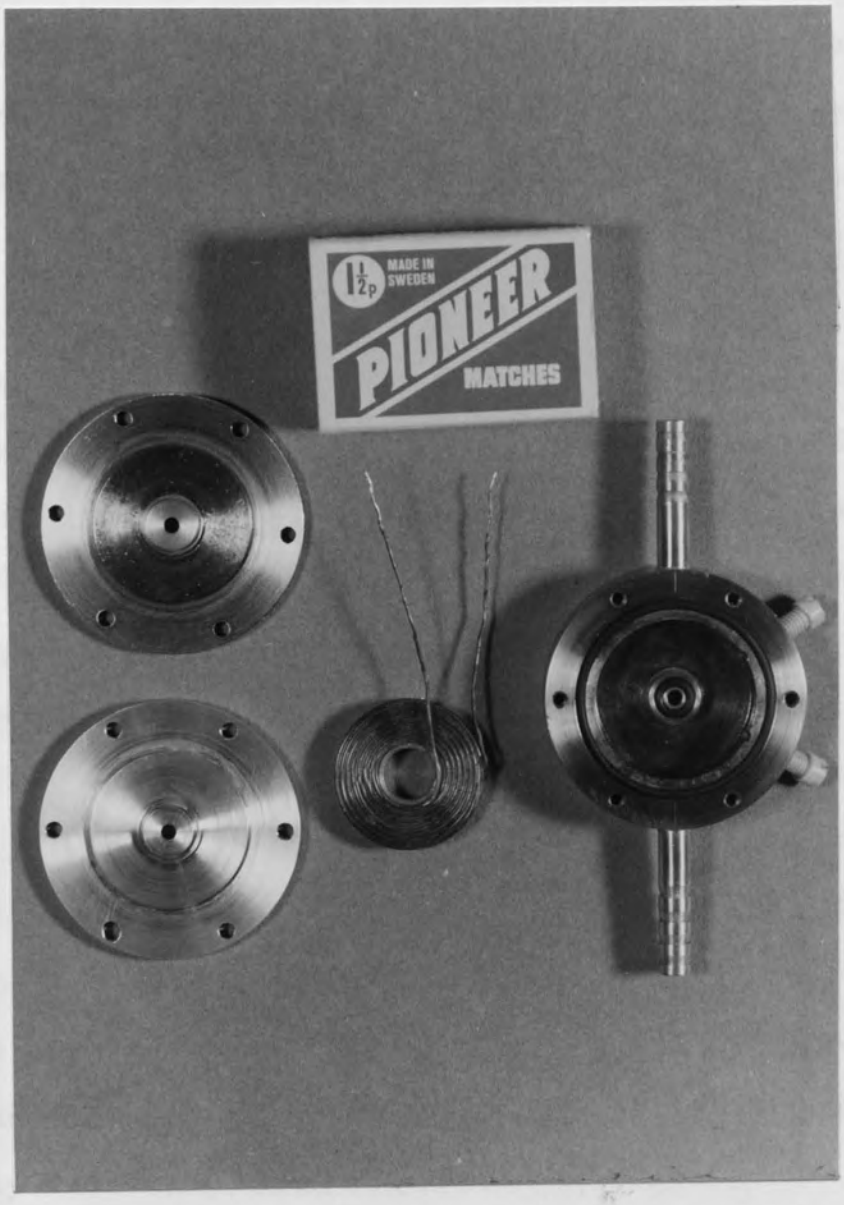

Figure 6.5 The 2000 A-t miniature projector lens with the brass top plate, which coverts the projector lens into a miniature iron shrouded pancake lens. The iron top plate and the wire coil are also shown.

axial field distribution is broadened into that of a 'pancake-type' lens. A blind hole was drilled into the brass plate to allow the Hall probe to be inserted and the axial flux density distribution to be measured. The result is shown in Figure 6.6a since $\int B_z dz = \mu_o NI$ the area under the B_z - z curve must correspond to the excitation applied. This fact enables the inaccessible part of the axial flux density distribution for the pancake lens to be estimated with fair accuracy. The projector focal length against excitation parameter for the complete axial flux density distribution from the pancake lens was calculated using "FLUTRAG" and subsequently measured on the Intercol Electron Optical Bench. The calculated minimum projector focal length was 5.1 mm and the measured value was 4.9 mm, see Figure 6.6b. In view of the various assumptions made and the experimental errors involved the agreement between the measured and calculated values is satisfactory. The important point that this experiment established is that it is possible to achieve a focal length of about 5 mm with a lens opening of some 40 mm, i.e. the lens operates essentially with only one polepiece.

6.2 A 100 KV Magnetic Electron Lens for the E.M.6 Microscope

With the successful operation of the previous lens a more powerful version was designed capable of operating at 100 kV. This lens was designed to replace the projector lens in the E.M.6 microscope, which has an excitation of 4000 Amp-turns at 100 kV. In order not to

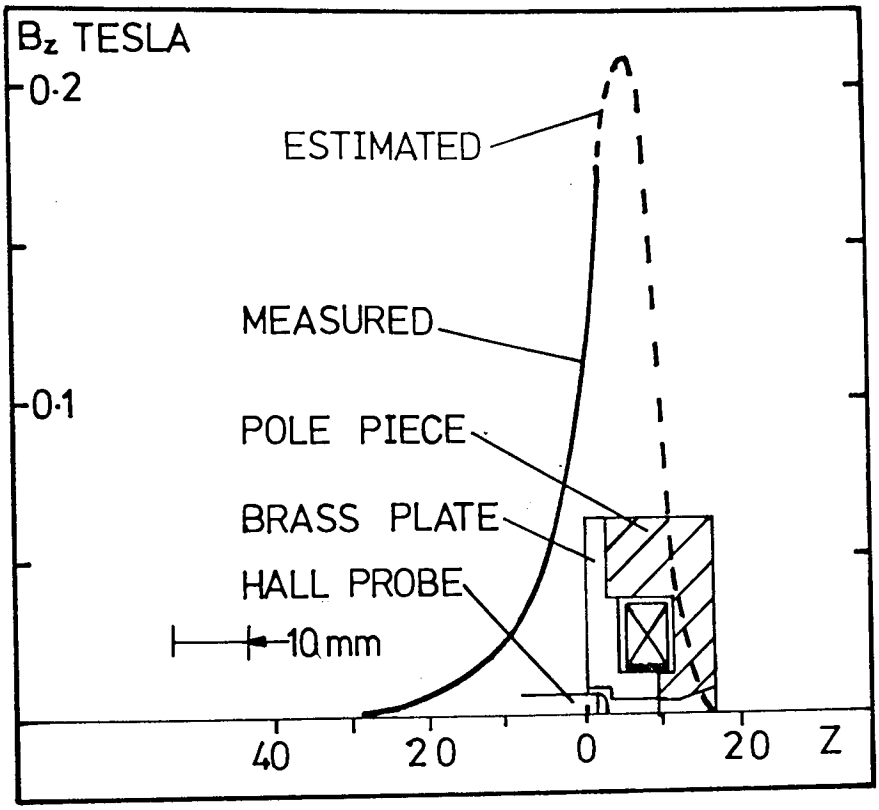

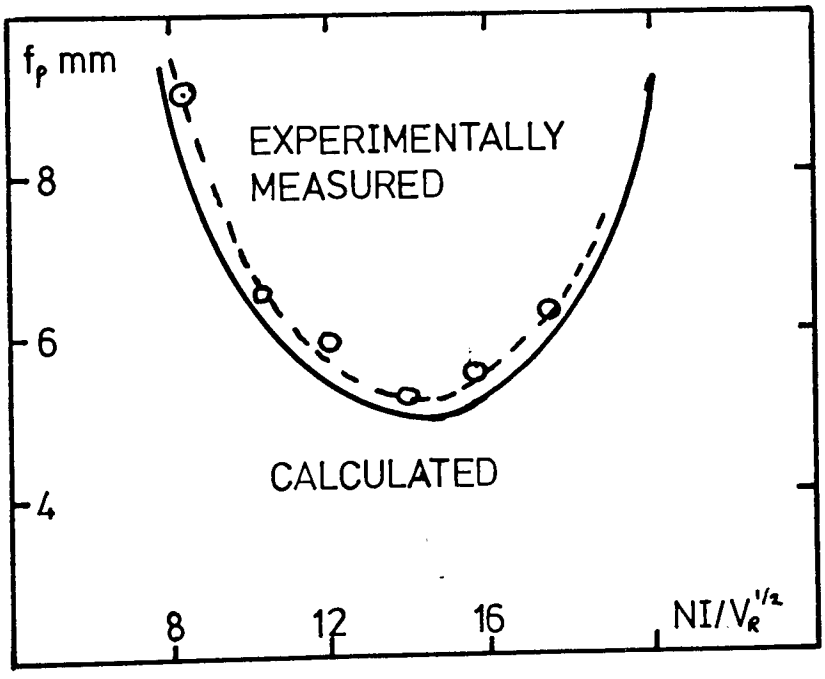

Figure 6.6. a) The axial flux density distribution of the miniature pancake lens as measured by the Hall probe (solid line) and the estimated portion (dashed line).

b) The projector focal properties of the miniature pancake lens as calculated by "FLUTRAG" (solid line) and as experimentally measured (dashed line).

disturb the normal operation of the microscope, the new lens was designed to fit into the diffraction specimen stage of the E.M.6, immediately below the normal second projector lens. This restricted the outside diameter of the lens to 46 mm, i.e. 4 mm smaller than the diameter of the previous lens. The construction and materials used in this lens are shown in figure 6.7. Coils similar to the one used in the previous projector lens were used to give the 4000 ampere-turns required. The wire connections of these coils were brought out through the water outlet pipes and into a junction box to remove the need for separate terminal studs, thereby simplifying the construction.

The lens was first tested at an accelerating voltage of 10 kV on the Intercol Electron Optical Bench. Figure 6.8 shows the measured projector focal length plotted against lens excitation parameter $NI/V_R^{\frac{1}{2}}$; two successive minima of projector focal lengths may be seen. The lens was then inserted into the E.M.6 electron microscope for testing at 100 kV. The lens was mounted in the diffraction stage immediately below the final projector lens. With the miniature lens switched off an image of a specimen was obtained on the viewing screen using the lenses of the E.M.6. The second projector lens of the E.M.6 was then switched off and the miniature projector lens switched on. No essential difference could be detected between the images produced by the conventional and miniature lenses. This is not surprising since the polepiece bore and gap and the excitation were the same in

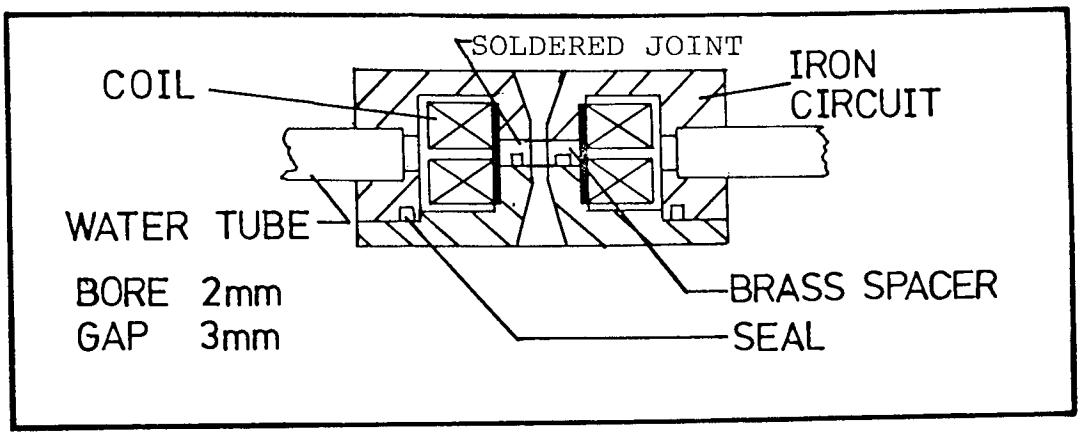

Figure 6.7. The miniature 100 kV projector lens. Two coils of 120 t produced 4000 A-t excitation. (Full size).

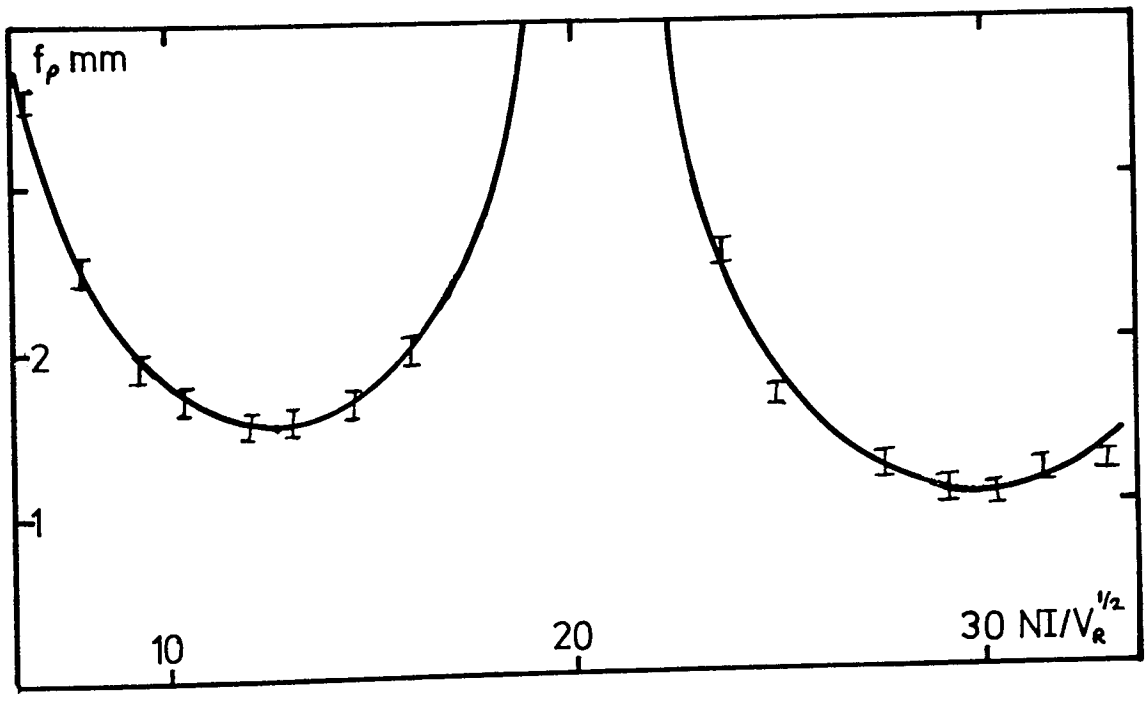

Figure 6.8. First and second projector focal properties of the 100 kV miniature projector lens, measured experimentally.

Figure 6.9 The 100 kV miniature projector lens designed to replace the EM6 projector lens on top of an EM6 double condensor lens. The outside diameter of the miniature lens is 50 mm.

both cases. The only difference was the considerable difference in size of the two lenses.

Figure 6.9 shows the miniature 100 kV lens dismantled and supported by an E.M.6. double condenser lens, and Figure 6.10 shows a micrograph obtained from the E.M.6. microscope using this miniature lens.

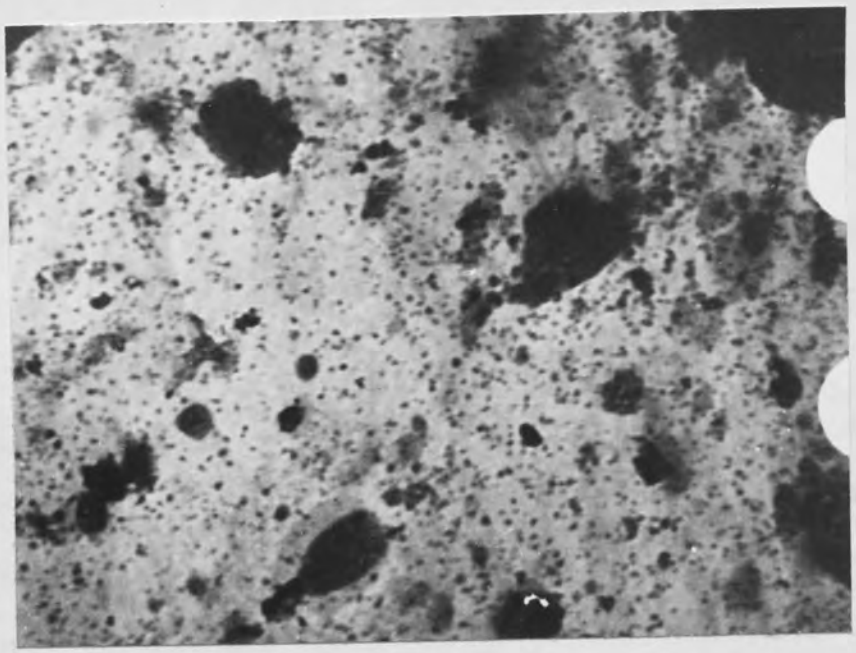

Figure 6.10 Micrograph of ink particles on a carbon film taken in the EM6 100 kV electron microscope using the 100 kV mini-projector lens in place of the normal EM6 final projector lens.
Electron optical magnification = 8500 X
Total magnification = 12 700 X

7 RADIAL FIELD (SINGLE-POLE) LENSES

7.1 The effect of an iron cylinder on the flux density distribution produced by an air-cored coil.

It is well known that the axial magnetic field distribution from a symmetrical coil is not altered if half the coil to one side of the plane of symmetry is removed and replaced by a large iron sheet of high permeability. What is not so well known is what happens to the axial field distribution when a long tube of high permeability is placed around such a coil. This effect has been investigated by Liebmann, using a resistance network (Liebmann 1950). Liebmann measured the magnetic vector potential against the radial distance from the axis for an infinitely long iron-free solenoid and for the same coil surrounded by a long iron tube of infinite permeability. Liebmann's result was that the magnetic field inside the coil was increased by 69%. This value was found to decrease by a negligible amount even when the permeability of the iron was reduced to 1000. The result is at first sight surprising since the flux density outside an infinitely long coil is zero and one might therefore expect an iron cylinder placed in this region to have a negligible effect on the flux density inside the coil.

No previously published information could be found on the effect of an external iron cylinder on the

flux density distribution on the axis of a short magnetic coil. It is important to know this in designing a practical lens system, since magnetic screening against external fields is essential. Moreover if an iron shroud can be introduced into a pancake lens without drastically affecting the electron optical properties, then conventional methods of construction and calculation can be applied. Furthermore, the judicious use of iron might allow one to control the field distribution of such lenses.

A series of experiments was therefore planned to investigate these effects. The apparatus is shown in Figure 7.1. Figure 7.1 also shows the axial flux distribution of the coil in iron-free space (full-line) as determined by a Hall probe, and the resulting axial flux density, shown by the crosses, when a close-fitting iron cylinder was placed around the coil. It will be seen that the axial field distribution was not changed appreciably. This experiment was carried out using a water cooled coil producing 1100 A-t. The experiment was repeated for a reversed current to remove any hysteresis effects in the iron. Dr. Munro very kindly calculated the field distribution for this arrangement of coil and iron circuit for us, and his results are shown in Figure 7.2, together with the result obtained from the program "FLUXBZ", for the air coil of similar dimensions.

Experimentally the peak height rose by 3.3%, but the half-width remained substantially the same within the

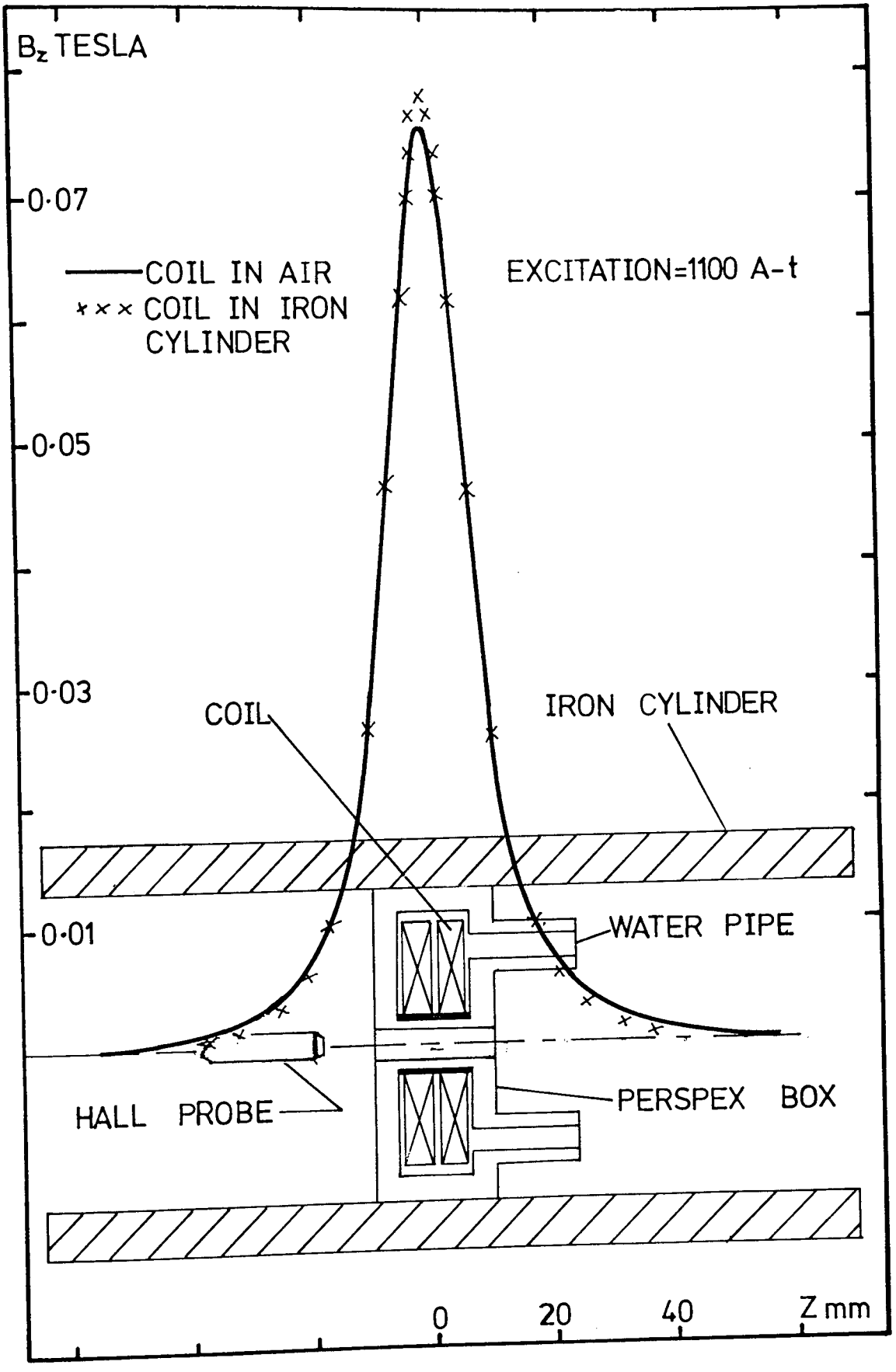

Figure 7.1 Apparatus for determining the effect of an iron shroud on the axial field distribution of a current carrying coil. Increase in peak flux density by iron shroud 3.3%.

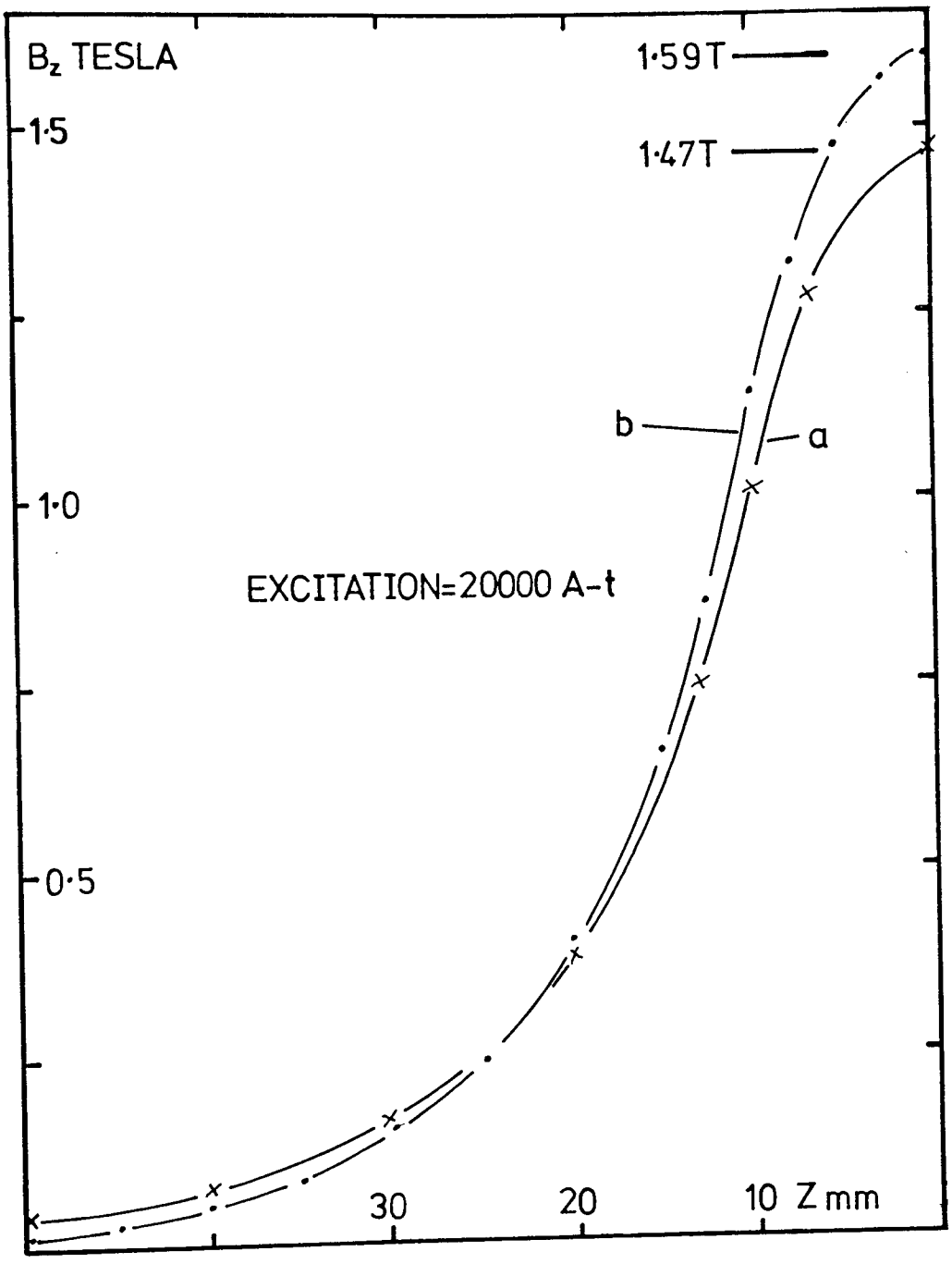

Figure 7.2 Influence of an iron shroud on the axial flux density distribution of a current carrying coil. a) calculated flux density distribution of an iron-free current carrying coil ("FLUXBZ"). b) calculated flux density distribution when a close fitting infinitely long iron cylinder is placed round the coil (finite-difference calculation). Increase in peak flux density due to iron 8.0%.

accuracy of the measurements (2%). The value calculated by Munro indicated an increase of 8% in peak height over the unshrouded coil with no change in half-widths. In this calculation Munro assumed a uniform high permeability of the iron and a limited number of mesh points in order to save computer time, and so the result could well be on the high side. It therefore appears that the field distribution of a shrouded pancake lens may be calculated to a sufficient degree of accuracy for the calculation of focal properties, by ignoring the effect of the iron shroud.

7.2 The effect of an Iron Plug on the flux density distribution produced by a current-carrying coil

To demonstrate what occurs to the axial flux density distribution when an iron plug is placed in the centre of a current-carrying coil, the apparatus shown in Figure 7.3 was constructed. It consisted of a perspex box carrying a water-cooled coil with a piece of soft iron on its axis. The flux density measured with the Hall probe is also shown in Figure 7.3. The solid line shows the flux density distribution through the coil with no iron present. The effect of the iron plug is indicated on top of this distribution. The peak flux density has to be estimated from the area under the curve as the Hall probe can only get to within 1 mm of the iron plug. Preliminary results indicate an increase of peak height of some 4-5 times that of the field due to the coil in the absence of iron. One point worth mentioning is that the tails of the flux density distribution are identical in

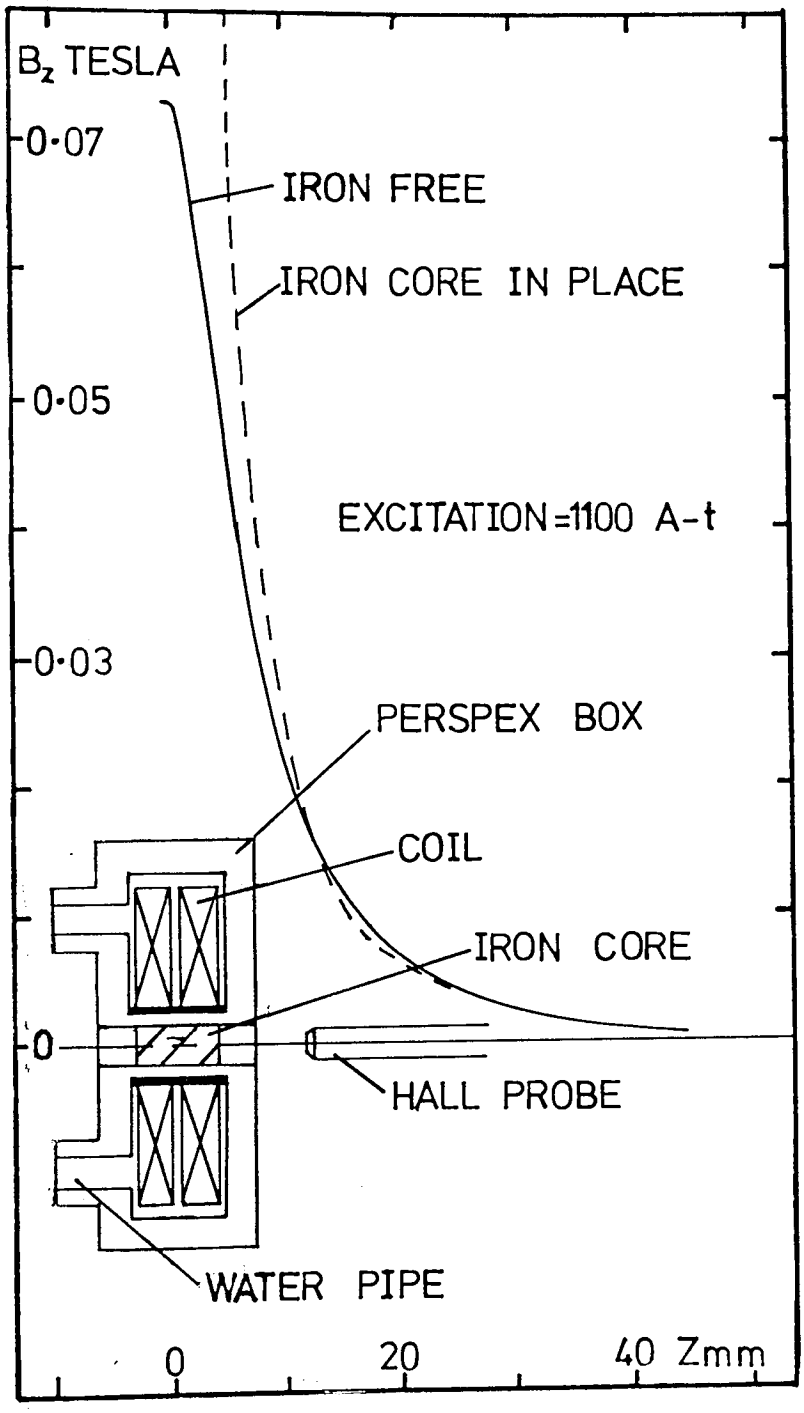

Figure 7.3 Effect on the axial flux density distribution of an iron-free current carrying coil when an iron plug is placed inside the coil.

both cases; the effect of the iron plug is only felt locally. So without losing a gentle "tail-off" of the field it is possible to produce high peak fields and narrow half-widths with only one polepiece.

7.3 The "radial-field" lens experiments

Figure 7.4 shows the apparatus used to develop the "radial-field" lens. A lens shell with a 10 mm iron plunger was arranged to pass through the centre of the coil. Ideally this should have had a plane face, but in practice it was found convenient to make a small depression in the end to allow access for the Hall probe.

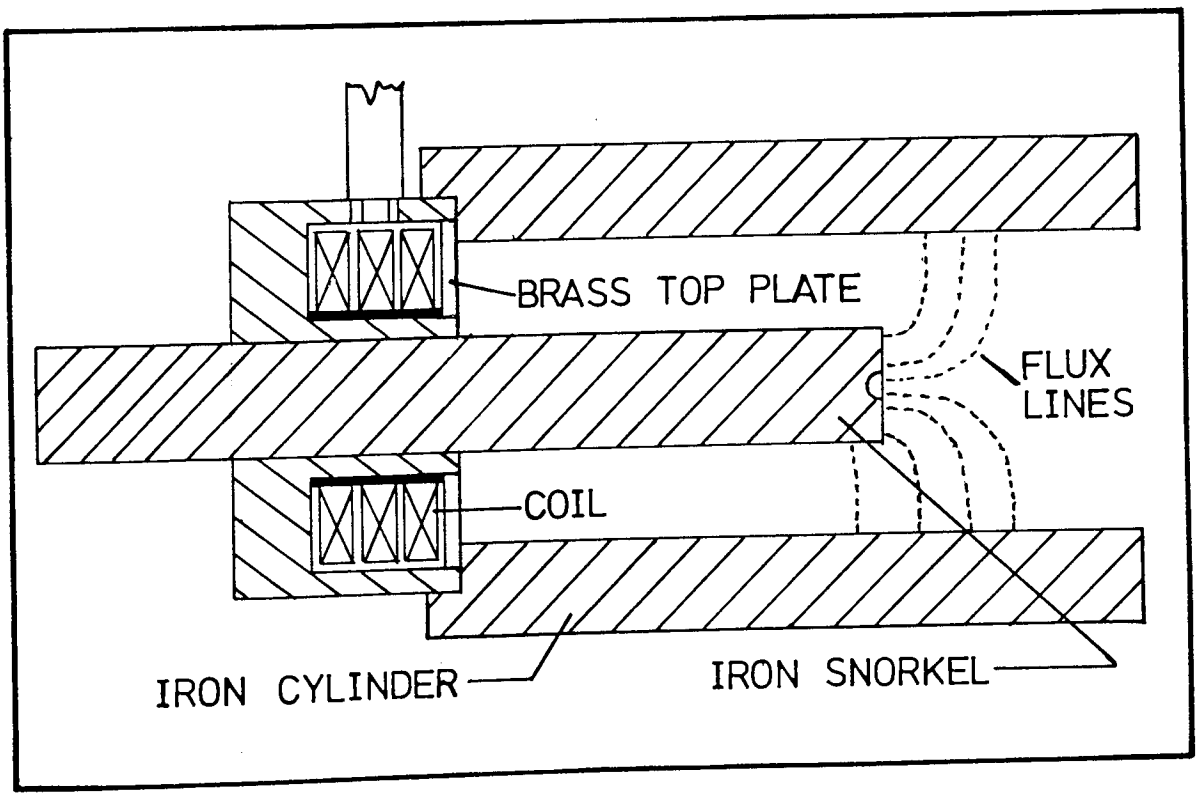

Figure 7.4 Apparatus for investigating "radial-field" lenses

The effect of the plunger is to act as a piston pushing the magnetic field distribution ahead of it. It is thus possible to design a lens system with the field distribution completely outside the structure producing it. A useful feature is that the lens housing can now be situated outside the vacuum system. The excitation available was 5000 A-t although in several cases it was not possible to make use of this amount, due to saturation of the iron. The highest excitation below saturation was used as this reduces the errors in measuring the flux density. For each position of the snorkel, the apparatus was checked for linearity and the flux densities were obtained on the linear portion of the curve for the various positions of the snorkel (Mulvey and Newman 1973).

The flux densities were obtained using a Hall probe. The precise axial position of the Hall probe element was determined by means of a coil with a reversed turn. The first series of experiments used a snout design with a recess to allow the Hall probe to enter the snout. The indentation allowed the element of the Hall probe to measure the peak and fall-off of the flux density distribution, so that the area under the flux density distribution could be measured. This enabled the calibration of the Hall probe to be checked independently.

A snout for a normal lens has a flat face so the distribution near the tip will be slightly different from the above experimental one. In both cases, however, the distribution 2 mm from the face should be very similar.

A snorkel with a flat face was introduced into the apparatus and a comparison of the flux density distributions obtained for various positions of the snorkel. These should give an indication of how the peak and half width of the distribution is affected by the position of the snorkel. This comparison is shown in

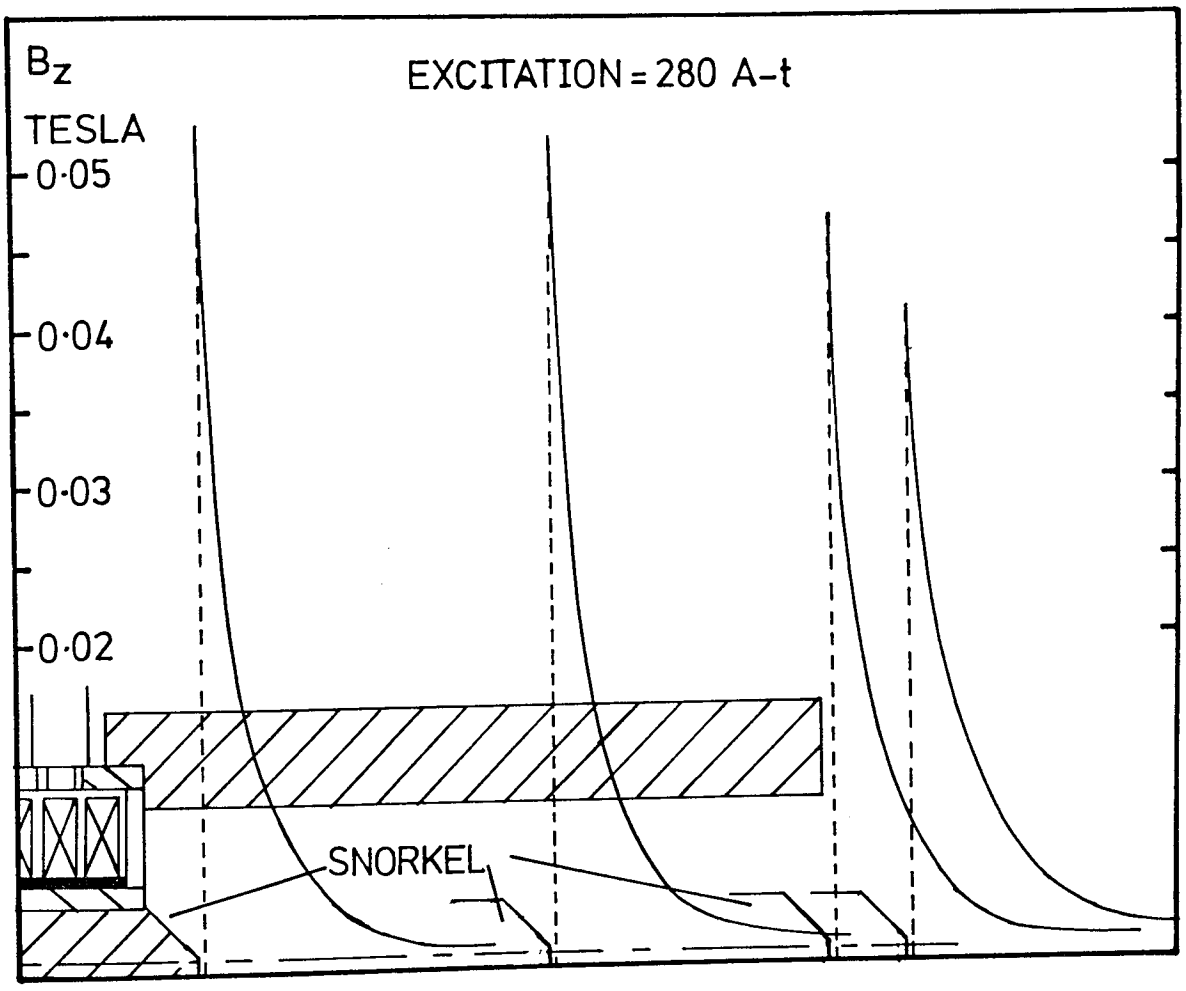

Figure 7.5 The effect on the flux density distribution as a flat-ended snorkel is pushed along the axis of a shrouded current carrying coil. The flux densities were measured with a Hall probe. Nearest approach of Hall probe element - 1 mm from pole-face

Figure 7.5. The iron snorkel inserted into the axial bore of the coil has the effect of concentrating the flux onto the axis, resulting in a high peak and small half width; the distribution also tails off rapidly. As the snout is pushed further along the axis the distribution is affected in the following way. Peak height falls and the distribution broadens due to leakage to the central pole-piece. This process can be seen by considering the direction of the magnetic flux lines in the various pole-piece geometries. For a snorkel standing proud of the structure the flux lines are shown in Figure 7.6a. In the first case a large amount of leakage occurs to the

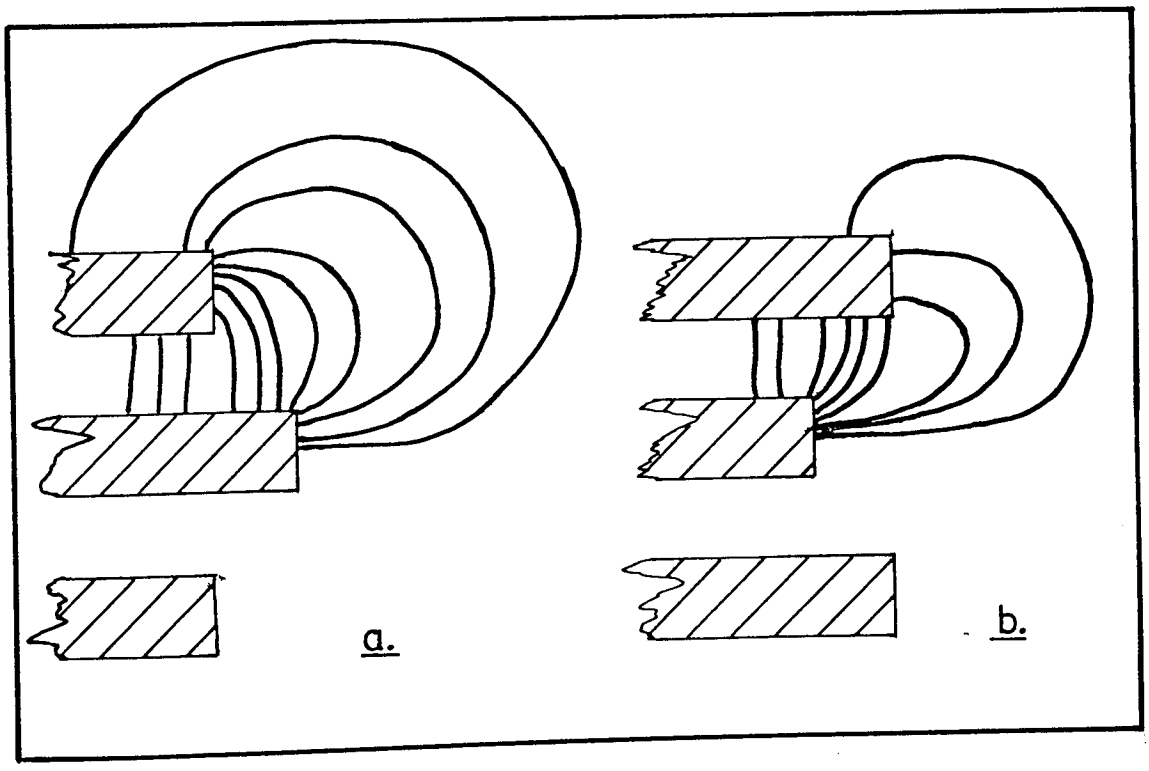

Figure 7.6 Magnetic flux lines for two pole-piece geometries in possible radial-field lenses
a - extended snorkel
b - retracted snorkel

extended snout causing a loss of flux collected at the snout tip, producing a smaller peak and a broader distribution. The second case collects the flux more efficiently and a high flux density is obtained in the region of the snout, Figure 7.6b. This system removes a certain amount of the advantage of the snorkel system i.e. being able to have the lens effect completely clear of the structure producing it - a distinct advantage when considering the placing of various detectors and in scanning electron microscopy. The position of the snout therefore depends on the use for which the lens is to be put. A projector or condenser system could have a retracted snout.

7.4 A practical snorkel lens

Figure 7.7 shows the first attempt to produce a practical "snorkel" lens. A miniature projector lens was modified as shown in the Figure. The lens was tested as a projector lens on the Intercol electron optical bench. However, the field of view on the screen was much smaller than was expected, and the beam appeared to be restricted. The lens was mounted on the Hall probe Bench and the axial flux density distribution determined. This revealed an unwanted air gap and saturation effects in the lens, as shown in Figure 7.7. Even at low excitation the unwanted stray flux on the axis was of the same order as the wanted distribution. This strong field in the lens bore produced a large focussing effect and the length of the lens bore acted as an aperture, reducing the field of view.

At maximum excitation the parasitic distribution was three times stronger than the snorkel distribution.

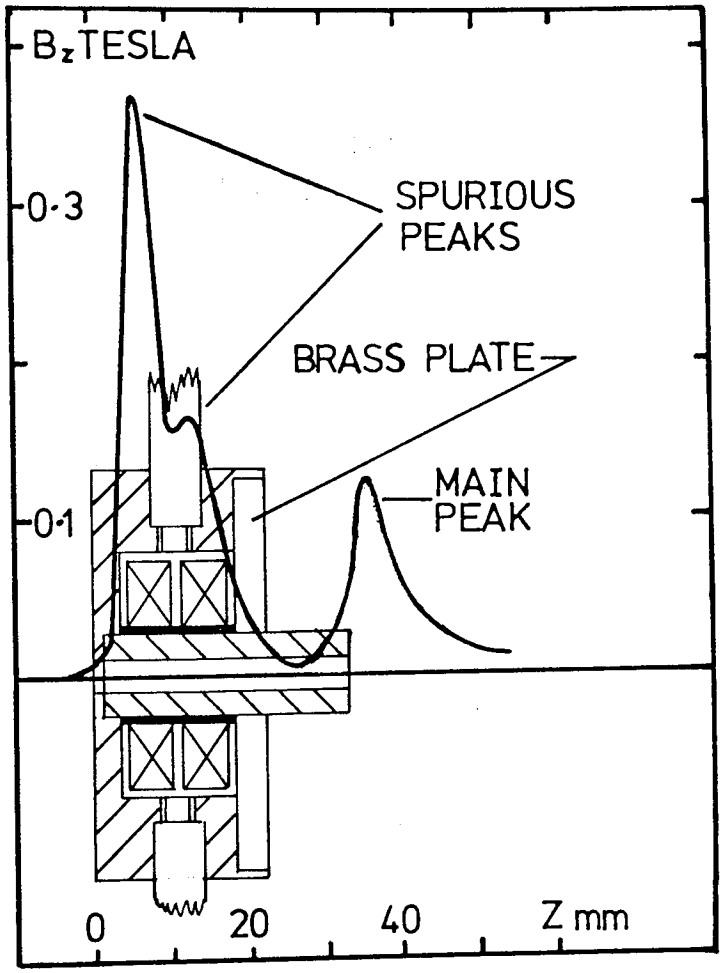

Figure 7.7 Snorkel lens I and its axial flux density distribution. Note the spurious peaks caused by iron saturation

The improved design shown in Figure 7.8a was then constructed. This lens was first tested for linearity on the Hall probe. A plot of flux density against current was taken, Figure 7.11. This lens was a great improvement on the first; the axial flux density remained linear with current up to 6 amps, but the iron circuit consumed about 30% of the total excitation at the

maximum permissible current of 16.8 amps. Flux measurements revealed that the flux density at the base on the cone forming the snorkel was approximately 0.8 TESLA at 6 amps; at the rear of the lens the flux density is probably about 1.5 TESLA and thus the non-linearity of the B/H curve becomes noticeable. This snorkel lens (mark II) was tested on the Intercol electron-optical bench and it was possible, even with such an inefficient design, to focus a 4 kV electron beam on a fluorescent screen placed 0.7 mm in front of the snorkel tip. Saturation was obviously occurring at the base of the snout and this was remedied in the mark III design, Figure 7.8b.

The performance of snorkel III was disappointing, although the field at the lens snout remained linear for an excitation of up to 1480 A-t the magnitude of the field was less than in the preceding design which became non-linear at 800 A-t, (Figure 7.11).

The iron circuit was subsequently redesigned, as in Figure 7.9 ; a smooth cone was used as the snout, the coil formers being specially shaped to sit on the cone. The excitation coils were designed to produce an excitation of 4000 A-t with an average temperature rise of 80^{o}C at the operating point. This was found to be achieved in practice, (Chapter 3, Section 4 and Figure 3.6). Figure 7.11 also shows the result of the magnetic test carried out on snorkel 4. The magnetic circuit is completely linear up to 17.5 amps, the maximum allowable current through the lens, Figure 7.10 shows a photograph

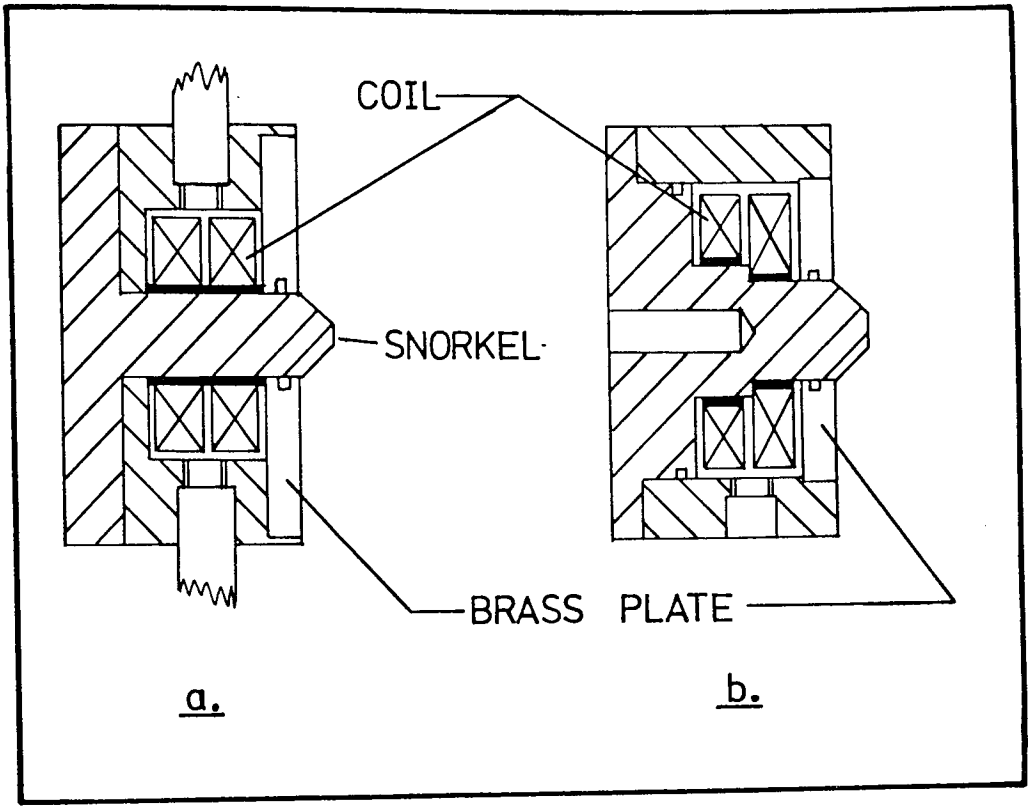

Figure 7.8 a) Snorkel lens II.
b) Snorkel lens III.

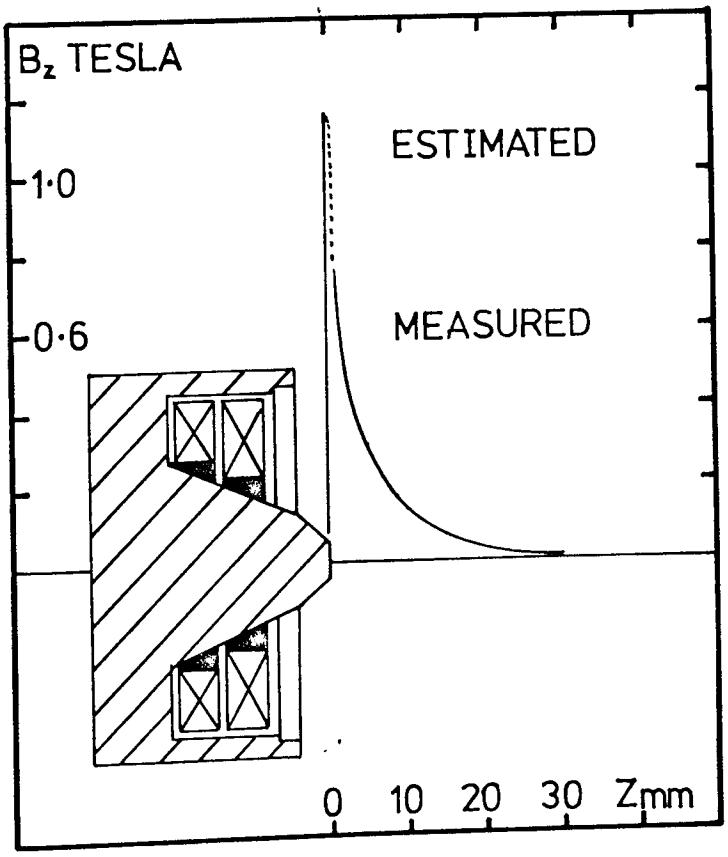

Figure 7.9 Snorkel lens IV and its axial flux density distribution

of the complete lens.

Measurements with the Hall probe allowed the flux to be determined at all points more than 1 mm away from the tip of the snout. Three search coils were placed on the snout, around the brass plate and at the base of the snorkel. The flux densities measured with this method indicated no problems with saturation effects at any position in the magnetic circuit. The fall-off of the flux density was determined using the Hall probe as shown in Figure 7.9. A large discrepancy was apparent between the measured flux density at the snout by the search coil method, and the approximate value obtained by the Hall probe. The Hall probe indicated a peak of 1.1 - 1.2 T, whereas the search coil gave a value of 0.7 TESLA. As the search coil in use was small and of so few turns (3) and also the scale to be read was small, it was decided to check the distribution by calculating the projector focal length using "FLUTRAG" to be compared with the focal length measured on the Intercol electron optical bench (Figure 7.12). The calculated value assuming a peak flux of 1.1 T gave f_p min = 4.9 mm and the measured value was 4.5 mm. The determination of the peak flux density at the snout of a miniature lens by the use of search coils appears to be difficult to carry out experimentally. A direct measurement in terms of focal properties may well be more accurate.

This lens was used for months in the laboratory and found to be very satisfactory. When it was

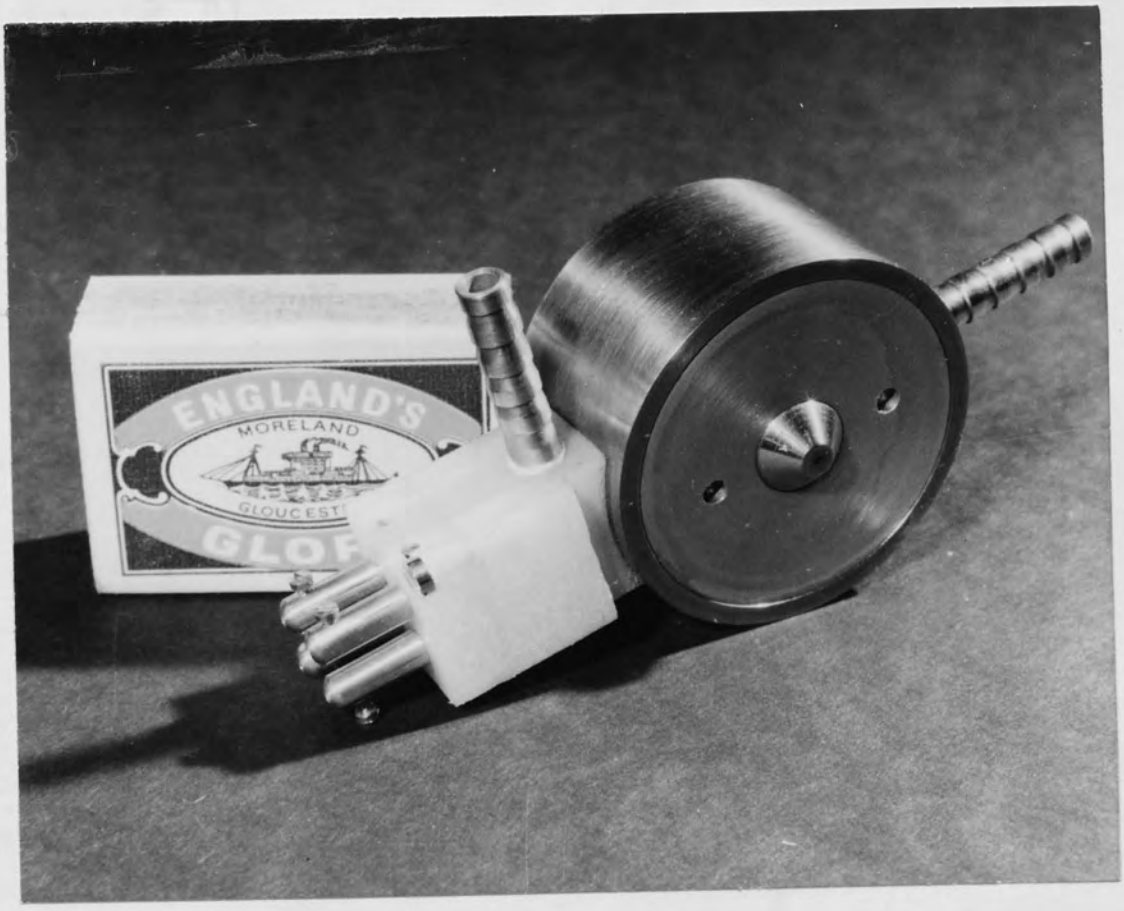

Figure 7.10 Snorkel lens IV showing the integral terminal block and the water connections.

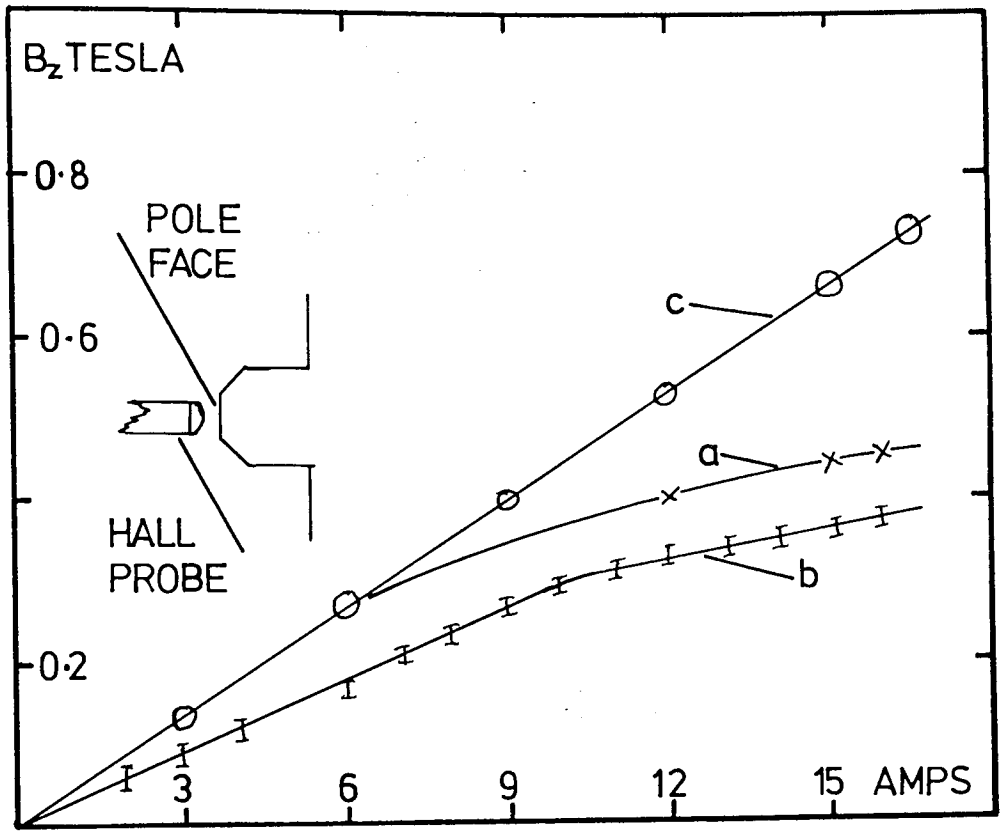

Figure 7.11 Comparison of the magnetic performance of the snorkel lenses.
a) snorkel lens II
b) snorkel lens III
c) snorkel lens IV

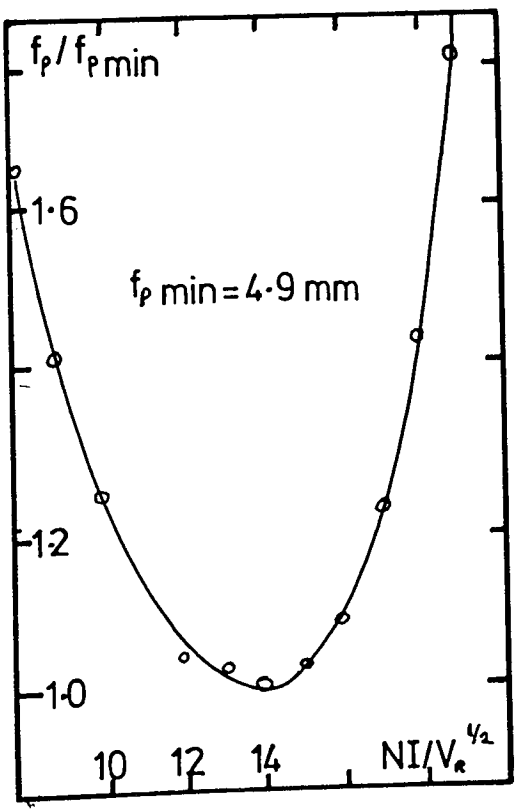

Figure 7.12 Projector focal properties of snorkel lens IV against excitation parameter.

dismantled in order to inspect the condition of the windings, it was evident that the inside case was beginning to rust slightly, and the coils appeared to be slightly charred. This slight charring was undoubtedly due to the fact that the lens was frequently used at excitations of some 4500 A-t, a 12% increase above the designed safe value. The lens was reassembled in this condition and continued to work satisfactorily with only a slight leakage current to the outside casing.

8 A MINIATURE TRANSMISSION ELECTRON MICROSCOPE

8.1 The basic electron optical system

When the successful operation of the miniature electron lenses had been established, a small transmission electron microscope was designed and constructed using miniaturised components to see how these would behave in practice. The microscope was built up on the Intercol electron-optical bench as shown in Figure 8.1 and Figure 9 in Appendix 2. The column was made by stacking lenses and spacers on top of each other. No alignments were provided except for gun tilt and shift. The electron beam travels upwards, first through the snorkel objective lens, then through the specimen mounted on the snout. The intermediate image formed by the snorkel lens field is further magnified by a miniature rotation-free projector lens before being rendered visible by the fluorescent screen (Mulvey and Newman 1973, Appendix 2). The observed magnification was consistent with that calculated from the electron-optical parameters. No alignment problems were encountered within the magnification limit of 10,000 X, obtainable by increasing the length of the iron spacer tube to 250 mm. This instrument was demonstrated at the National Physical Laboratory on June 26th 1973, using the N.P.L. Intercol apparatus as an electron source.

Mention should be made of the miniature rotation-free projector lens (Juma and Mulvey 1974) which has an

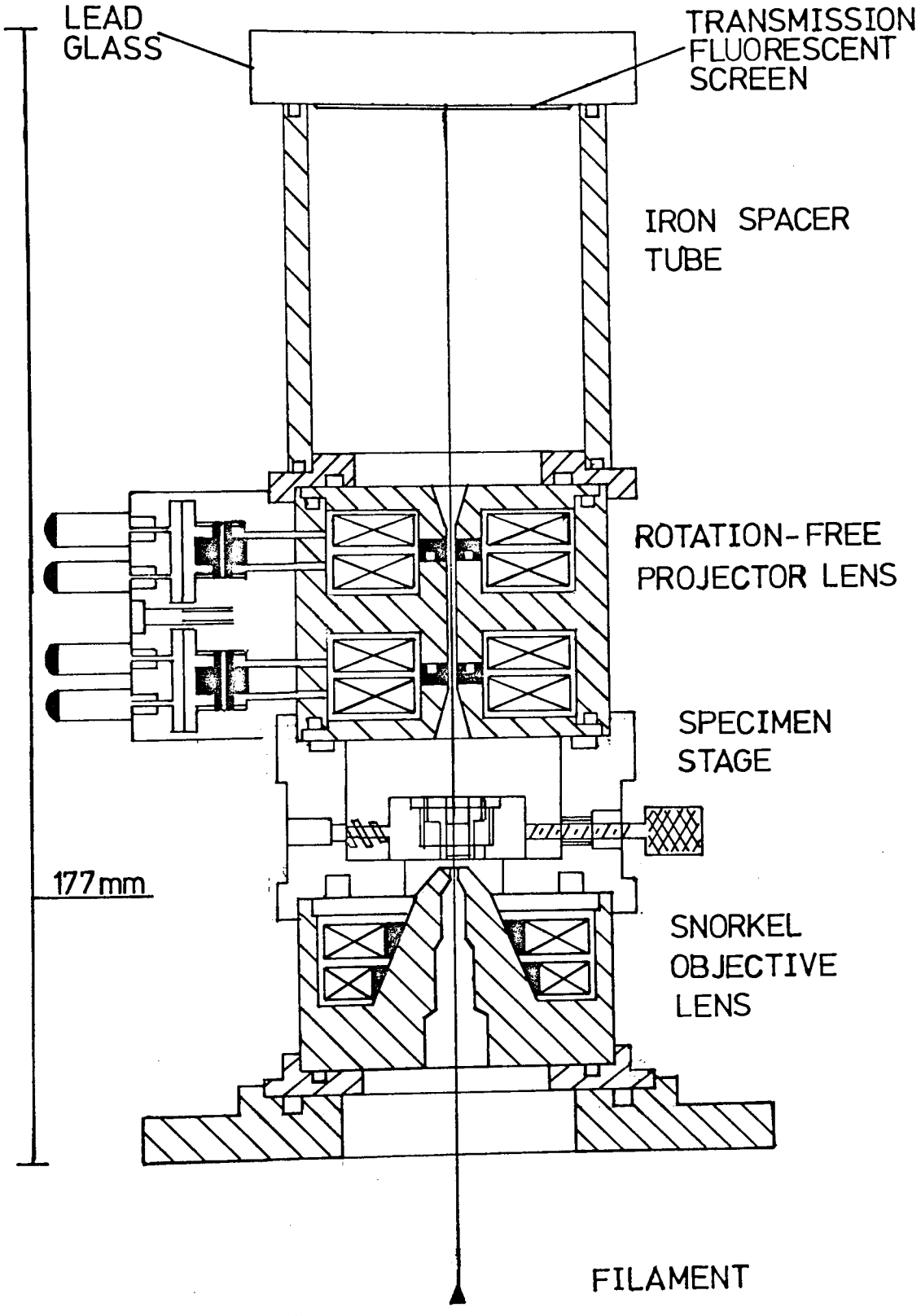

Figure 8.1 Miniature 100 kV Transmission Electron Microscope (Full size). Total magnification is 2500 times, being the product of the objective (7x), the first projector (9x) and the second projector (39x). A magnification of 10 000 times is possible with an iron spacer tube 250 mm long

effective focal length of only 0.17 mm, and consequently an unusually high magnification. Figure 1 in Appendix 2 shows a photograph of this lens. A rotation-free lens considerably improves the alignment tolerances since the troublesome rotational movement of the image is removed. The instrument can, of course, be used as a typical three-stage microscope by abandoning the rotation-free facility, but in this mode an alignment section would be desirable. Much useful experience was gained in constructing and using this instrument. Figure 8.2 shows a micrograph of latex spheres taken with a polaroid camera focussed on the transmission screen (Mulvey and Newman 1973). The latex spheres were 1.3 μm in diameter. In the absence of an internal camera, the resolution of the instrument, some 5 nm (50 A.U) was in fact set by the resolution of the fluorescent screen (≃ 50 μm) and the maximum magnification (10,000 X) provided. The theorectical resolution limit of the objective lens (0.2 nm at 100 kV) could therefore not be determined experimentally.

Figures 8.3 (a) and (b) show micrographs of a carbon film supported by a copper grid. The magnifications in each case are 3200 X total (1600 X electron optical) and 5600 X total (2800 X electron optical) respectively.

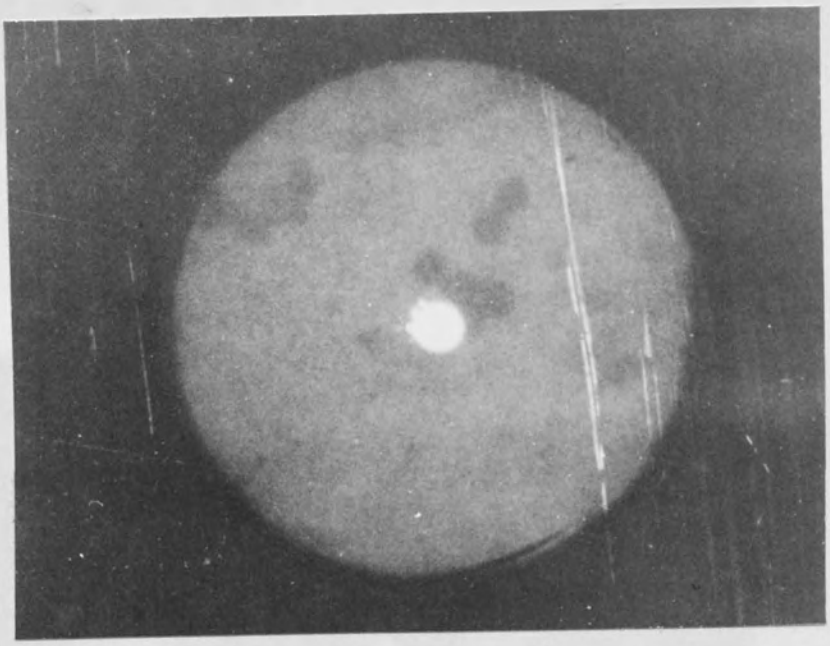

Figure 8.2 Micrograph showing latex spheres 1.3 μm in diameter taken using the miniature transmission electron microscope shown in Figure 8.1. Electron optical magnification 2000 X, total magnification 3600 X.

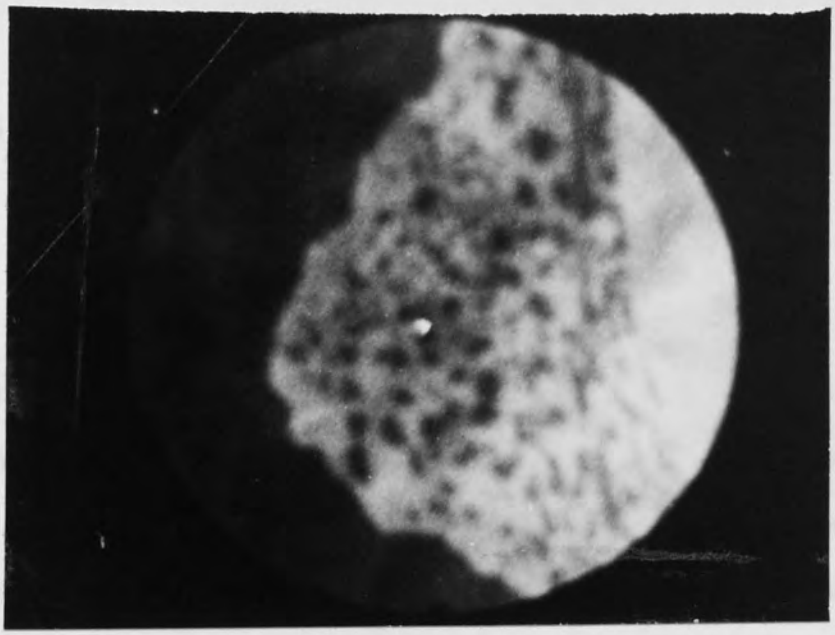

(a)

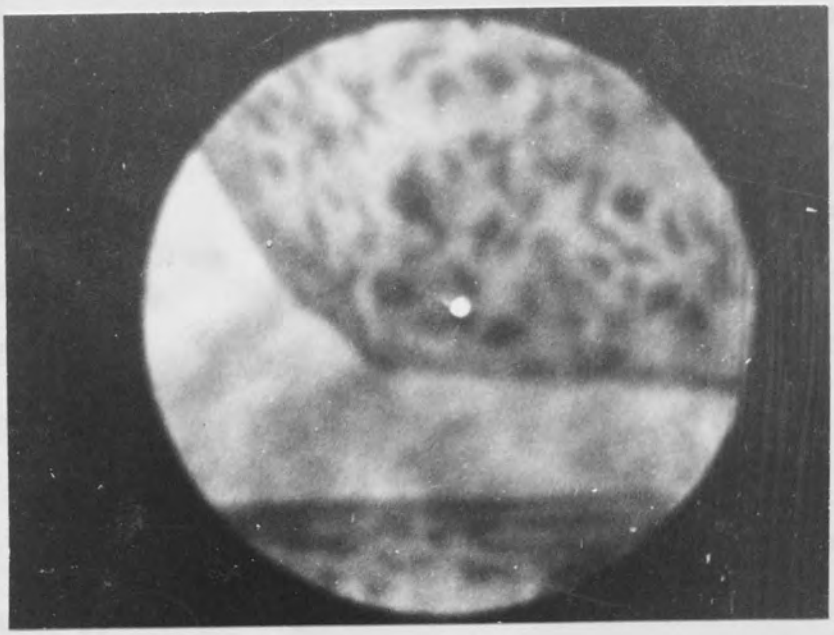

(b)

Figure 8.3 (a) Micrograph of ink particles on a carbon film supported by a copper grid. Electron optical magnification 1600 X, total magnification 3200 X.
(b) Micrograph of ink particles on a carbon film supported by a copper grid. Electron optical magnification 2800 X, total magnification 5600 X.

9 A MINIATURE SCANNING MICROSCOPE

9.1 Introduction

The results obtained with the miniature transmission electron microscope suggested that single-pole lenses could be used successfully in the scanning mode. The large amount of free space below the snorkel lens seemed attractive for the positioning of large specimens. It was also thought that the guiding influence of the magnetic flux lines would enable secondary-electrons to be extracted from the specimen, in spite of immersion in the magnetic field. The large take-off angle for X-ray analysis and low aberations of the objective lens combine to produce a system ideally suited to scanning electron microscopy. This chapter describes the attempts to detect secondary-electrons and produce a system demonstrating the feasibility of a miniature scanning instrument utilising these principles.

9.2 Collection of secondary-electrons

Until recently it was considered that extraction of low energy secondary-electrons emitted by a specimen immersed in a strong lens field was not practicable. However, (Koike, Ueno and Suzuki 1971) and (Kimura and Tamura 1967) devised effective extraction methods for conventional magnetic electron lenses. The snorkel magnetic lens seems to offer a simple possibility for the extraction of the secondary-electrons since the radial

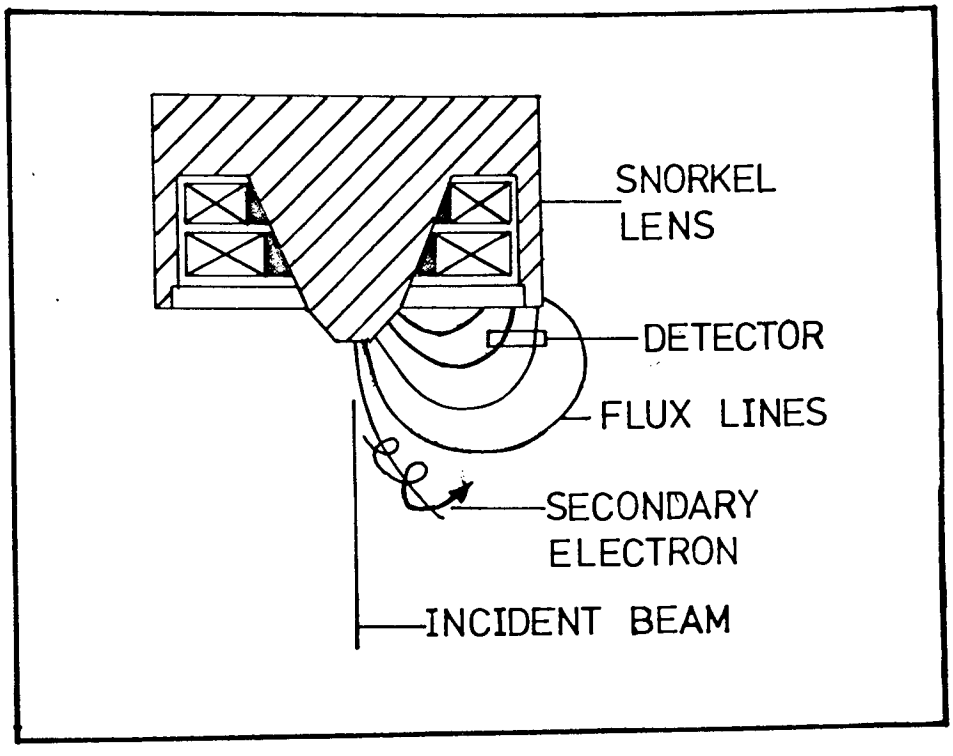

Figure 9.1 Low energy secondary-electrons spiralling around the magnetic flux lines of a radial-field lens towards the secondary-electron collector.

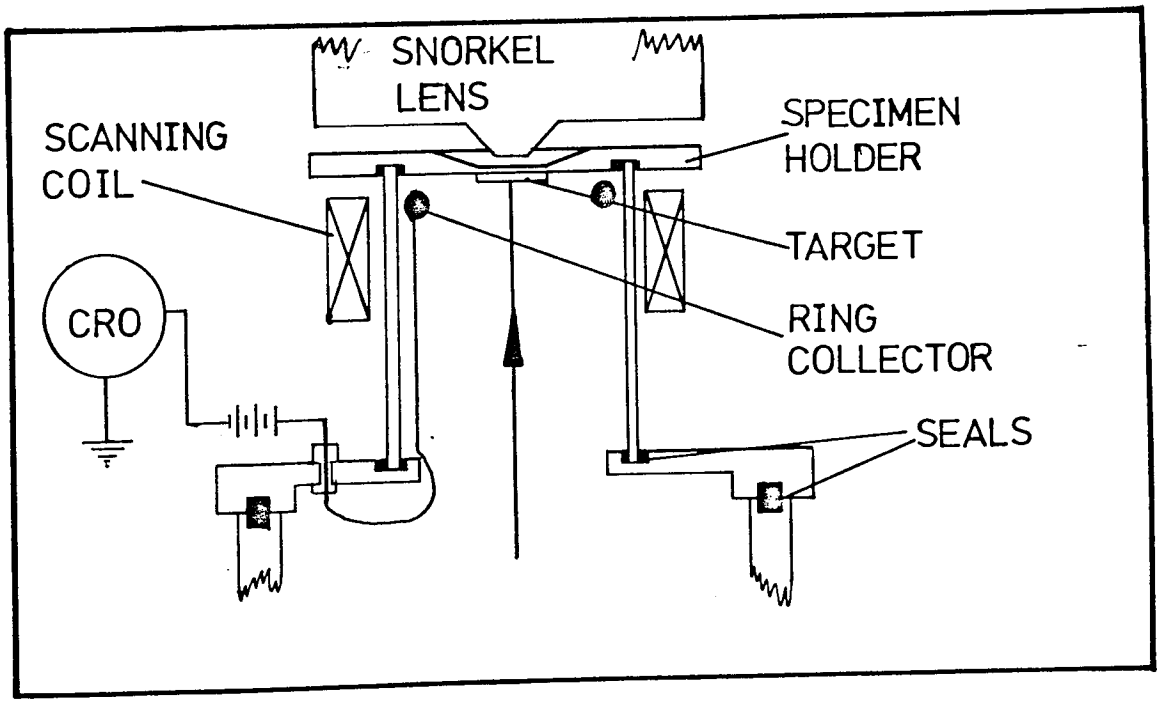

Figure 9.2 Position of the secondary-electron detector in the experimental scanning electron microscope, showing the duralumin target, scanning coils and probe forming lens.

direction of the lines of flux could lead conveniently to an annular detector. The low energy secondary-electrons tend to spiral round the flux lines and, in principle, can be collected on the outside diameter of the lens. Figure 9.1 shows an experimental arrangement for achieving this. A secondary-electron detector mounted in this position should collect very few back scattered electrons of high energy, approximately 5.0%, see Appendix 6. The first experimental detector is shown in Figure 9.2. The target was a duralumin disc with a phosphor coating mounted on the specimen holder. The results from the detection experiments are shown in Figure 9.3 and confirm that secondary-electrons were being detected, but a large contribution of the detected current appeared to come from back-scattered electrons multiply-scattered from the lens structure, and electrons emitted by the structure in the column. The probe current was 0.3 μA at 3.8 kV

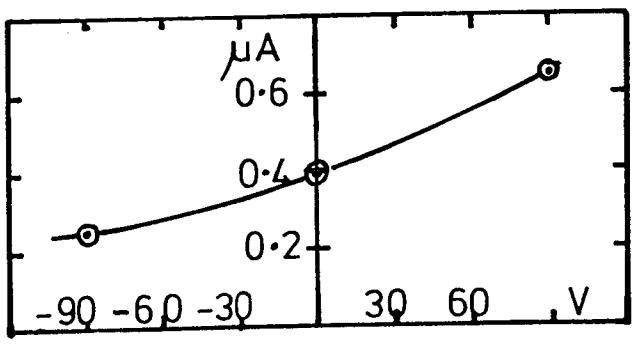

Figure 9.3 Secondary-electron current measured as a function of applied collector voltage.

9.3 The first experimental scanning system.

Figure 9.4 shows the first crude attempt to construct a miniature scanning electron microscope with a

single-polepiece objective lens. In order to simplify the detector system a probe size of the order of 0.1 μm was aimed at. The condenser or intermediate lens, capable of demagnifying the electron source by 16 times, was mounted directly over the electron gun. This lens was in fact the projector lens described in Chapter 6, section 3. The snorkel lens was mounted outside the vacuum system and supported by the specimen stage. For simplicity no provision was made for mechanical movement of the specimen, since the scanning system could be employed to search the specimen. The scanning coils used were a single pair of coils each of 100 turns externally mounted on a glass tube 33 mm apart and placed just below the specimen as shown in Figure 9.4. This experimental column was designed to demonstrate that it is feasible to produce a reflection scanning electron microscope with a large solid angle of escape for X-rays and which would also be compatible with a high vacuum system. this instrument operated at 30 kV and produced a total demagnification of 80 times to give a final probe size of 0.7 μm. The spherical aberration coefficient C_s was 1.5 mm and the theoretical resolving power was 60 nm. Following successful operation of this instrument an improved system was assembled as shown in Figure 9.5. In this experimental 30 kV scanning electron microscope the electron beam travels upwards, as before, but encounters a wide bore (4 mm) rotation-free intermediate lens, focal length 1 mm, before being brought to a focus on a specimen

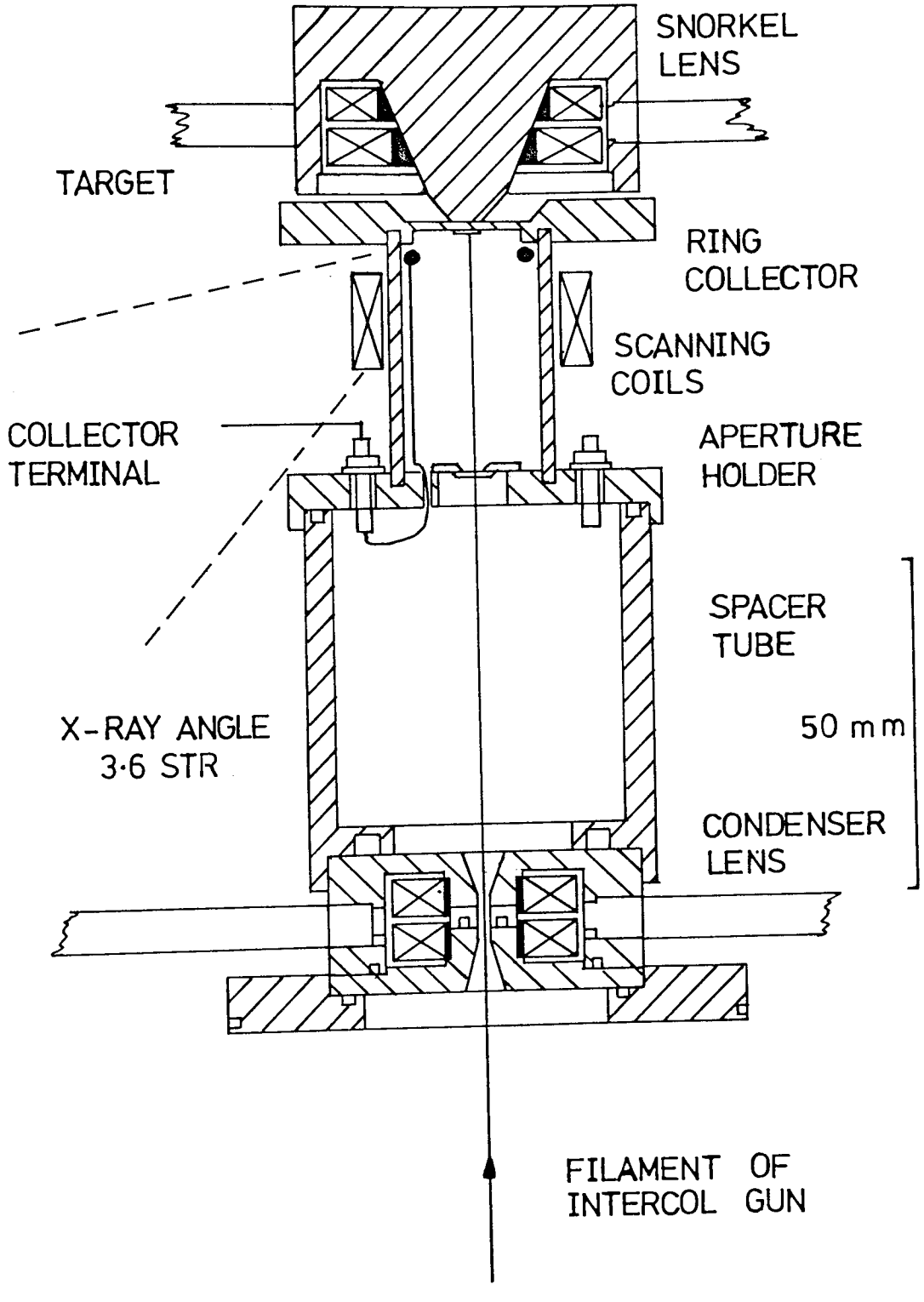

Figure 9.4 Experimental Scanning Microscope. The intermediate lens is a miniature conventional twin polepiece lens. The objective is a single polepiece radial field lens having no bore and mounted completely outside the vacuum system. Note the very large X-ray take-off angle.

by a snorkel lens, which as in the previous instrument was mounted completely outside the vacuum, (Mulvey & Newman 1973, Appendix 2). Figure 10 in Appendix 2 shows the scanning system using the rotation-free lens developed by Juma and Mulvey for the transmission electron microscope. Its focal length 0.17 mm, is very short, and bore 2 mm, (Juma & Mulvey 1974). In practice this lens was found to be too powerful producing a gaussian probe size of some 40 nm, far too small for detection by simple electron collectors and calling for instrumental and electrical stability greater than was available in the Intercol electron-optical bench. Hence the intermediate lens shown in Figure 9.5 was designed and built. This is a doublet consisting of two single-pole lenses mounted back to back. External scanning coils placed below the specimen scan the beam across the specimen, which is mounted on a thin non-magnetic plate, in close proximity to the snout of the snorkel lens. This instrument produced a probe size of 0.2 μm. It was also possible to operate this instrument using only one half of the intermediate lens, producing a probe size of 1 μm.

9.4 The detection of secondary electrons.

In the schematic diagram of the first scanning microscope, shown in Figure 9.4, a ring collector may be seen. This is in approximately the correct position to avoid high energy back-scattered electrons and, with a suitable collecting voltage applied to it, should draw out of the lens field the low energy secondary-electrons. The

Figure 9.5 A 30kV scanning electron microscope. The intermediate lens is a rotation-free double snorkel lens. The objective lens is a single snorkel lens and is completely outside the vacuum system.

secondary-electron current of some 50 μA produced by the electron beam hitting a phosphor coating on the specimen was allowed to leak to earth via a 1 megohm resistor. The potential difference across this resistor was displayed on an oscilloscope causing the trace to drop about 0.5 volts as the electron beam traverses the phosphor coating. Normally the secondary-electron current is about 10^{-12} A and a low frequency amplifier has to be employed. This system was now employed to display the image of a specimen grid. The grid was mounted over a phosphor coating to produce greater definition in the corresponding secondary-electron current. This system proved unsuccessful mainly due to the fact that the probe size, 30 μm, was of the same order as that of the grid bar. The placing of an aperture in this system to produce a more favourable spot size led to the idea of producing a better system which would demonstrate qualitatively if not quantitatively the feasibility of such a system.

9.5 The scanning transmission electron microscope.

The experimental difficulties encountered above were circumvented by projecting a shadow image of the grid onto a distant fluorescent screen. A hole was bored in the specimen holder and through the polepiece of the snorkel lens. On top of the snorkel lens was placed a spacer tube capped by a transmission screen as shown in Figure 9.6. This effectively converted the previous scanning microscope into a scanning transmission microscope. With the instrument set up in this way, a transmission shadow

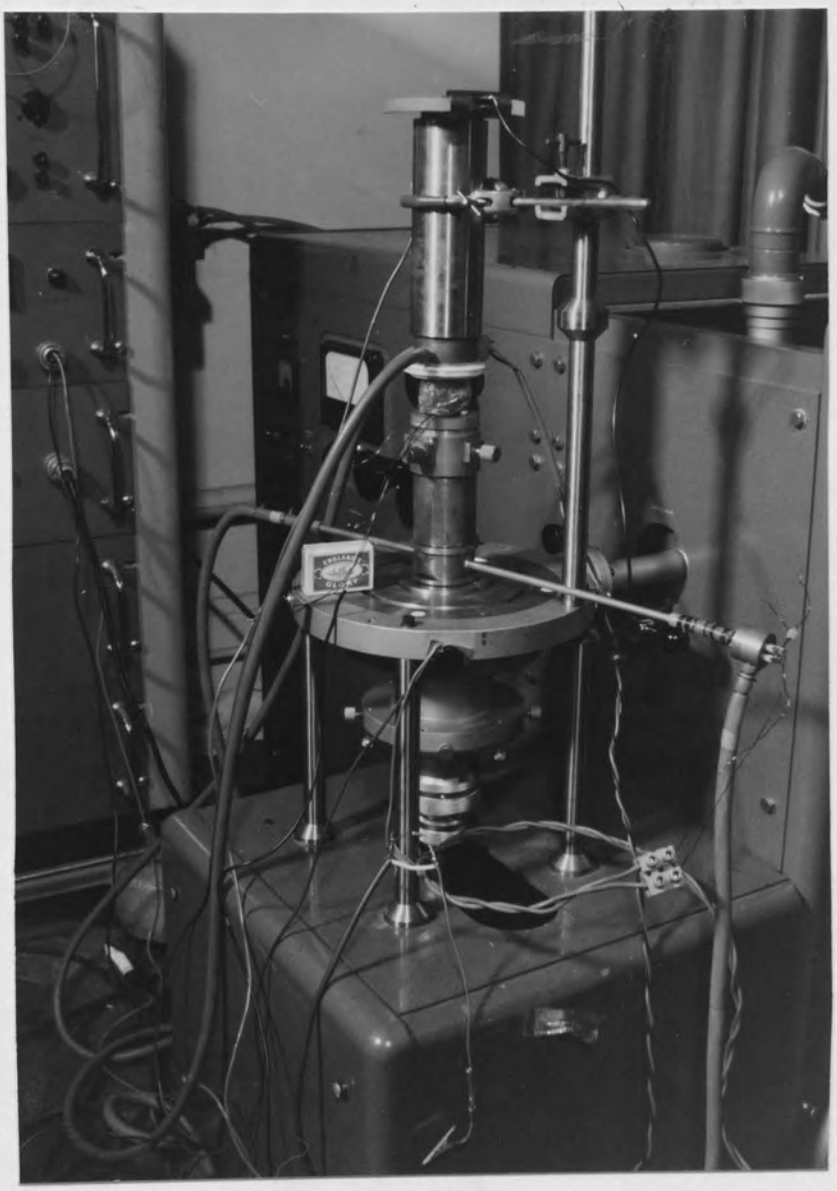

Figure 9.6 Miniature scanning transmission electron microscope using the 100 kV EM6 projector lens as the intermediate lens. The snorkel objective now has a bore through it.

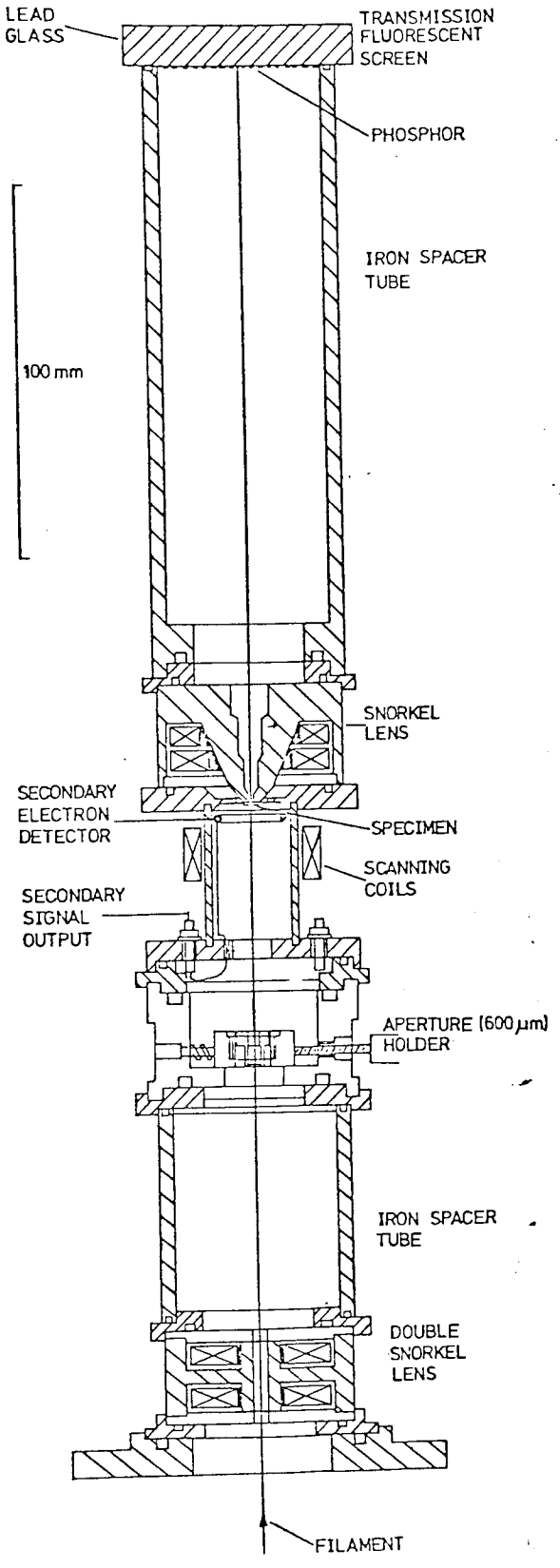

Figure 9.7 The Scanning Transmission Microscope, made up entirely of snorkel type lenses. The intermediate lens is a rotation free double snorkel lens and the objective a single snorkel lens

of a specimen grid was projected on the screen. The sharpness of this image served to indicate the spot size. As the current in the snorkel objective was increased, a position was found where the magnification of the projected pattern was "infinite", corresponding to the probe being focussed in the plane of the specimen. This is then the position for operation in the scanning mode. With the system operating in this mode, the signal collected at the screen had a sine wave appearance rather than the square wave one expected from scanning across a grid. A suitably positioned aperture brought the probe size down to 1 μm producing a considerable improvement in resolution and sharpness in the scanning trace on the oscilloscope. Figure 9.7 shows the final version of the scanning transmission microscope with a theoretical spot size of 0.2 μm., (using half the double snorkel lens). However, it was found that instrumental defects such as pick-up in the amplifying system and the presence of stray a.c. fields severely affected the performance.

In the limited time available it did not prove possible to redesign the scanning system and pick-up arrangements. Consequently, the resolving power was limited to about 10 μm as indicated by the trace of the line scan shown in Figure 9.8. The specimen is a rectangular copper grid (75/300 mesh) of dimensions indicated by the attached scale of 1.0 mm.

One can conclude from this experiment that such a scanning system is indeed feasible but more detailed

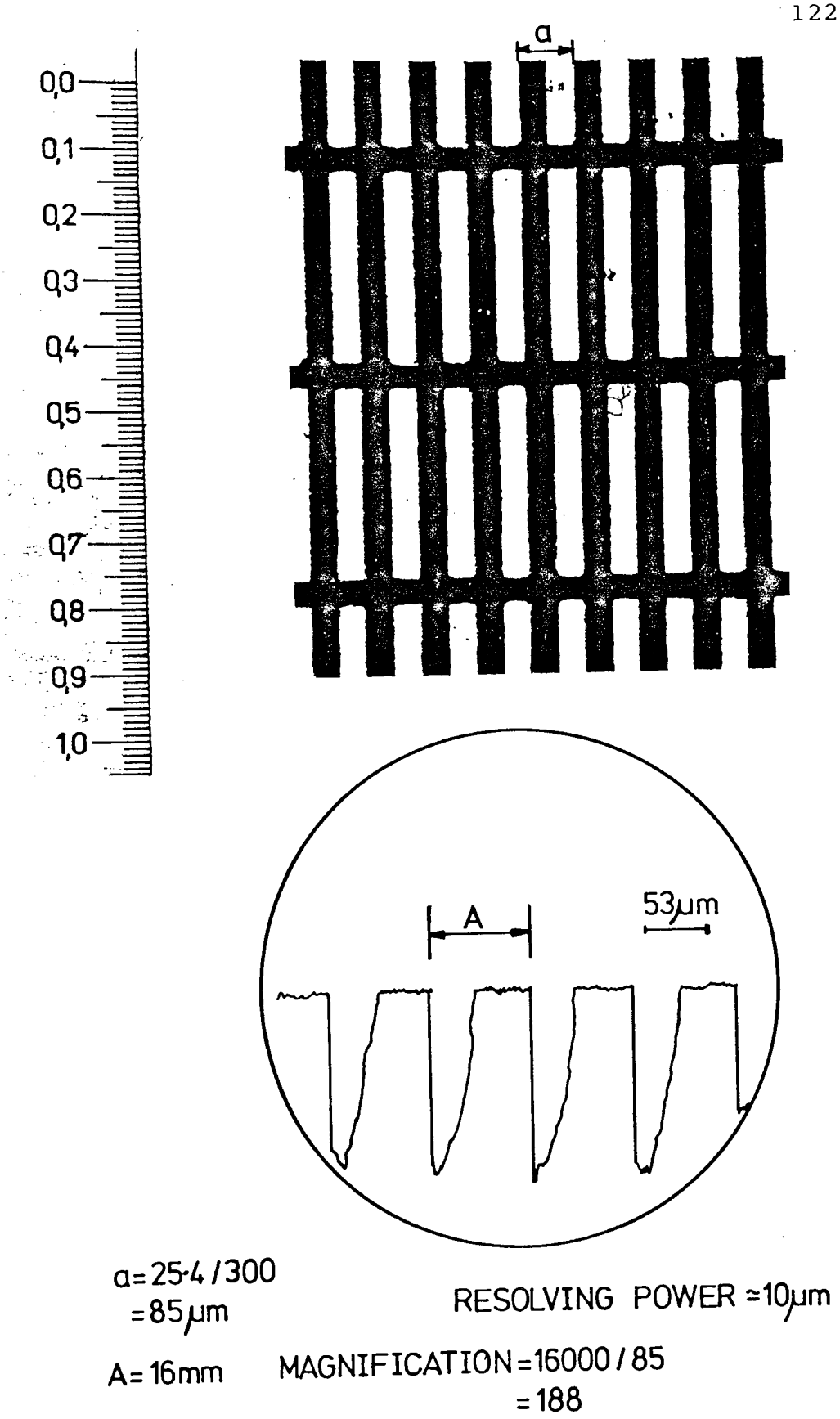

Figure 9.8 The 75/300 copper grid, with 1 mm scale, and a line scanning image obtained from the scanning transmission electron microscope.

investigation is needed into the design of an optimum scanning system and electron collector.

It was therefore decided not to proceed further with the above microscope but to concentrate attention on the feasibility of realising a snorkel projector lens for a million volt electron microscope as described in the following chapter.

10. MINIATURE LENSES FOR HIGH VOLTAGE MICROSCOPY

10.1 A single-polepiece lens for high voltage microscopy

An obvious field of application for lenses of reduced size is in high voltage microscopy. High voltage electron microscopes have been mainly of traditional design, being essentially scaled up versions of 100 kV instruments, necessitating expensive buildings and services. This has tended to restrict the growth of high voltage microscopy. A typical conventional 1 MV electron lens with 20 000 A-t has a diameter of some 45 cm, a length of some 20 cm, a weight of 250 kg and a focal length in the region of 10 mm. Furthermore, conventional electron lenses are not well adapted to high vacuum systems called for by recent developments in electron sources. Moreover, in future, super-conducting windings may be needed requiring further modification of traditional lens designs. The miniature lenses so far described are extremely small and could readily be increased in size to accommodate the increased number of ampere turns required at one million volts without departing from the simple constructional techniques described in previous chapters.

Although it seemed feasible to design and construct a miniature lens for a million volt electron microscope, there seemed little chance of testing it out under realistic conditions, without seriously disrupting the operation of the high voltage microscope concerned.

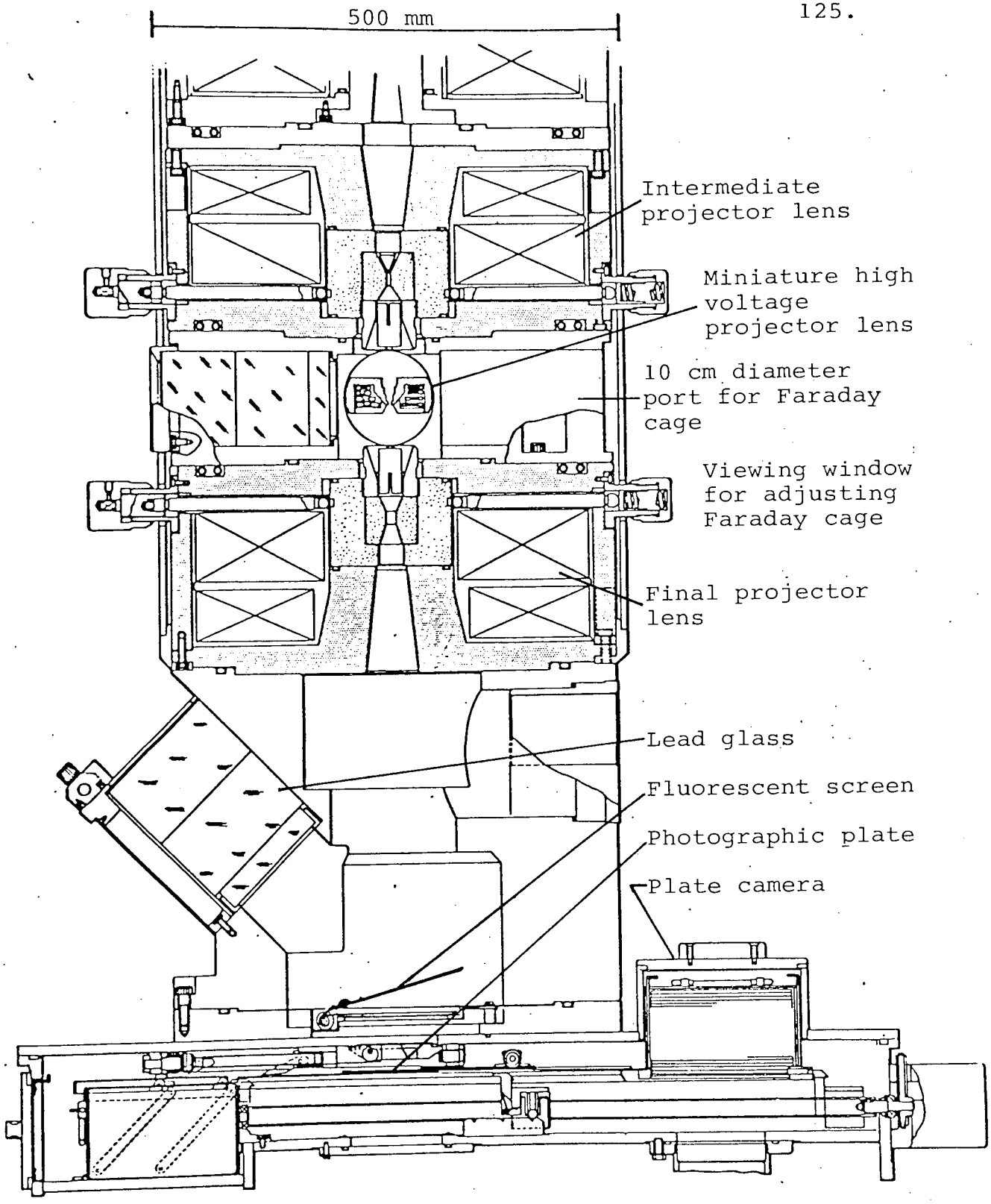

Figure 10.1. Cross-section of Hitachi HU 1000 million volt electron microscope showing intermediate and final projector lens. Miniature projector lens inserted in Faraday cage port above the final projector lens.

However, a possibility seemed to exist of fitting a miniature projector lens into the million volt Hitachi HU 1000 electron microscope (Figure 10.1) since a port-hole of 10 cm diameter is available above the final projector lens; this normally houses a Faraday cage. It seemed worthwhile to investigate the possibility of removing the Faraday cage and inserting a miniature lens into position in the column with the intention of using it as the final projector lens.

10.2 The preliminary and final design

In conjunction with the C.E.G.B. Research Laboratories at Berkeley, it was arranged that if a suitable miniature electron lens could be constructed, it could be tested on their Hitachi HU 1000 microscope at an operating voltage of 1000 kV. Further study indicated however that several extremely stringent conditions had to be satisfied in the design of such a lens. It was clearly desirable to be able to carry out the experiment without any modification to the existing electron-optical column of the HU 1000. Not only was it necessary for the minilens to fit into the existing 10 cm diameter porthole above the final projector lens, but all arrangements for alignment, water cooling and current leads had also to be incorporated and mounted on a single flange. Figure 10.1 gives an idea of the limited space available for the lens in the column. Figure 10.2 shows an early attempt at designing a suitable single-polepiece lens with tape windings to satisfy the electron-optical and general mechanical conditions. The outside diameter of the lens

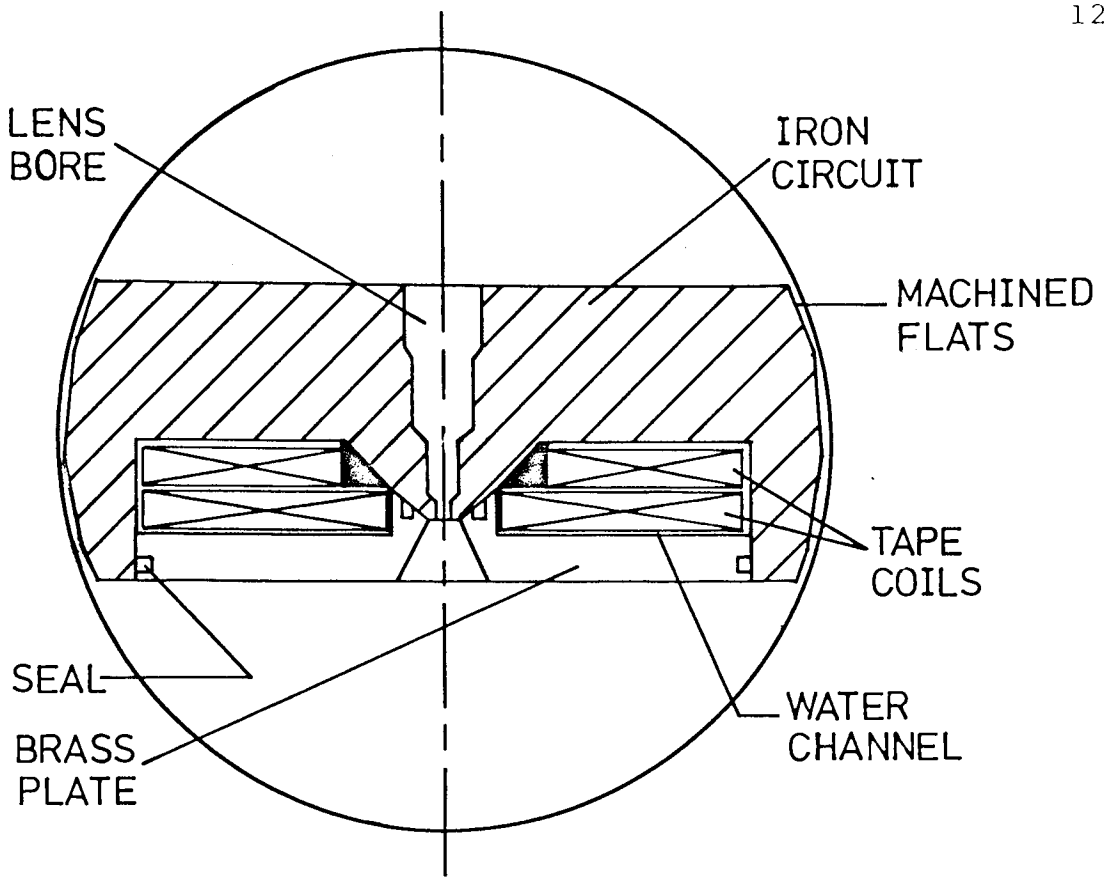

Figure 10.2 Preliminary design for a 1 million volt lens to fit into a 10 cm porthole. Full size. Diameter of circle 10 cm.

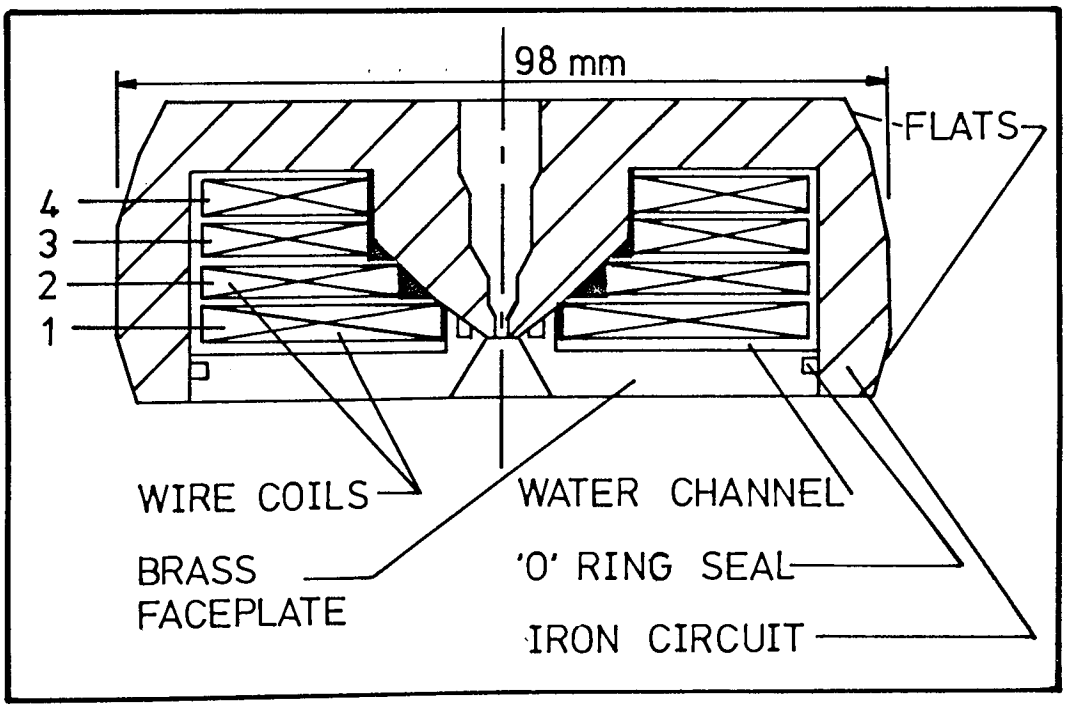

Figure 10.3 Miniature 1 million volt projector lens modified for wire windings. Full size. Bore diameter = 2.25 mm.

was fixed at 98 mm, i.e. approximately twice the size of the snorkel of focal length 4.9 mm described in Chapter 7. Simple scaling would lead one to expect a minimum projector focal length of about 10 mm for the design shown in Figure 10.2. Also, an outer diameter of 98 mm is just sufficient to allow an adjustment of $\pm$ 1 mm in the final position of the lens. The magnetic circuit was turned from a single piece of iron. In order to allow the lens to be inserted into a 10 cm diameter porthole, it was necessary to machine two flats on the appropriate sides of the cylindrical lens casing. As suitable tape windings were not available immediately preliminary experiments were carried out with temporary wire coils at a reduced number of ampere turns (4 800 A-t) to determine the chief magnetic characteristics. Extrapolation of these results to an excitation of 20 000 A-t indicated that with this excitation, the pole-face flux density would be in the region of 2.3 T in the immediate vicinity of the pole-face. These tests indicated however that the design of a suitable tape winding for 20 000 A-t in this restricted space, would cause considerable technical difficulties. The calculations previously given in Chapter 3 supported this view. In addition, at the time, the available power supplies were limited to an output of 3 kW, which was not sufficient for developing more than about 15 000 A-t. Further calculations (Chapter 3) showed that an excitation of this order could be provided by removing some of the magnetic circuit to provide extra space for

Figure 10.4 Front view of the million volt single-pole piece projector lens showing the water and electrical connections. Maximum diameter 98 mm. Weight of the four lens coils = 0.486 kg, weight of the lens shell and pipes = 1.6 kg. Total weight of lens = 2.1 kg.

ordinary wire coils without undue magnetic saturation effects. Since such coils are very much easier and quicker to manufacture than are tape coils it was decided to proceed on these lines. The re-designed magnetic circuit and coil arrangement is shown in Figure 10.3, and the completed lens is shown in Figure 10.4. The extra winding area and simplified construction seemed to offer the possibility as discussed in Chapter 3 of an excitation of about 14 000 A-t, sufficient for producing a projector focal length less than 20 mm; assuming a minimum focal length of the order of 10 mm at an excitation of 20 000 A-t and an accelerating voltage of 1 MV. This is perfectly acceptable, especially if one considers that the weight of this lens was only just in excess of 2 kg, compared with the 250 kg of the normal HU 1000 projector lens, (Mulvey and Newman 1973b).

10.3 Laboratory testing of the high voltage lens

Magnetic performance

Figure 10.5 shows the measured maximum axial flux density at the poleface. The figure shows that up to an excitation of some 10 000 A-t, the axial flux density is linear with excitation. At an excitation of about 12 000 A-t, a loss of some 1 700 A-t (14%) appears to take place in the iron circuit as indicated in Figure 10.5. These tests indicated that an acceptable electron optical performance could be obtained at 1 MV. Subsequent calculations of the axial field distribution, as shown in Figure 10.6, kindly carried out by W. Trowbridge at the Rutherford Laboratory using the GFUN

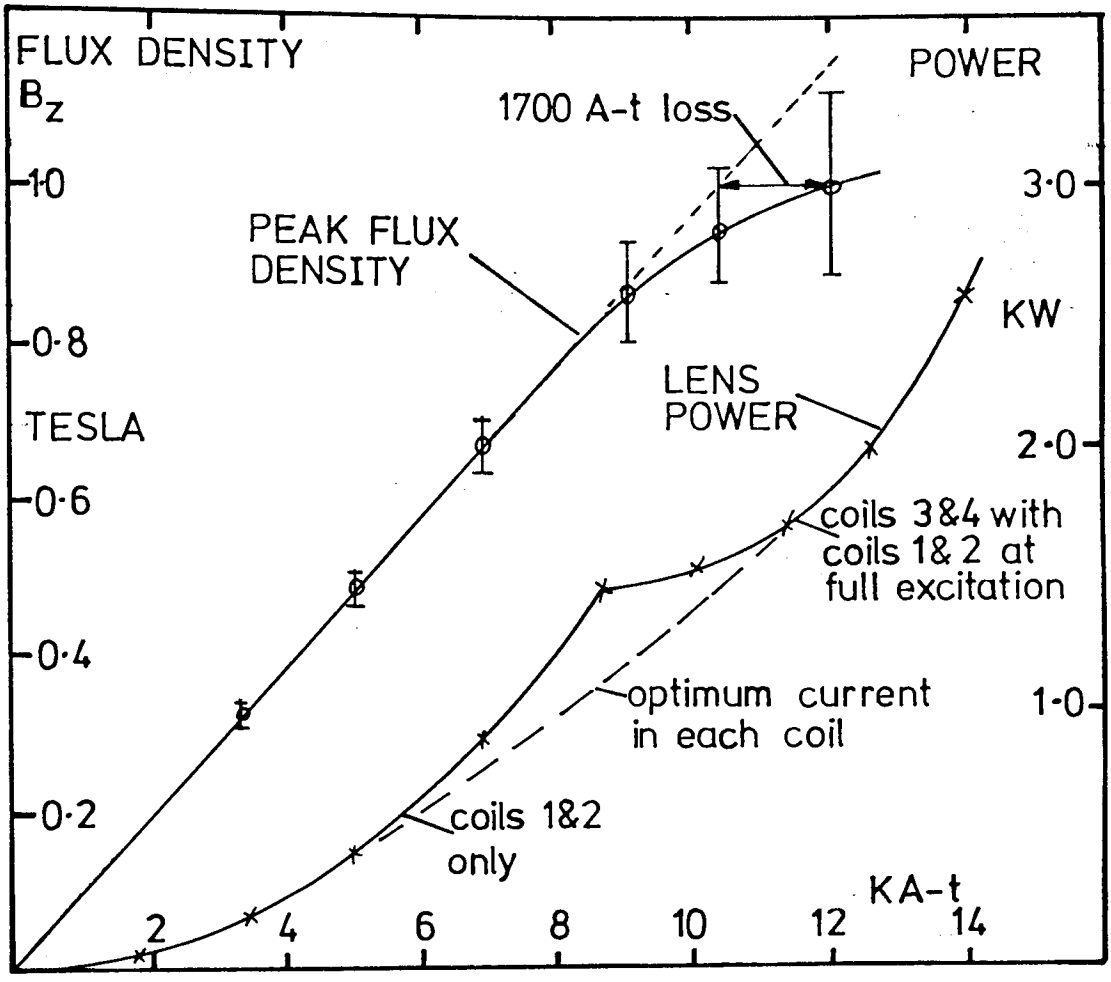

Figure 10.5 The measured peak axial flux density and power input as a function of excitation in the miniature high voltage lens.

magnetic design program, show the reason for this limitation. Owing to the cramped space available and the removal of iron to accommodate the wire winding, the diameter of the snout in the region of the poleface is slightly too small, causing the appearance of an unwanted magnetic field peak in the polepiece, located about 3 mm from the snout face. The measured axial flux density distribution (Figure 10.5) shows that the experimental values agree with those calculated by Trowbridge within the accuracy of measurement (5%). It was also found that

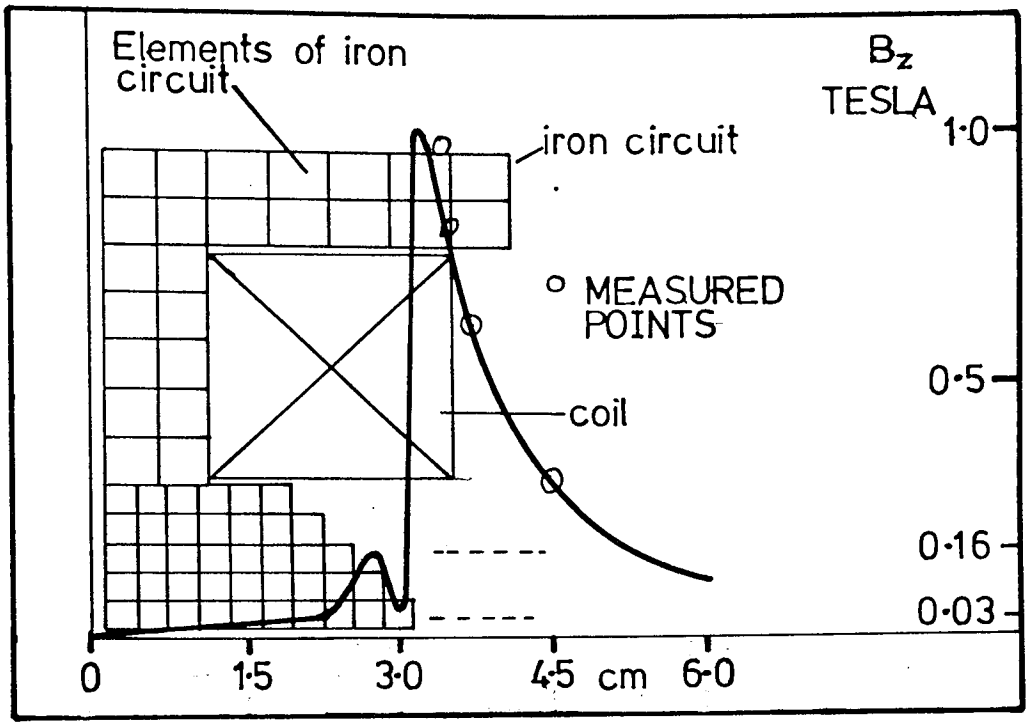

Figure 10.6. The 'GFUN' calculation of the axial flux density distribution of the 1 MV lens. For ease of computation the model used in the calculation had a 2 mm bore and a stepped snout. The actual lens, shown in Figure 10.3 had a stepped bore and a smooth conical snout.

coils 1 and 2 together (packing factor $\lambda = 0.65$) could produce 8 600 A-t for an expenditure of 1.4 kW and coils 3 and 4 together ($\lambda = 0.65$) could produce 5 000 A-t for an expenditure of 0.9 kW. However, coils 3 and 4 were found to run very hot at this power input and so were, in fact derated to 3 800 A-t for an input power of 0.4 kW. Thus the total excitation available for continuous running was 12 400 A-t for a power input of 1.8 kW supplied by two separate power supplies. This was also the useful limit set by the iron circuit because of the high flux density in the region of the snout. The relation between excitation produced and the power

required is shown in Figure 10.5. This shows that coils 1 and 2 near the snout are more efficient at producing ampere-turns than coils 3 and 4 placed further from the snout. This is entirely consistent with the calculations given in Chapters 2 and 3.

Focal properties of the million volt lens

A preliminary study of the projector focal properties of this lens was made on an Intercol Electron Optical bench at an accelerating voltage of 30 kV, at this voltage no saturation effects are present. Figure 10.7 shows the experimental details. An electron microscope grid was fixed directly onto the pole-piece bore of 2.25 mm diameter. The resulting projected images of the grid on the fluorescent screen at different excitation parameters ($NI/V_R^{\frac{1}{2}}$) are also shown in Figure 10.7. The projector focal length (f_p) can be determined as follows. The magnification M at the screen is given by $M = (L-f_p)/f_p$ Figure 10.7, for the principal plane situated at the pole-face. The projector focal length is therefore given by $f_p = L/(M+1)$. This method is only accurate for f_p near the minimum i.e. when the lens is strong and the principal plane is situated at the pole face. It was possible to check electron-optically the diameter (2.25 mm) of the bore of the mini-lens by counting the number of grid squares (Figure 10.7), for example in micrograph 3, across the mini-lens bore. This method can only be used at low excitations. At high excitation, saturation effects in the pole-piece cause the unwanted field in the lens bore, see Figure 10.6, and this will have a focusing

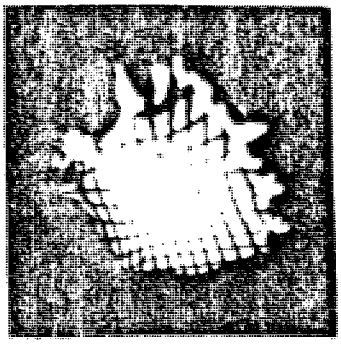

$NI/V_R^{\frac{1}{2}} = 8.0$

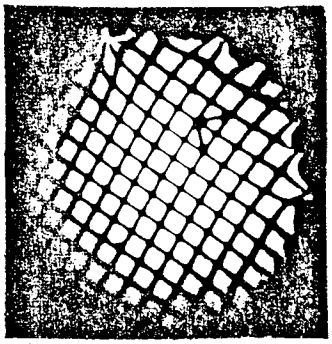

$NI/V_R^{\frac{1}{2}} = 12.1$

$f_p = 11.2 \pm 0.7$ mm

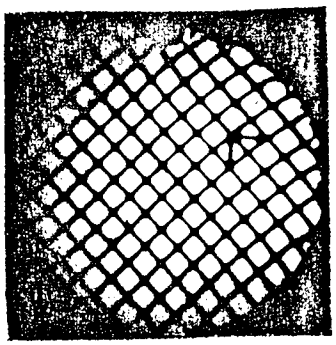

$NI/V_R^{\frac{1}{2}} = 14.1$ (3)

$f_p = 10.2 \pm 0.7$ mm

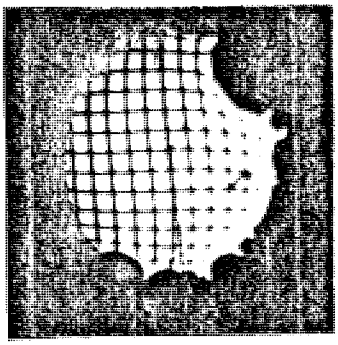

$NI/V_R^{\frac{1}{2}} = 18.1$

$f_p = 11.2 \pm 0.7$ mm

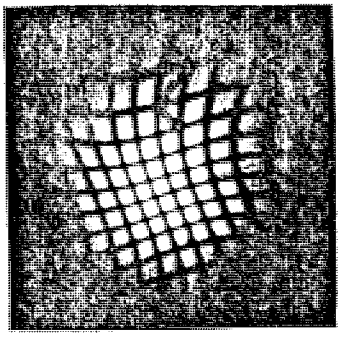

$NI/V_R^{\frac{1}{2}} = 28.1$

$f_p = 14.0 \pm 1.0$ mm

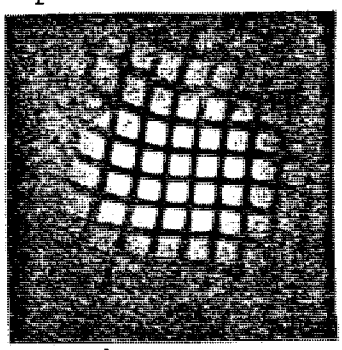

$NI/V_R^{\frac{1}{2}} = 30.1$

$f_p = 9.2 \pm 0.6$ mm

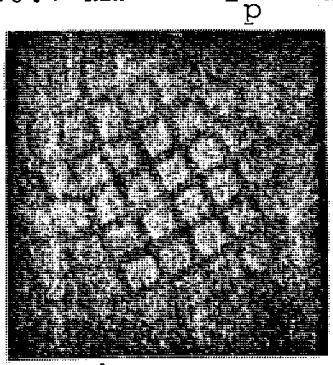

$NI/V_R^{\frac{1}{2}} = 34.2$

$f_p = 6.7 \pm 0.5$ mm

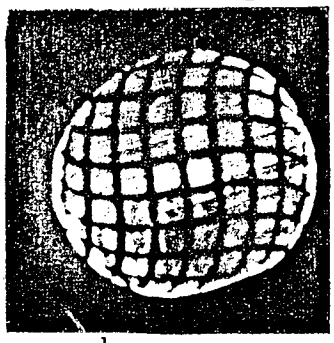

$NI/V_R^{\frac{1}{2}} = 38.2$

$f_p = 7.6 \pm 0.5$ mm

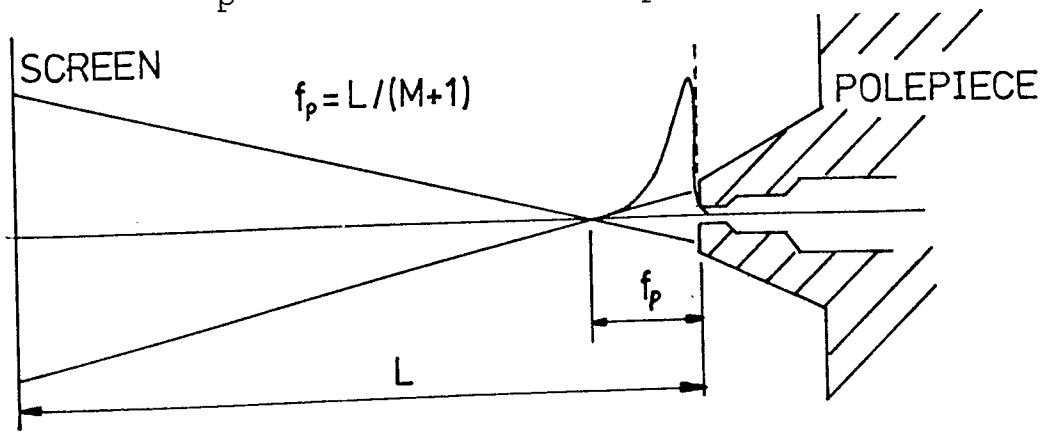

Figure 10.7. The experimental procedure to determine the projector focal properties of the high voltage lens and the micrographs obtained. Micrograph No. 3 was the one used to determine the diameter of the bore of the mini-lens.

effect on the beam, before the beam reaches the grid and hence not all the plane of the lens bore containing the grid will be illuminated.

Figure 10.8, solid lines, shown the normalised projector focal length ($f_p/f_{p\ min}$) versus normalised excitation parameter NI/NI' as discussed in Chapter 4 (Figure 4.4). The normalised experimental points for the million volt lens obtained at an accelerating voltage of 30 kV are shown on the graph. The experimentally measured minimum focal length was 10 mm at an excitation of $NI/V_R^{\frac{1}{2}} = 15.2$. Figure 10.8 indicates that these normalised focal properties can be used as a good guide to the performance of single-polepiece projector lenses especially if the minimum projector focal length and excitation can be determined experimentally. For this lens to work at its minimum projector focal length at an accelerating voltage of 1 million volts an excitation of 21 500 A-t is required, in good agreement with the estimated figure of 20 000 A-t given in Chapter 3. With the 12 500 A-t available corresponding to NI/NI' = 0.58 a projector focal length of 1.65 $f_{p\ min}$ appears possible, namely a projector focal length of about 17 mm, as indicated in Figure 10.8.

At a later stage in the investigation a more direct calculation became available. These calculated focal lengths were kindly provided by F.Z. Marai and are shown in Figure 10.9, solid lines. These calculations are based on the flux density distribution shown in Figure 10.6. These are in good agreement with the

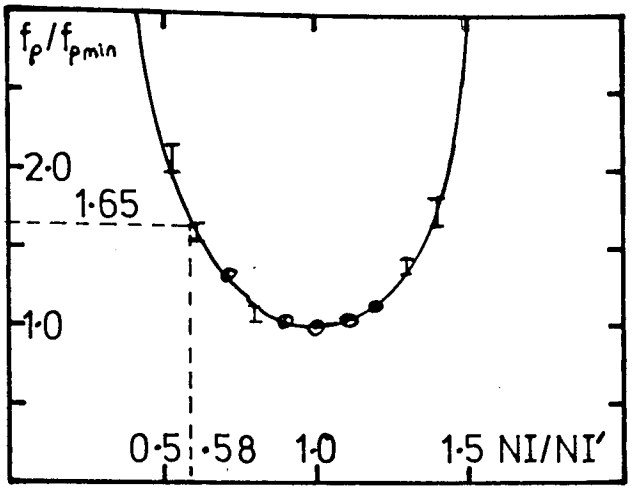

Figure 10.8. Normalised projector focal length f_p/f_{pmin} as a function of normalised excitation NI/NI'. Solid line, calculated from rectangular field distribution or from "half-field" of an iron free lens of D_2/D_1=19.0, I, experimentally measured points at an accelerating voltage of 30 kV. f_{pmin}=10 mm NI/NI'=15.2 .

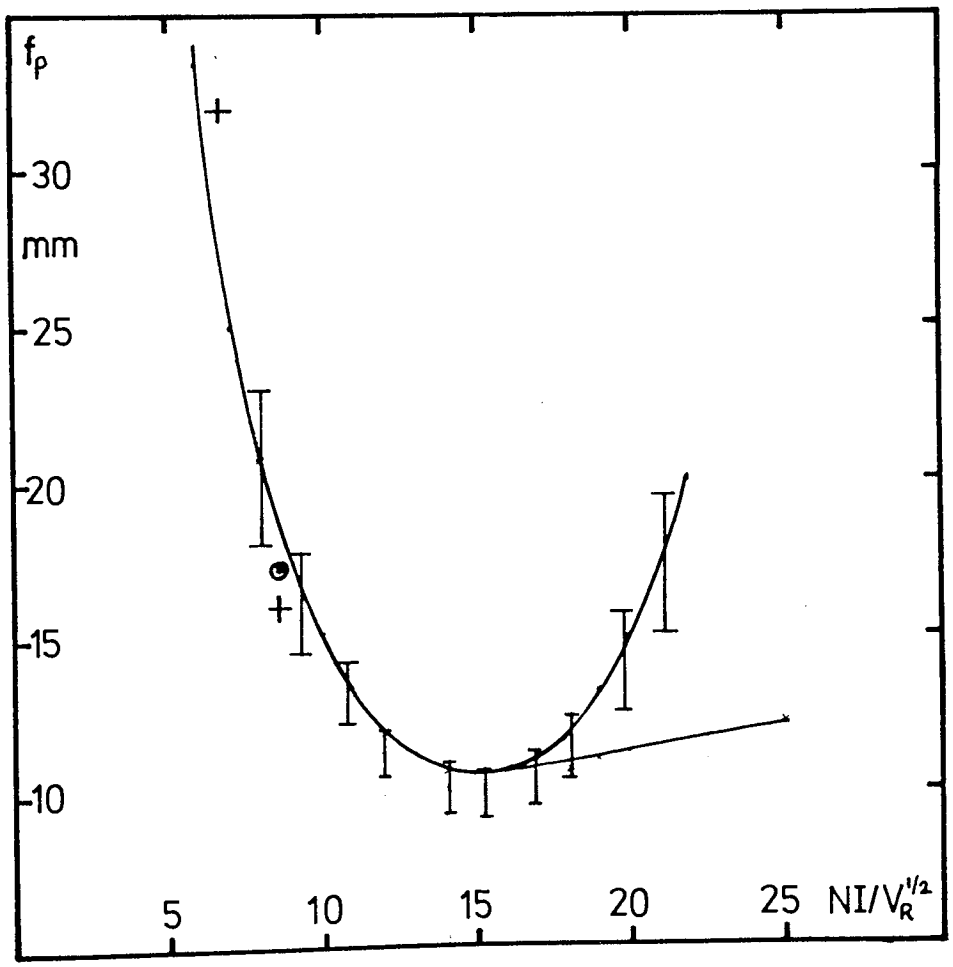

Figure 10.9. Projector and objective focal properties of the high voltage lens. Solid line, calculated from the field distribution determined by the GFUN progam. I, experimentally determined points at 30 kV. +, ⊙ experimentally determined points at 1 MV.

calculated values but there is a slight but systematic deviation between the two curves. This arises as follows. It was not possible to model the magnetic circuit exactly of the 1 MV lens shown in Figure 10.3 in the calculations of flux density in the magnetic circuit. For simplicity the lens bore was taken as a constant 2 mm through the lens, and not stepped as in the real lens. Similarly, the snout had to be modelled using a rectangular mesh; it was therefore necessary to represent the conical sides of the snout as a series of steps. These approximations are entirely justified under normal conditions of excitation, but may become important when saturation effects are present, namely at excitations in the region of 12,000 A-t. The calculated minimum projector focal length was 10.7 mm at an excitation parameter $NI/V_R^{\frac{1}{2}}$ of 15.5, in good agreement with the experimental results. The second cause of discrepancy is due to the experimental difficulty of measuring focal lengths at weak excitation. In general the accuracy of the method is greatest in the region of the minimum focal length. Here the agreement between theory and experiment is particularly good.

10.4 Testing the lens in the HU 1000 at C.E.G.B. Berkeley.

The miniature lens was assembled into the porthole of the HU 1000 electron microscope at the C.E.G.B. Berkeley Research Laboratories. Figure 10.10 shows the complete lens unit (underside view), with modified water cooling pipe. In the laboratory tests the lens unit had a water pipe each side of the casing, as in all the previous designs. It was necessary to modify this lens as access

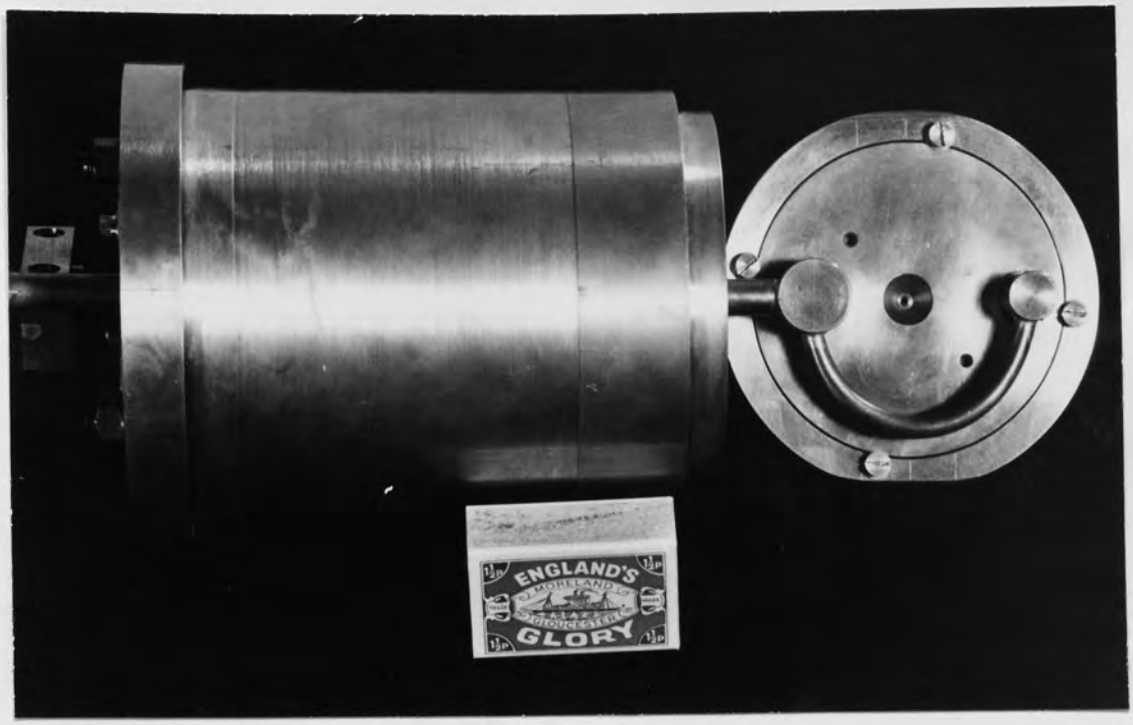

Figure 10.10 Underside view of the million volt lens with modified water cooling pipe assembled in the brass mounting plug, (X-ray shield).

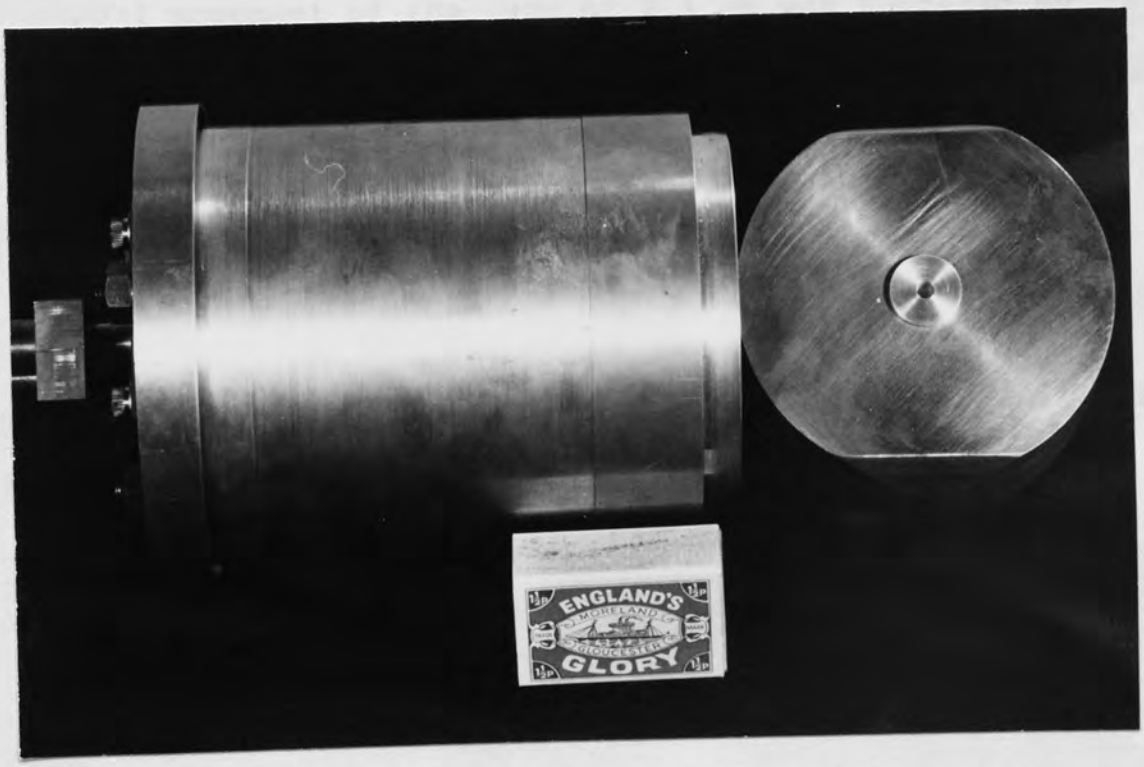

Figure 10.11 The million volt lens, viewed from above showing the duralumnin X-ray limiting aperture (18.6 mm dia.), in the lens bore. Notice the flats machined on the lens surface to allow entry of the lens into the porthole.

to the HU 1000 was possible from one side only. In the final version of the high voltage mini-lens the water inlet pipe was mounted on the brass face-plate of the lens and routed around the lens face and out alongside the water outlet pipe, as can be seen in Figure 10.10. The electrical leads were brought out of the lens via the water outlet pipe as it was easier to seal the electrical connector box from water leaks on the outlet side of the cooling system. The brass plug of 10 cm diameter, much heavier than the lens, provided an alignment datum and support for the lens as well as X-ray shielding to protect the operator whilst adjusting the lens. The cooling water-pipes passed through 'O' ring seals, which acted as a fulcrum permitting a lateral movement of the lens of ± 1 mm. A radial movement of the lens of ± 1 mm was achieved by sliding the water pipes through the 'O' ring seal. Figure 10.11 shows the view from above, revealing the flats machined on the sides of the lens to allow entry into the porthole, and the duralumin aperture. Figure 10.12 gives the details and dimensions of this duralumin X-ray limiter. As aluminium has a smaller atomic number than iron the X-ray dose produced by possible electron bombardment will be reduced considerably. Figure 10.13 is a detailed drawing of the arrangement of the mini-lens inside the porthole.

The pump-down time of the HU 1,000 after inserting the lens was about 1½ hours. When an adequate vacuum had been achieved in the column, the normal lenses of the HU 1000 were energised, the mini-lens excitation being switched off. Since the diameter of the snorkel

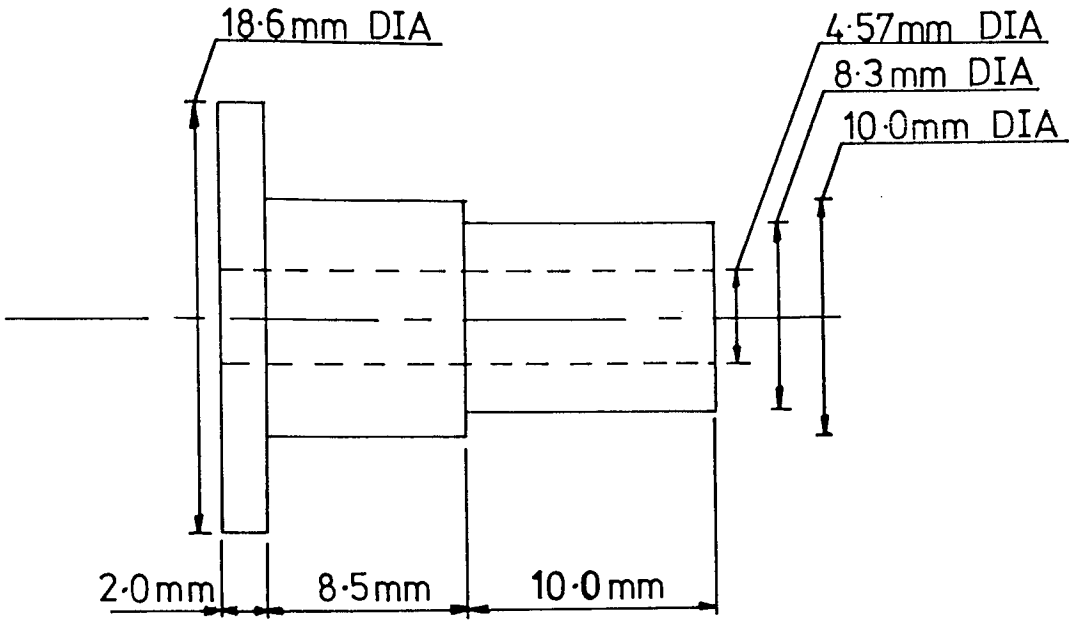

Figure 10.12. The duralumin X-ray limiter shown in Figure 10.11.

pole-piece was 2.25 mm and the field of view of the final projector of the HU 1000 is about 1.4 mm at maximum excitation as determined by the size of the fluorescent screen (120 mm diameter) and the magnification of the projector lens (85X), insertion of the mini-lens did not affect the normal operation of the HU 1000 microscope provided that the bores of these two lenses were approximately concentric. Figure 10.14 shows the field of view of the mini-lens and the final HU 1000 projector lens in the plane of the HU 1000 lens bore (8 mm diameter). It can be seen that the mini-lens must be positioned in the column to an accuracy of ± 0.43 mm for a completely unrestricted field of view to be obtained in the microscope under normal operating conditions.

A preliminary alignment of the mini-lens was made by reducing the excitation and hence magnification

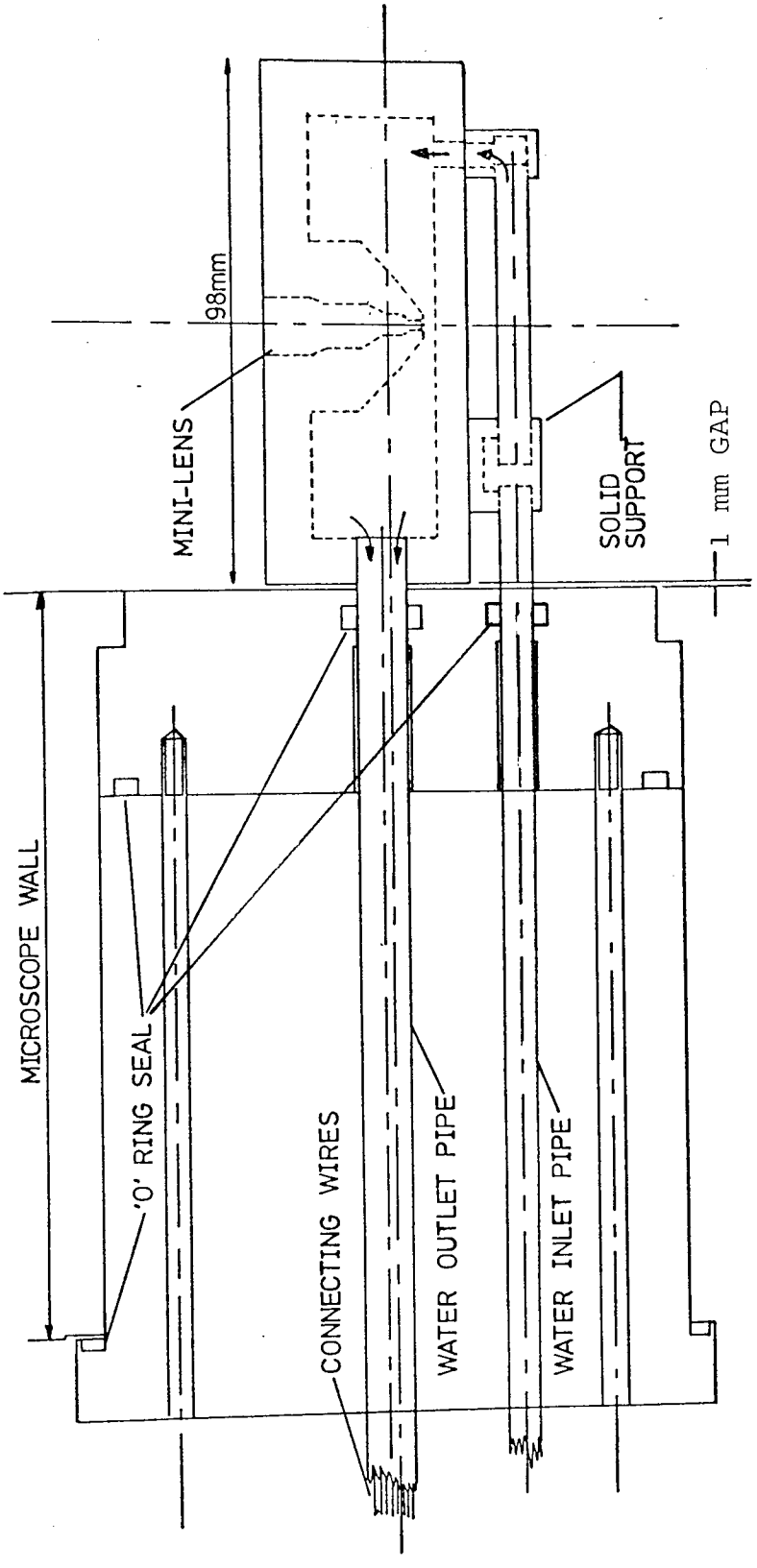

Figure 10.13 Detailed drawing of the arrangement for manipulating and supplying the mini-lens from a single flange in the HU 1000 electron microscope. Connecting wires led out through the water outlet pipe. Radial and transverse movement of the mini-lens ±1 mm.

of the normal projector lens until the bore of the mini-lens came into view slightly off-centre. This was then corrected by the mechanical alignment system of the mini-lens. The mini-lens was then energized and re-centred more critically. It was not possible to correct the alignment completely because the lens could not be tilted under vacuum. Calculations show that the mini-lens would have to be tilted by less than 1.7^{o} with respect to the axis in order to avoid the shadow of the X-ray limiter appearing on the fluorescent screen.

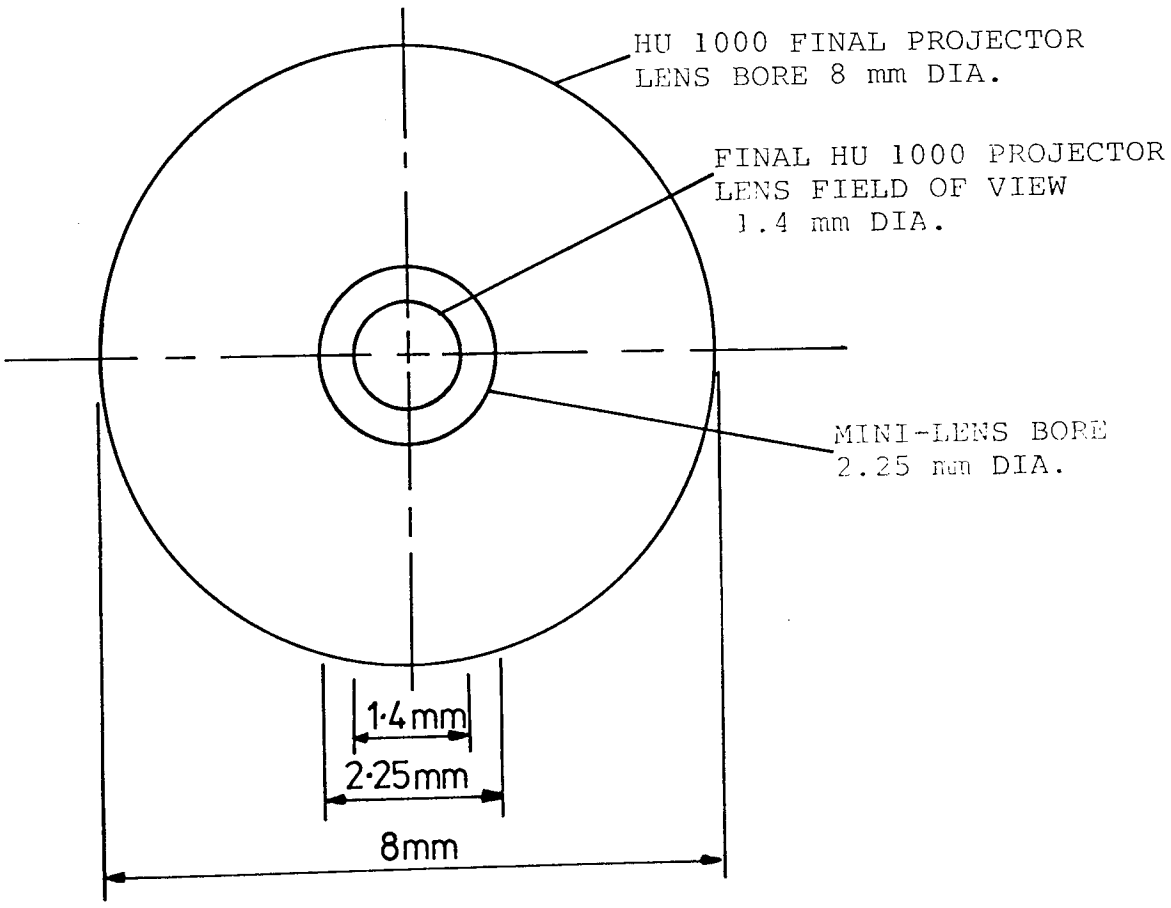

Figure 10.14. Field of view of the final projector lens of the HU 1000 referred to the lens bore (8 mm). The mini-lens must be positioned to within ± 0.4 mm to ensure an unrestricted field of view in normal operation of the microscope.

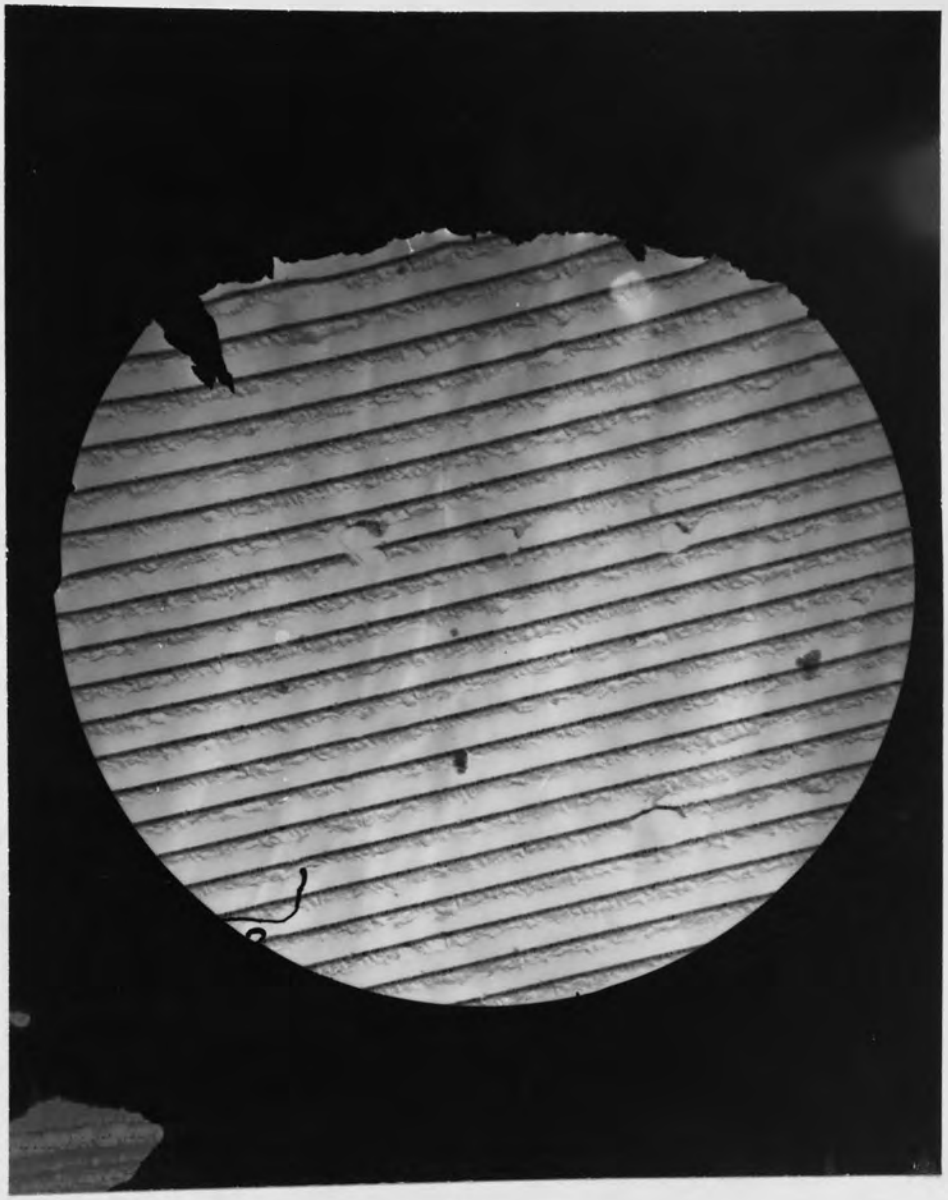

Figure 10.15. Electron micrograph 19 500 X total (4500 X electron optical) of a diffraction grating replica (2160 lines/mm, 0.463 μm spacing) taken at 1 million volts in the HU 1000 using the mini-lens as the final projector lens. The field of view is set by the bore of the final projector (8 mm dia.). Because of a 1.3° tilt, the bore of the mini-lens is just visible in the top of the micrograph. The distortion at this point is about 6.5%.

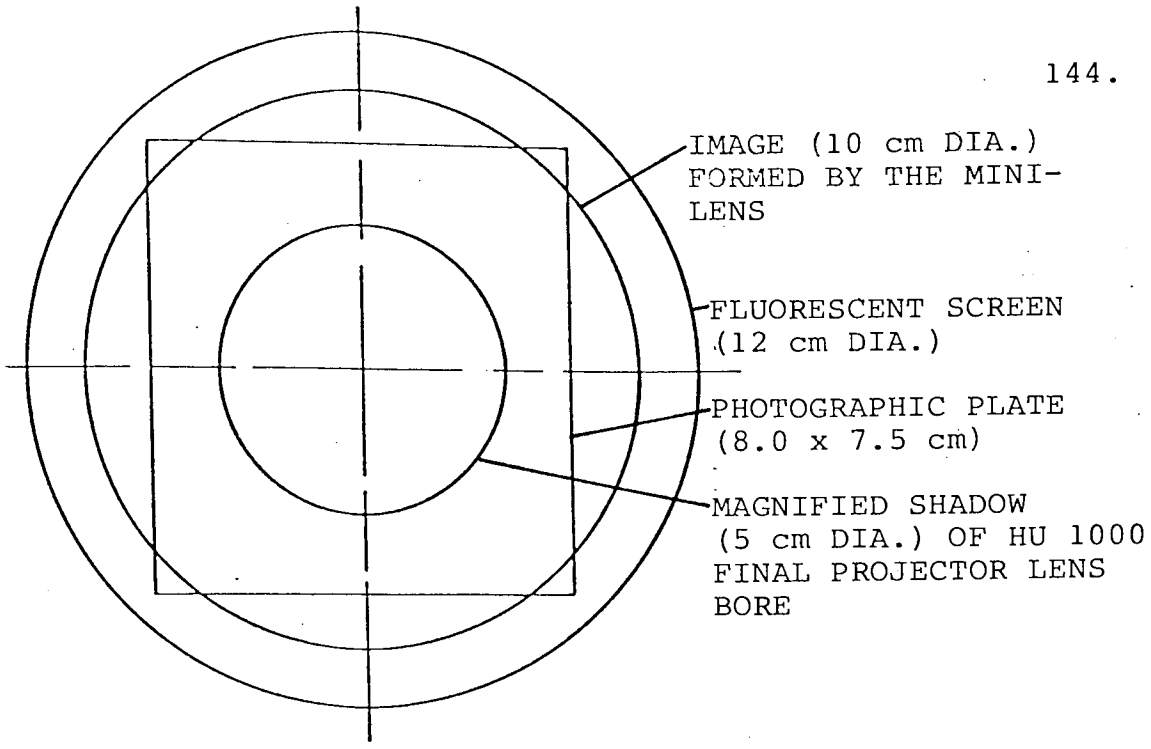

Figure 10.16 (a) The expected image produced on the final screen by the mini-lens in the presence of the normal HU 1000 projector bore, (8 mm dia.). Diameter of the fluorescent screen 120 mm.

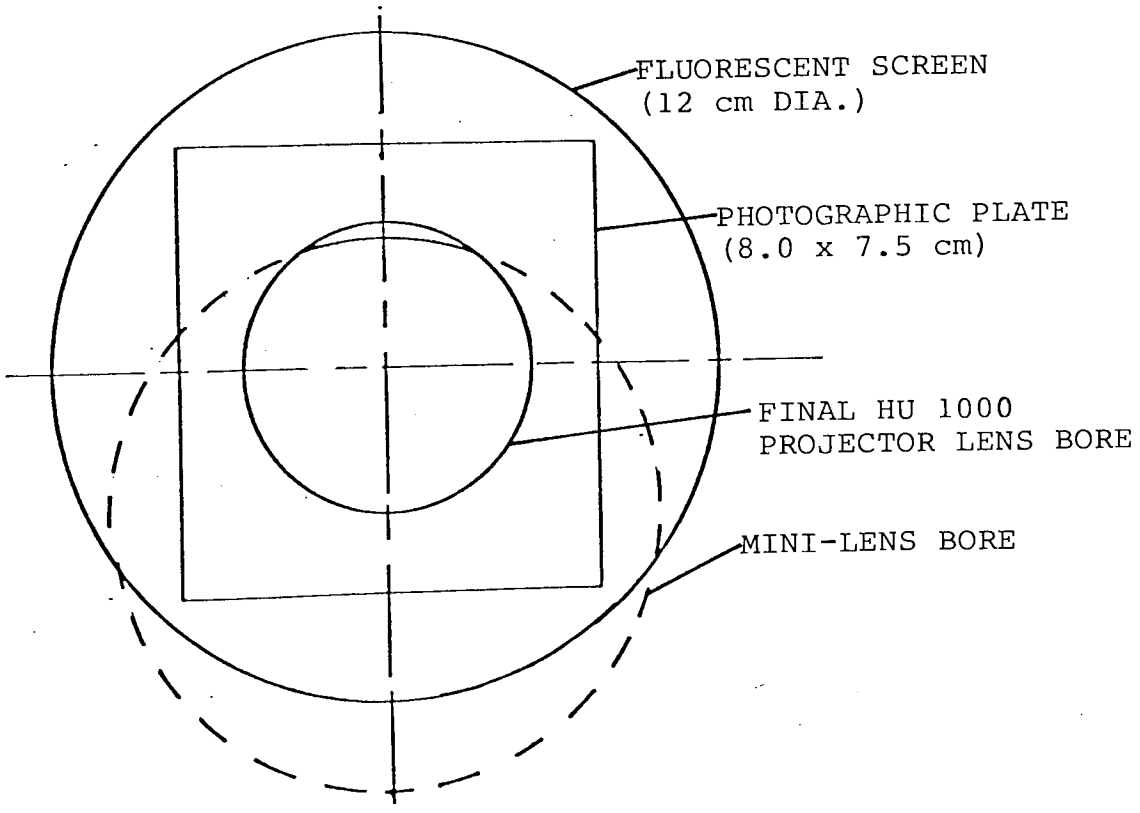

Figure 10.16 (b) Appearance of the image actually produced by tilted mini-lens in the presence of the HU 1000 projector bore. Dashed lines show the part of the image cut off by the bore of the normal projector.

Figure 10.15 shows a micrograph of a diffraction grating replica (spacing 0.463μm) obtained at 1000 kV in the HU 1000 using the normal objective lens and the mini-projector lens. Total magnification 19 500 X (electron-optical magnification 4500 X). The micrograph shows that the degree of tilt was in fact less than the predicted value (1.7^{o}) that would allow the X-ray limiter to be seen. An excitation of some 12 500 A-t was employed in the mini-lens with a power expenditure of 1.8 kW.
an image of the same diffraction grating replica was taken under identical circumstances but by using the normal projector lens of focal length 6.1 mm instead of the mini-projector. Under these circumstances the magnification was found to be 11 250 X. Thus to a first approximation the focal length of the mini-lens equals

$$\frac{11\ 250}{4500} \times 6.1 = 15.3 \text{ mm}.$$

This neglects to take account of the difference in position of the two projector lenses (Figure 10.1). When this is taken into consideration the focal length must be increased by 4%, i.e. $f_p = 15.9$ mm.

Figure 10.16(a) shows the expected field of view under perfect conditions. The mini-lens bore is completely outside the field of view of the final projector lens and completely concentric with it. The rectangular photographic plate (75 x 80 mm) and the final projector lens bore (8 mm dia.) are shown to complete the picture. Figure 10.16(b) indicates what was actually seen in the HU 1000. The mini-lens being tilted caused a portion of the bore to become visible in the field of view. This

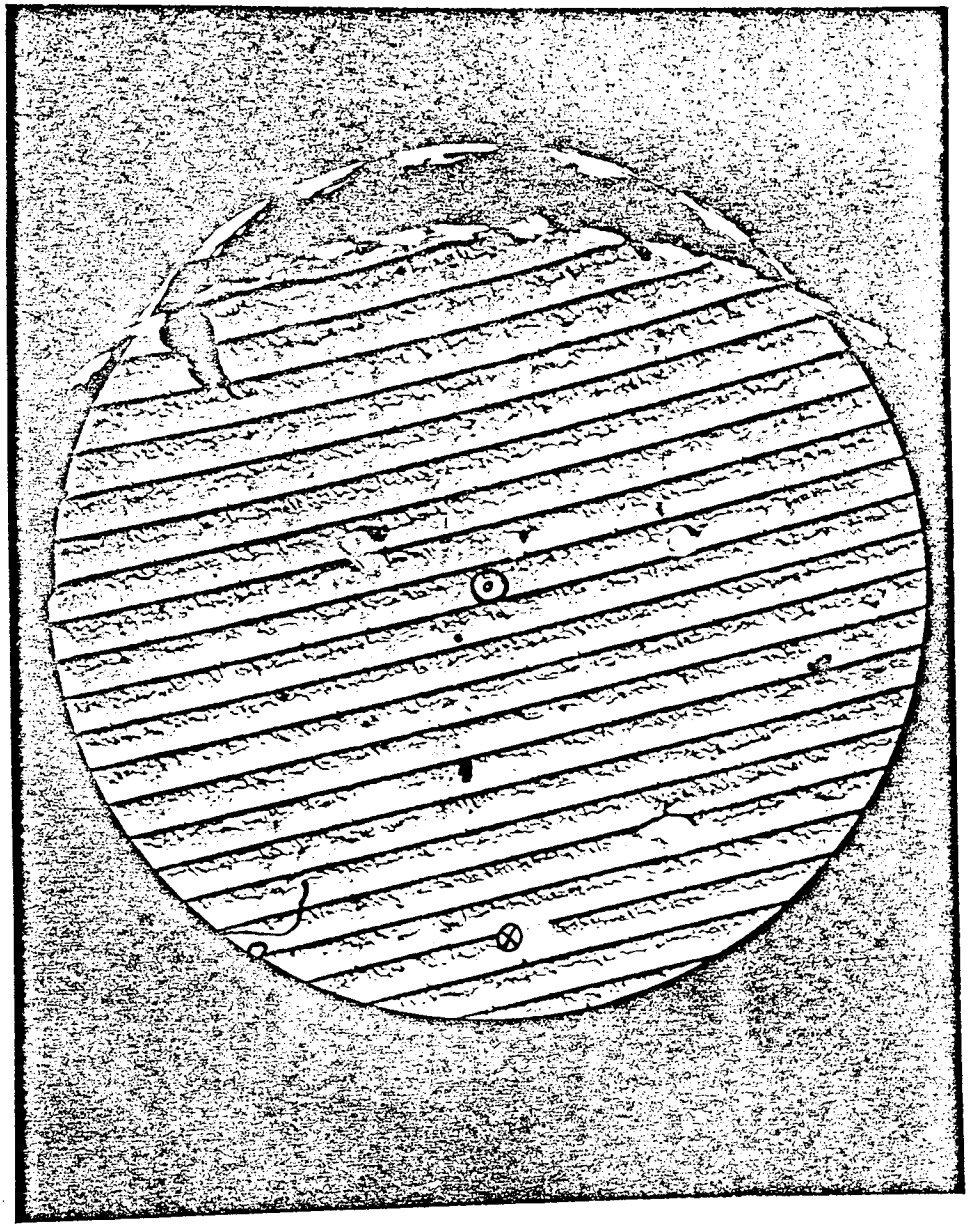

Figure 10.16 (c) Analysis of the micrograph of Figure 10.15. showing the centre of the normal projector ⊙ , the true centre of the projected image of the specimen ⊗ , and the circumference of the mini-lens polepiece (2.25 mm dia.).

is indicated on a copy of the micrograph (Figure 10.15) in Figure 10.16(c). The diameter of the mini-lens bore on the fluorescent screen was 77 mm, i.e. the magnification $M = \frac{77}{2.25} X = 34.4 X$. The projector focal length f_p is given by $f_p = L'/M$ where L' is the distance from the focal point to the screen, approximately 600 mm. From this analysis $f_p = 17.4$ mm. This point is shown on Figure 10.9.

Additional evidence that the limit of the field of view in Figure 10.15 is set by the bore of the normal projector in the HU 1000 is shown in Figure 10.17. Here an initial micrograph taken with the mini-lens tilted through an angle of about 3^{o} with respect to the optical axis of the HU 1000 is superimposed on that of Figure 10.15. The corresponding focal length is twice that of Figure 10.15. This micrograph was taken at a lower excitation of about 9500 A-t. The difference $d\theta$ in rotation equals 22.5^{o} confirming an excitation difference of 3000 A-t between the two micrographs. In spite of this image rotation the boundary of the field of view remains unaltered (notice the slight step in the bore at the extreme left of the figure). Unfortunately the extreme tilt of this micrograph precludes any exact analysis.

We can therefore conclude that the minimum projector focal length of this lens lies between 10 and 11 mm and in its present form is capable of forming an image of 10 cm in diameter in the HU 1000 electron microscope. The measured distortion of 6.6% at an excitation of $NI/V_R^{\frac{1}{2}} = 8.8$ is probably on the high side as it was not possible to align the lens accurately. Calculations (Marai and

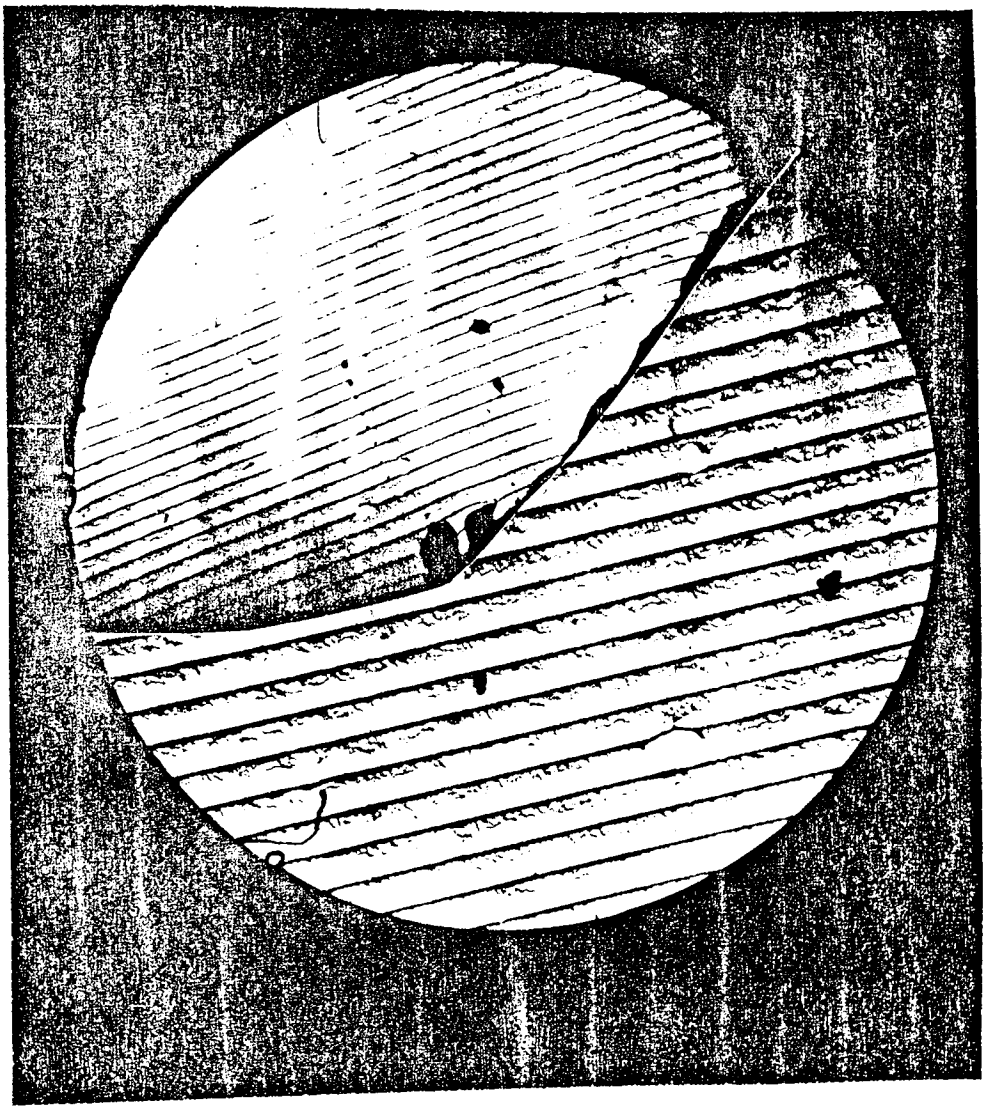

Figure 10.17 A composite micrograph of a grating replica (0.463 μm spacing) taken with a tilted lens (3^{o}) with $NI/V_R^{\frac{1}{2}} = 6.7$ (f = 32 mm) and a well-aligned (better than 1.5^{o}) lens at $NI/V_R^{\frac{1}{2}} = 8.8$ (f = 16 mm) showing the identical limit on field of view as set by the HU 1000 normal polepiece.

Mulvey, 1974) indicate that at minimum focal length the distortion would be less than 1%, and less than 4% at the reduced excitation of $NI/V_R^{\frac{1}{2}} = 8.8$.

Further calculations (Marai and Mulvey, 1976) have shown that there is a preferred direction for the electron trajectory through this lens to obtain low aberrations. If the electron beam enters the gently sloping side of the distribution i.e. is in the opposite direction to the electron trajectory employed here, appreciably lower aberration coefficients can be obtained. To take advantage of this system a redesign of the viewing chamber of the electron microscope would be necessary since with the same image size on the photographic plate the lens-screen distance could be reduced from the normal 535 mm in the HU 1000 to 280 mm for the same distortion on the final screen. This seems an excellent way of bringing about a substantial reduction in column height. To obtain the same total magnification a further mini-lens of magnification 2.5 X would be needed just above the final projector lens, or preferably the whole imaging system could be redesigned to produce the necessary magnification with further shortening of the column height.

10.5 Conclusions

It is possible to produce single-pole lenses of comparable or better performance than that of existing conventional electron lenses. Even by a modest increase in the size of the miniature lens described above a useful reduction in power input could be achieved, while still retaining the essential practical advantages over

existing lenses. It should therefore be feasible to build a one million volt microscope column that is no larger than that of present conventional 100 kV microscopes.

Simple extrapolation of the design of the high voltage mini-lens in the light of the experimental and calculated performance indicates that an increase of lens dimensions of about 40% would be entirely suitable for a conservative design of either a projector or objective lens operating at 1 MV. This would put the weight of the lens up to some 3 kg. It is not necessary, of course, to use single-polepiece lenses; the same general principles of miniaturisation also hold for conventional lenses.

Figure 10.18 shows a design for an improved projector lens. This lens has a pole-face diameter of 4 mm as in the previous lens but the outside diameter of the snout has been increased 40% over the first 10 mm of bore and then by approximately 30% over the remainder of the lens bore. This increase will prevent the iron curcuit from saturating. The depth of the lens has also been increased to 28 mm inside depth. This is to allow a 20% increase in coil width 2w necessary as the power input available was limited. The outside diameter of the lens casing has been increased to accommodate the extra turns required to produce the 21 500 A-t excitation required from the 3 kW power supplies available, to enable the lens to work at its minimum projector focal length.

The final size of the lens has been kept to a minimum consistant with the above considerations. The lens could of course be increased further in size and a reduction in power input obtained. This lens design

indicates that it is possible to have a million volt lens with an obtainable minimum projector focal length of 10 mm, and weighing approximately 3 kg with an outside diameter of 12 cms. Such a lens can act equally well as an objective lens of low spherical aberration and with maximum room for insertion of the specimen. It would therefore be feasible to design an entire electron optical column using mini-lenses of this type for a million volt electron microscope. Table 10.6.1 gives the design parameters for this lens obtained using the method outlined in Chapter 3.

TABLE 10.6.1

THE DESIGN PARAMETERS FOR THE HIGH VOLTAGE LENS SHOWN IN FIGURE 10.18.

Coil No.	1	2	3	4
D_1 (mm)	18.0	32.0	42.0	42.0
D_2 (mm)	104.0	104.0	104.0	104.0
D_m (mm)	61.0	68.0	73.0	73.0
D_2/D_1	5.78	3.25	2.48	2.48
D_2-D_1 (mm)	86.0	72.0	62.0	62.0
2w (mm)	6.0	6.0	6.0	6.0
W (Watts)	1100.0	1100.0	400.0	400.0
NI_{opt} (A-t)	6800	5780	3200	3200
d_{opt} (mm)	0.89	0.89	1.1	1.1

Power supply 3 kW (2 units of 25 Amps at 60 Volts).

NI = 19 000 A-t $f_p = 1.01\ f_{pmin.}$

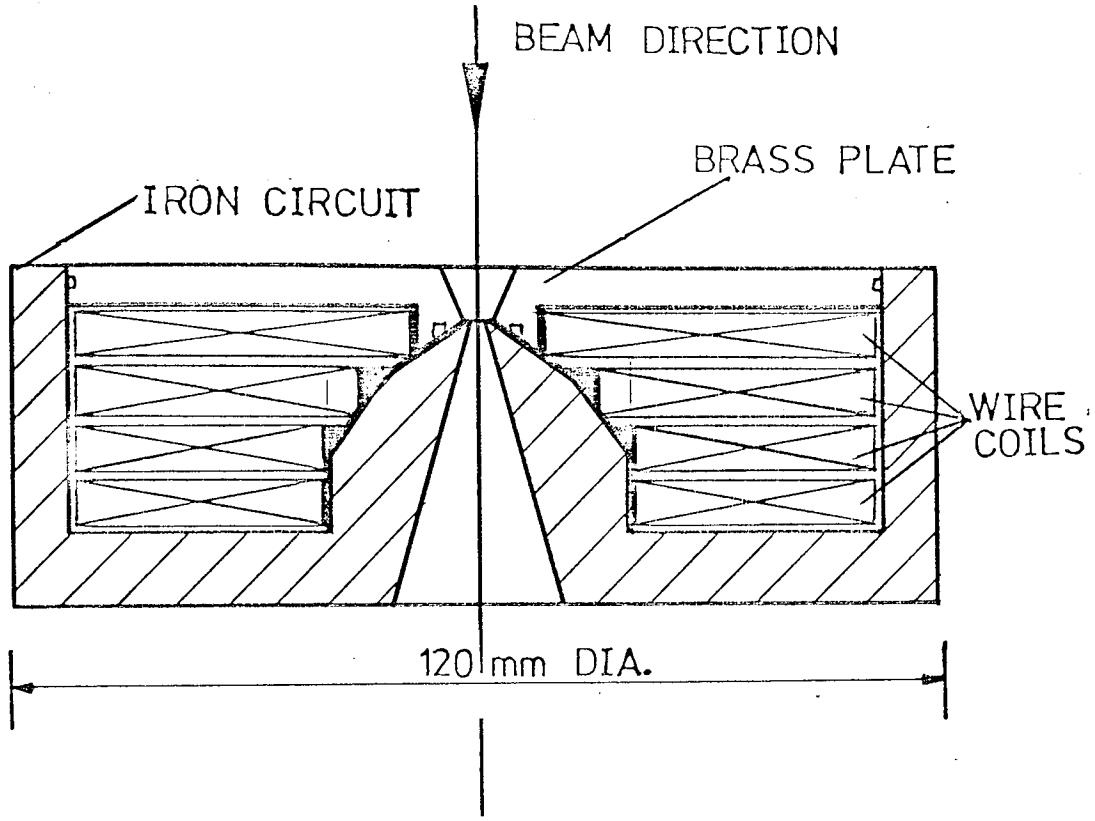

Figure 10.18 Proposed improved design for a 1 MV lens. Focal length ≈ 10 mm, excitation 19 000 A-t, power input 3 kW, and weight 3 kg.

The straightforward design methods and the ease of manufacture produce reliable magnetic electron lenses that give a method of achieving large improvements in the design of electron optical instruments. It has been shown that the techniques developed to miniaturise magnetic electron lenses are feasible and that these lenses can be used in every branch of electron microscopy, TEM, SEM, STEM, and HVEM.

11. REFERENCES

Basset, R. and Mulvey, T. Proc. 5th Int. Conf. X-ray Optics and Microanalysis, Trübringen (Springer) pp 224-230, 1968.

Basset, R. and Mulvey, T. Z. für Physik, pp 142-145, 27th March, 1969.

Cooke, C. J. and Duncumb, P. Proc. 5th Int. Conf. X-ray Optics and Microanalysis, Tübringen (Springer) pp 245-247, 1968.

Cooke, C. J. and Openshaw, I. K. Proc. 7th Int. Conf. Elec. Microscopy, Grenoble (Soc. Francaise de Micros. Electronique Paris) 1, pp 170-176, 1970.

Crewe, A. V. Quat. Rev. of Biophys. 3, 1, pp 137-175, 1970.

Eckert, E. R. G. and Gross, J. F. Heat and Mass Transfer, McGraw-Hill, pp 43-45, 1963.

Farrant, J. L. Proc. 25th Anniv. Mtng. of EMAG, Inst. of Phys. pp 141-142, 1971.

Fontijn, L. A., Bok, A. B. and Kornet, J. G. Inst. of App. Phys. Special Publication TNO-TH Delft 1968.

Glaser, W. Z. für Phys. 97, pp 177-201, 1935.

Glaser, W. Grundlagen der Elektronenoptik, Vienna, Springer, pp 306-307, 1952.

Grivet, P. Electron Optics Part I Oxford. Pergamon Press, Chapter 9 p 216, 1972.

Juma, S. M. and Mulvey, T. Proc. 8th Int. Cong. Electron Microscopy, Canberra 1, pp 134-135, 1974.

Kays, W. M. and London, A. L. Compact Heat Exchangers, New York, McGraw-Hill 1964.

Kimura, H. and Tamura, H. I.E.E.E. Proc. 9th Annual Sympos. Electron, Ion and Laser Beam technology pp 198-205, 1967.

Klemperer, O. Electron Optics. Camb. Univ. Press Ch 5, 1971

Knoll, M. and Ruska, E. Contribution to Geometrical Optics Annls. Phys. 12, p 607, 1932.

Knudsen, J. G. and Katz, D. L. Fluid Dynamics and Heat Transfer, New York, McGraw-Hill,1954.

Koike, H., Ueno, K.? and Suzuki, M. EMSA Proc. p 28, 1971

Kroon, D. J. Laboratory Magnets, Cleaver-Hume Press Ltd., London, Ch 8, Sect. 2 1968.

LePoole, J. B. 3rd Conf. Elect. Micros., Prague, Czech Acad. of Sci. supplementary pages, 1964.

Liebmann, G. Proc. Phys. Soc. 62, 12, Dec. 1949.

Liebmann, G. Phil. Mag., Ser. 7. vol. xli, p 1143, Nov 1950

Liebmann, G. and Grad, E. M. Proc. Phys. Soc. B, vol. lxiv, p 956, 1951.

Machlachlan, M. E. C. Proc. Conf. Scann. Elec. Micros. London, Inst. of Phys. pp 46-49, 1973.

Marai, F. Z. and Mulvey, T. 8th Int. Cong. on Elect. Micros., Canberra, vol. 1, pp 130-131, 1974.

Maria F. Z. and Mulvey, T. Developments in Electron Microscopy and Analysis, ed. J. Venables. Academic Press, pp 43-44, 1976.

McAdams, W. H. Heat Transmission, McGraw-Hill, New York, p 219, 1933.

Montgomery, D. B. Solenoid Magnet Design, Wiley-Interscience, New York, p 37, 1969.

Mulvey, T. and Wallington, M. J. J. Sci. Instru. Ser. 2, vol. 2, 1969.

Mulvey, T. and Newman C. D. Proc. 5th Eur. Conf. Elect. Micros., London, Inst. of Phys. pp 116-117, 1972

Mulvey, T. and Newman, C. D. Proc. Conf. Scann. Micros., London, Inst. of Phys. pp 16-21, 1973.

Mulvey, T. and Newman, C. D. Proc. 3rd Int. Conf. High Voltage Elect. Micros., Ed. Swann, P. R., Humphreys, C. J. and Goringe, M. J., Academic Press, London, p 98-102, 1973b.

Mulvey, T. 8th Int. Conf. on Elect. Micros., Canberra, vol. 1, pp 16-17, 1974.

Munro, E. Ph. D. Thesis, Cambridge Univ. 1971.

Newman, M. J., Trowbridge, C. W. and Turner, L. R. Proc. 4th Int. Conf. on Magnet Technology, Brookhaven 1972.

Pease, R. F. W. and Nixon, W. C. High Res. Scann. Elect. Micros., Proc. 27th Ann. Mtg. EMSA p 86, 1969.

Smith, K. C. A. and Oatley, C. W. The Scanning Electron Microscope and its Field of Applications, Br. J. Appl. Phys. 6, 391, 1955.

Taylor, A. J. Electrical Times, 6th January, 1972.

Thon, F. Siemans Review,3rd special issue,36, p24, 1969

APPENDIX 1

Versatile Miniature Electron Lenses.

A paper presented by T. Mulvey and C. D. Newman at the Fifth European Congress on Electron Microscopy at Manchester in 1972.

Aston University

Content has been removed for copyright reasons

Aston University

Content has been removed for copyright reasons

APPENDIX 2

New Electron-Optical Systems for SEM and STEM. A paper presented by T. Mulvey and C. D. Newman at the conference on Scanning Electron Microscopy organised by the Institute of Physics and held at Newcastle in 1973.

Aston University

Content has been removed for copyright reasons

Aston University

Content has been removed for copyright reasons

APPENDIX 3

New Experimental Lens Designs for High Voltage Electron Microscopy.
A paper presented by T. Mulvey and C. D. Newman at the 3rd International Conference on High Voltage Electron Microscopy, held at Oxford in 1973.

Aston University

Content has been removed for copyright reasons

Aston University

Content has been removed for copyright reasons

APPENDIX 4.

Calculation of the axial flux density distribution of iron free coils.

Axial Flux Density Distribution of a Coil of Rectangular Cross Section.

The axial flux density B_z for an elemental current carrying ring at a point P on the axis of the ring (see Figure A4.1) is given by

$$B_z=\mu_0.I.r.\text{Sin } A /(2.a^2) \qquad \text{.....A4.1}$$

where r = radius of the ring
a = distance of P to the ring
A = the angle the ring makes with the axis at P
I = current in the ring
μ_0 = permeability of free space

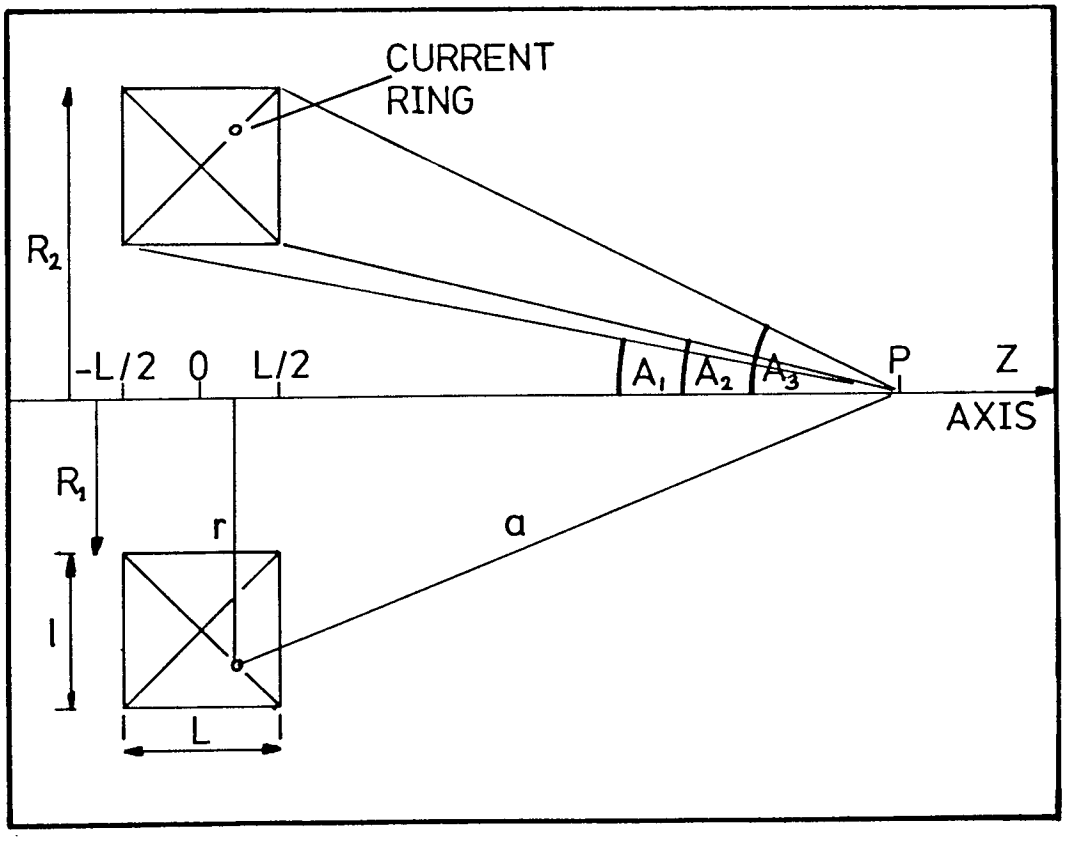

Figure A4.1 Current carrying coil of rectangular cross section.

Integrating equation A4.1 in the z direction gives the flux density due to an elemental solenoid.

$$B_z = \int (\mu_0 . r . \sin A . I' / (2.a^2)) . dz \quad \ldots\ldots A4.2$$

between the limits $z = \pm L/2$.

where $I' = N.I/L$

and

N = number of turns in the solenoid

I = current through the solenoid

L = length of the solenoid

$$B_z = \mu_0 . N . I . (\cos A_2 - \cos A_1)/(2.L) \quad \ldots\ldots A4.3$$

Integrating equation A4.3 in the radial direction gives the axial flux density at the point P due to the whole coil.

$$B_z = \int \mu_0 . I' . (\cos A_2 - \cos A_1) . dr/2 \quad \ldots\ldots A4.4$$

between the limits $r = R_1$ and R_2.

where $I' = I.N/(L.l)$

and

l = radial extent of the coil

Using the relationships

$$\cos A_1 = (z-(L/2))/(r^2+(z+(L/2))^2)^{\frac{1}{2}}$$

$$\cos A_2 = (z+(L/2))/(r^2+(z+(L/2))^2)^{\frac{1}{2}}$$

and the substitutions

$$\tan B = r/(z+(L/2))$$

$$\tan B' = r/(z-(L/2))$$

The axial flux density from the whole coil as a function of z is

$$B_z = ((\mu_0 . I . N/(2.L.l)) (G^- + G^+) \quad \ldots\ldots A4.5$$

where

$$G^- = ((L/2)-z) . \ln \frac{R_2+(R_2^2+(z-(L/2))^2)^{\frac{1}{2}}}{R_1+(R_1^2+(z-(L/2))^2)^{\frac{1}{2}}}$$

$$G^+ = ((L/2)+z) . \ln \frac{R_2+(R_2^2+(z+(L/2))^2)^{\frac{1}{2}}}{R_1+(R^2+(z+(L/2))^2)^{\frac{1}{2}}}$$

The axial flux density distribution from an infinitely thin coil.

The expression for an elemental ring can be integrated in a radial direction to give an expression for the axial flux density due to an elemental disc. The expression obtained is a good approximation for the pancake lens, where the axial extent is much less than the radial extent.

$$B_z = \int \mu_o . r . \sin A . I' / (2.a^2) . dr \qquad .....A4.6$$

Using the relationships

$$\sin A = r/a$$

where $a = (r^2+z^2)^{\frac{1}{2}}$

and the substitution $\tan B = r/z$

and integrating A4.6 between the limits R_1 and R_2 gives

$$B_z = \mu_o . I . N/(2.l) . (\sin A_1 - \sin A_3 + \ln G)$$

where G $G = ((1+\sin A_3).\cos A_1)/((1+\sin A_1).\cos A_3)$

and l = radial extent of the coil

B_z may be defined entirely in terms of sines by using the relationship

$$(\cos A_1)/(\cos A_2) = (R_2 . \sin A_1)/(R_1 \sin A_2)$$

APPENDIX 5

Listings of the computer programs "FLUXBZ" and "FLUTRAG" used in this thesis.

"FLUXBZ"

```
24/03/72          COMPILED BY XALE MK.  5C

'SEND TO' ( ED,ASTD-DEFAULT(0),,PROGRAM)
'WORK' (ED,WORK FILE   (0))
'LIBRARY'(ED,SUBGROUPSRF7)
'LIBRARY' (ED,SUBGROUPFSCF)
'TRACE'2
'BEGIN'
'PROCEDURE' HGPLOT (X,Y,A,B);
'VALUE'X,Y,A,B;
'REAL'X,Y;
'INTEGER'A,B;
'EXTERNAL'     ;
'PROCEDURE' STRARR(A,N,S);
'ARRAY'A;
'INTEGER'N;
'STRING'S;
'EXTERNAL'     ;
'PROCEDURE' OPENPLOT;
'EXTERNAL';
'PROCEDURE' CLOSEPLOT;
'EXTERNAL';
OPENPLOT;
'BEGIN' 'COMMENT' THIS PROGRAM CALCULATES THE AXIAL FIELD DISTRIBUTION
FOR THE LENS FORMULA
'REAL' Z, BZ, D1,D2,L,I,W,A,B,C,D,E,F,G,ALPHA,BETA,ZM,MUO:
'REAL'PP,QQ,GG;
'REAL' GPY;
        'INTEGER' N;
'INTEGER'JNO,GN;
'ARRAY'RZ1,RZ2,RZ3,RZ4,RZ5,BZ1,BZ2,BZ3,BZ4,BZ5[1:100]:
'ARRAY'RB,RZ[1:97],LAB[1:10],LBY,LBX[1:2]:
'PROCEDURE'  HGPRECT(X,Y,H,W,TH,I);
'VALUE'X,Y,H,W,TH,I:
'INTEGER'I:
'REAL'X,Y,H,W,TH;
'EXTERNAL';
   'PROCEDURE' HGPNUMBER (X,Y,HT,FL,THETA,I,IP,IQ);
               'VALUE'X,Y,HT,FL,THETA,I,IP,IQ:
               'INTEGER'I,IP,IQ;
               'REAL'X,Y,HT,FL,THETA;
               'EXTERNAL';
'PROCEDURE' HGPAXISV (X,Y,BCD,NC,S,THETA,XMIN,DX,GAP,NH):
'VALUE'X,Y,NC,S,THETA,XMIN,DX,GAP,NH;
'INTEGER'NC,NH;
'ARRAY'BCD;
'REAL'X,Y,S,THETA,XMIN,DX,GAP;
               'EXTERNAL';
   'PROCEDURE' HGPSYMBL (X,Y,HT,BCD,THETA,N);
               'VALUE'X,Y,HT,THETA,N;
               'INTEGER'N;
               'ARRAY'BCD;
               'REAL'X,Y,HT,THETA;
               'EXTERNAL';
'PROCEDURE' HGPSCURVE(X,Y,N,L,YOP,YFP);
               'VALUE'N,L,YOP,YFP;
               'INTEGER'N,L;
               'ARRAY'X,Y;
               'REAL'YOP,YFP;
```

```
                'EXTERNAL';
JNO:=READ  ;
MU0:=1.256636'10'-6;
PP:=-7;
QQ:=8.5;
GG:=0;
GN:=0;
REPEAT:GN:=GN+1;
D1:=READ;
D2:=READ;
L:=READ ;
W:=READ;
I:=READ ;
WRITE TEXT('(''('5S')'SI%UNITS%ARE%USED%THROUGHOUT')');
NEWLINE(2);
WRITE TEXT('(''('5S')'THE%PARAMETERS%FOR%THIS%LENS%ARE%'('2C')'')');
WRITE TEXT('('D1')');
PRINT(D1,1,3);
WRITE TEXT('('D2')');
PRINT(D2,2,4);
WRITE TEXT('('L')');
PRINT(L,3,3);
WRITE TEXT('('I')');
PRINT(I,2,1);
WRITE TEXT('('W')');
PRINT(W,3,1);
WRITE TEXT('('MU0')');
PRINT(MU0,1,6);
NEWLINE(5);
WRITE TEXT('(''('5S')'THE%AXIAL%FIELD%DISTRIBUTION'('3C')'')');
WRITE TEXT('(''('10S')'Z'('10S')'BZ'('2C')'')');
ALPHA:=D2/D1;
BETA:=L/D1;
G:=MU0*I*W/(2*D1*BETA*(ALPHA-1));
                N:=0;
'FOR'Z:=-0.1'STEP'0.005'UNTIL'-0.01,-0.009'STEP'0.001'UNTIL'0.009,0.01
'STEP'0.005'UNTIL'0.1'DO'
'BEGIN'
        N:=N+1;
ZM:=Z*Z/D1;
A:=SQRT(ALPHA↑2+(BETA-ZM)↑2)      ;
B:=SQRT(1+(BETA-ZM)↑2)  ;
C:=SQRT(ALPHA↑2+(BETA+ZM)↑2);
D:=SQRT(1+(BETA+ZM)↑2)    ;
E:=(BETA-ZM)*LN((ALPHA+A)/(1+B));
F:=(BETA+ZM)*LN((ALPHA+C)/(1+D));
BZ:=(E+F)*G;
RZ[N]:=Z+50;
RB[N]:=BZ*10000/(80*G);
SPACE(8);
PRINT(Z,3,4);
SPACE(3);
PRINT(BZ,6,5);
NEWLINE(1);
'END';
GPY:=READ;
NEWLINE(10);
HGPLOT(PP,QQ,0,4);
STRARR(LAB,22,'('THE%AXIAL%FLUX%DENSITY')');
STRARR(LBX,16,'('Z%OVER%DINTERNAL')');
```

```
      STRARR(LBY,7,'('FLUXXBZ')');
HGPSYMBL(-2.25,7.25,0.2,LAB,0,22);
HGPAXISV(-5.0,LBX,-11,10,0,-10,1,0.5,-2);
HGPAXISV(0,0,LBY,7,7,90,0.4,1,-2);
HGPRECT(5.25,-0.5,10.5,8,90,3);
HGPSCURVE(RZ,RB,57,0,1,1);
HGPLOT(0,0,3,0);
GG:=GG+1;
'IF'GG'LT'2.9'THEN'
'BEGIN'
PP:=0;
QQ:=9;
'END'
'ELSE'
'BEGIN'
PP:=PP-12;
GG:=0;
QQ:=-18;
BBB:'END';
'IF'GN'LT'(JNO-0.1)'THEN''GOTO'REPEAT;
'END';
CLOSEPLOT;
'END';
```

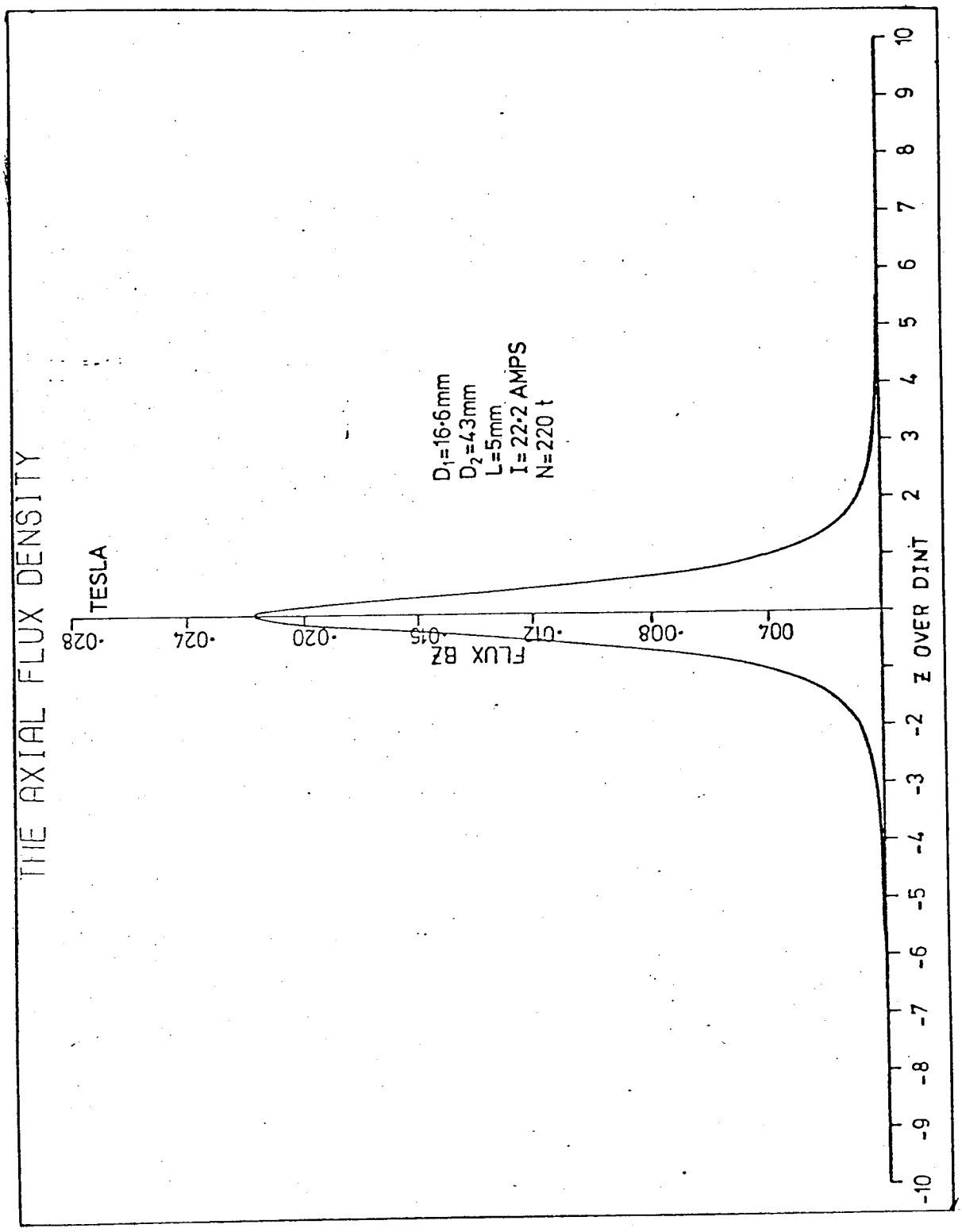
THE AXIAL FLUX DENSITY
TESLA
.028
.024
.020
.016
.012
.008
.004
FLUX BZ
D_1=16·6mm
D_2=43mm
L=5mm
I= 22·2 AMPS
N=220 t
-10 -9 -8 -7 -6 -5 -4 -3 -2
1 2 3 4 5 6 7 8 9 10
Z OVER DINT

"FLUTRAG"

```
22/04/72          COMPILED BY XALE MK. 5C

'SEND TO' ( ED,ASTD-DEFAULT(0),,PROGRAM)
'WORK' (ED,WORK FILE    (0))
'LIBRARY'(ED,SUBGROUPSRF7)
'LIBRARY' (ED,SUBGROUPFSCE)
'TRACE'2
'BEGIN'
'PROCEDURE' HGPLOT (X,Y,A,B);
'VALUE'X,Y,A,B;
'REAL'X,Y;
'INTEGER'A,B;
'EXTERNAL'    ;
'PROCEDURE' STRARR(A,N,S);
'ARRAY'A;
'INTEGER'N;
'STRING'S;
'EXTERNAL'    ;
'PROCEDURE' OPENPLOT;
'EXTERNAL';
'PROCEDURE' CLOSEPLOT;
'EXTERNAL';
OPENPLOT;
'BEGIN'
'COMMENT' THIS IS THE FIRST ATTEMPT TO CONSTRUCT A FIELD AND
TRAJECTORY SOLVING PROGRAM

'COMMENT'THIS PROGRAM USES THE ARIMET IC MEAN OF THE FLUX
BETWEEN THE TWO Z INTERVALS;
'COMMENT'TRAJECT SOLVES THE ELECTRON PATH THROUGH A STAIRCASE
MAGNETIC FIELD;
'COMMENT'THE DATA CARD FORMAT IS D1,D2,L,I,W,MU0      ;
'REAL' Z, BZ, D1,D2,L,I,W,A,B,C,D,E,F,G,ALPHA,BETA,ZM,MU0;
'REAL'T;
'INTEGER'P;
'ARRAY'RZ,RB,RT[1:100],LY,LX[1:10];
'INTEGER'Q;
      'ARRAY'BZTRAJ,ZTRAJ,BZMEAN[1:100];
'PROCEDURE'  HGPRECT(X,Y,H,W,TH,I);
'VALUE'X,Y,H,W,TH,I;
'INTEGER'I;
'REAL'X,Y,H,W,TH;
'EXTERNAL';
'PROCEDURE' HGPLINE(X,Y,N,K);
'VALUE' N,K;
'ARRAY'X,Y;
'INTEGER'N,K;
'EXTERNAL';
   'PROCEDURE' HGPNUMBER (X,Y,HT,FL,THETA,I,IP,IQ);
               'VALUE'X,Y,HT,FL,THETA,I,IP,IQ;
               'INTEGER'I,IP,IQ;
               'REAL'X,Y,HT,FL,THETA;
               'EXTERNAL';
'PROCEDURE' HGPAXISV (X,Y,BCD,NC,S,THETA,XMIN,DX,GAP,NH);
'VALUE'X,Y,NC,S,THETA,XMIN,DX,GAP,NH;
'INTEGER'NC,NH;
'ARRAY'BCD;
'REAL'X,Y,S,THETA,XMIN,DX,GAP;
```

```
                'EXTERNAL';
                'INTEGER'N;
                'ARRAY'BCD;

                'REAL'X,Y,HT,THETA;
                'EXTERNAL';

'PROCEDURE' HGPSCURVE(X,Y,N,L,YOP,YFP);

                'VALUE'N,L,YOP,YFP;

                'INTEGER'N,L;

                'ARRAY'X,Y;

                'REAL'YOP,YFP;

                'EXTERNAL';

D1:=READ;
D2:=READ;
L:=READ;
I:=READ ;
W:=READ;
MU0:=READ;
WRITE TEXT('('('5S')'THE%PARAMETERS%FOR%THIS%LENS%ARE%'('2C')')');
WRITE TEXT('('D1=')');
PRINT(D1,1,1);
NEWLINE(2);
WRITE TEXT('(' D2=')');
PRINT(D2,2,1);
NEWLINE(2);
WRITE TEXT('('L=')');
PRINT(L,1,1);
NEWLINE(2);
WRITE TEXT('('I=')');
PRINT(I,2,1);
NEWLINE(2);
WRITE TEXT('('W=')');
PRINT(W,3,1);
NEWLINE(2);
WRITE TEXT('('MU0=')');
PRINT(MU0,1,6);
WRITE TEXT('('ZM%IS%THE%AXIAL%DISTAN CE%DEVIDED%BY%HALF%THE%INNER%
          DIAMETER')');
PAPER THROW;
WRITE TEXT('('IW%IS%THE%EXCITATION%OF%THE%LENS%IN%AMPERE-TURNS')');
WRITE TEXT('('D1,D2,%AND%L%ARE%IN%CMS')');
NEWLINE(5);
WRITE TEXT('('('5S')'BZ%IS%IN%GAUSS')');
NEWLINE(2);
ALPHA:=D2/D1;
WRITE TEXT('('D2/D1=')');
PRINT(ALPHA,2,6);
NEWLINE(10);
WRITE TEXT('('L=')');
PRINT(L,1,6);
NEWLINE(5);
WRITE TEXT('('('12S')'Z'('14S')'BZ'('24S')'ZM'('2C')')');
WRITE TEXT('('('5S')'THE%AXIAL%FIELD%DISTRIBUTION'('3C')')');
```

```
BETA:=L/D1;
P:=0;
G:=MU0*I*V/(2*D1*BETA*(ALPHA-1));
'FOR'Z:=-20'STEP'0.5'UNTIL'-1,-0.9'STEP'0.1'UNTIL'0.9,1'STEP'
0.5'UNTIL'20'DO'
'BEGIN'
P:=P+1;
ZM:=Z+2/D1;
A:=SQRT(ALPHA↑2+(BETA-ZM)↑2)      ;
B:=SQRT(1+(BETA-ZM)↑2) ;
C:=SQRT(ALPHA↑2+(BETA+ZM)↑2);
D:=SQRT(1+(BETA+ZM)↑2)    ;
E:=(BETA-ZM)*LN((ALPHA+A)/(1+B));
F:=(BETA+ZM)*LN((ALPHA+C)/(1+D));
BZ:=(E+F)*G;
SPACE(8);
PRINT(Z,3,1);
SPACE(3);
PRINT(BZ,6,5);
SPACE(11);
PRINT(ZM,3,4);
BZTRAJ[P]:=BZ;
RB[P]:=(BZ/400);
ZTRAJ[P]:=Z;
RZ[P]:=Z/4;
NEWLINE(1);
'END'   ;
PAPER THROW;
'BEGIN'
'REAL'V,RO,RODASH;
'ARRAY' BM[1:100];
'ARRAY'  Z[1:100];
'REAL'R,RDASH,CON;
'INTEGER'N,K,Y;
RO:=READ;
RODASH:=READ;
V:=READ;
NEWLINE(1);
WRITE TEXT('('R=')');
PRINT(RO,4,8);
WRITE TEXT('('RDASH=')');
PRINT(RODASH,4,8);
NEWLINE(1);
              Y:=0;
K:=0;
N:=0;
NEWLINE(3);
CON:=SQRT((1.6'10'-19)/((9.1'10'-31)*8*V));
WRITE TEXT('('CON=')');
PRINT(CON,8,8);
NEWLINE(5);
WRITE TEXT('('Z%IS%IN%METRES')');
WRITE TEXT('('BM%AND%CON%ARE%IN%SI%UNITS')');
WRITE TEXT('('('('8S')'BM'('12S')'Z'('2C')'')');
'FOR'K:=1'STEP'1'UNTIL'95'DO'
'BEGIN'
BM[K]:=CON*(BZTRAJ[K]+BZTRAJ[K+1])/2'10'4;
Z[K]:=(ZTRAJ[K+1]-ZTRAJ[K])/100;
PRINT(BM[K],2,7);
SPACE(3);
```

```
PRINT(Z[K],3,5);
NEWLINE(1);
'END';
PAPER THROW;
Q:=0;
WRITE TEXT('('('45')'Z'('13S')'BM'('12S')'R'('12S')'RDASH'('2C')')');
'FOR'Y:=1'STEP'1'UNTIL'94'DO'
'BEGIN'
Q:=Q+1;
T:=BM[Y]*Z[Y];
NEWLINE(1);
R:=R0*COS(T)+(RODASH*SIN(T))/BM[Y];
RT[Q]:=R;
RDASH:=-R0*BM[Y]*SIN(T)+RODASH*COS(T);
R0:=R;
RODASH:=RDASH;
PRINT(Z[Y],5,5);
SPACE(3);
PRINT(BM[Y],5,5);
SPACE(6);
PRINT(R,1,8);
SPACE(3);
PRINT(RDASH,3,8);
SPACE(5);
PRINT(ZTRAJ[1+Y],4,4);
NEWLINE(1);
'END';
        'END';
'BEGIN'
        'ARRAY' RX[1:Q];
         'REAL' QX;
        'FOR'QX:=1'STEP'1'UNTIL'Q'DO'
            'BEGIN'
            RX[QX]:=RZ[QX];
PRINT(RX[QX],2,2);
NEWLINE(1);
            'END'     ;
HGPLOT(-5,20,0,4);
HGPSCURVE(RZ,-3,97,0,1,1);
HGPLINE(RX,RT,Q,1);
      STRARR(LBY,7,'('FLUX%BZ')');
STRARR(LBX,16,'('Z%OVER%INTERNAL')');
STRARR(LAB,22,'('THE%AXIAL%FLUX%DENSITY')');
HGPSYMBL(-2.25,7.25,0.2,LAB,0,22);
HGPAXISV(-5,0,LBX,-11,10,0,-10,1,0.5,-2);
HGPRECT(5.25,-0.5,10.5,8.90,3);
HGPAXISV(0,0,LBY,7,7,90,0,4,1,-2);
'END'
LLL:'END';
CLOSEPLOT;
'END';
```

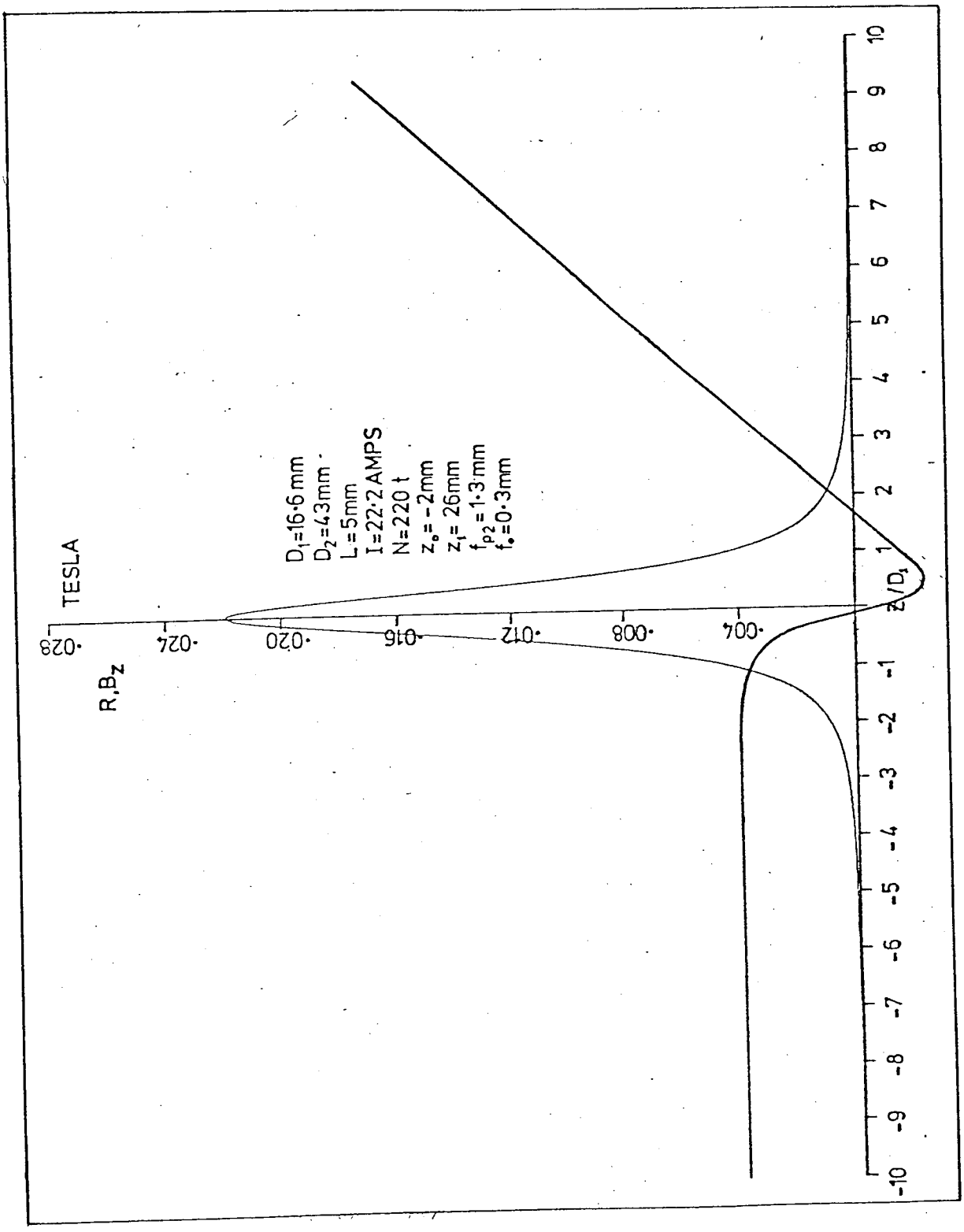
TESLA
R,Bz
.028
.024
.020
.016
.012
.008
.004
D1=16·6mm
D2=43mm
L=5mm
I=22·2AMPS
N=220 t
z0=-2mm
z1=26mm
fp2=1·3mm
f0=0·3mm
z/D1
10
9
8
7
6
5
4
3
2
1
-1
-2
-3
-4
-5
-6
-7
-8
-9
-10

APPENDIX 6

The method used to determine the proportion of back scattered electrons incident on the secondary electron collector.

Assume the back scattered electrons are distributed as in Lambert's cosine law.

Define I as the intensity of the back scattered electrons in the normal direction per unit surface area per unit solid angle from a small surface dS within a small cone of solid angle dw, with the normal as axis, see figure A6.1.

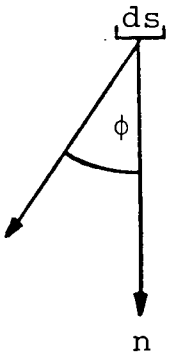

Figure A6.1

Hence the back scattered electrons in any direction ϕ to the normal is given by

$$N^{o} = I.dS.dw.\cos\phi \quad \text{.....A6.1}$$

where N^{o}=number of back scattered electrons in the ϕ direction.

The total number of back scattered electrons incident on the collector is given by

$$N = I.dS.\int\cos\phi dw \quad \text{.....A6.2}$$

between the limits ϕ_1 and ϕ_2

where $\phi_1$and $\phi_2$depend on the geometry of the collector, see figure A6.2.

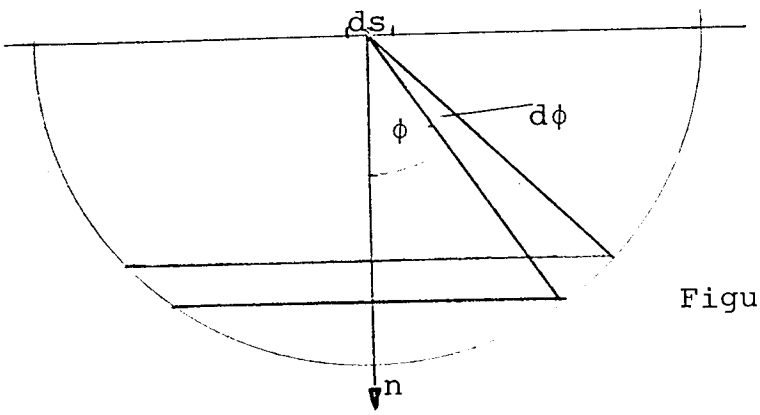

Figure A6.2

Elemental solid angle between ϕ and $\phi + d\phi = 2\pi.\sin\phi d\phi$.

Therefore total back scatter incident on the detector

$$= 2\pi.I.dS.\int\sin\phi.\cos\phi.d\phi \quad \text{.....A6.3}$$

between the limits $\phi_1$and ϕ_2 .

Total back scatter in all directions

$$= 2\pi.I.dS\int \sin\phi.\cos\phi.d\phi \qquad \ldots\ldots\ldots A6.4$$

$$= \underline{\pi.I.dS}$$

$\therefore$ percentage back scattered to detector

$$= 2\int \sin\phi.\cos\phi.d\phi \ .100 \qquad \ldots\ldots\ldots A6.5$$

$$= 100.(\sin^2\phi)$$

evaluated between the limits ϕ_1 and ϕ_2.

Substituting the values of ϕ_1 and ϕ_2 for the collector described in Chapter 9. The percentage of back scattered electrons incident on the collector = 5.4±1.0 %.